Non-canonical Telomerase Reverse Transcriptase Controls Osteogenic Reprogramming of Aortic Valve Cells Through STAT5

Rolando A. Cuevas[1], Luis Hortells[2], Claire C. Chu[1], Ryan Wong[1], Alex Crane[1], Camille Boufford[1], Cailyn Regan[1], William J. Moorhead III[1], Michael J. Bashline[1], Aneesha Parwal[1], Angelina M. Parise[1], Parya Behzadi[1], Mark J. Brown[1], Aditi Gurkar[3], Dennis Bruemmer[4], John Sembrat[5], Ibrahim Sultan[6], Thomas G. Gleason[6], Marie Billaud[6], and Cynthia St. Hilaire[1,8,9*]

[1] Division of Cardiology, Department of Medicine, Pittsburgh Heart, Lung, Blood and Vascular Medicine Institute, University of Pittsburgh, Pittsburgh, Pennsylvania, USA.

[2] Cardiovascular Research Group, Department of Medical Biology, Faculty of Health Science, UiT-The Arctic University of Norway, 9019 Tromsø, Norway.

[3] Aging Institute, Division of Geriatrics, Department of Medicine, University of Pittsburgh, Pittsburgh, Pennsylvania, USA.

[4] Department of Cardiovascular Medicine, Cleveland Clinic, Cleveland, OH, USA.

[5] Division of Pulmonary, Allergy, and Critical Care Medicine, University of Pittsburgh School of Medicine, Pittsburgh, PA, USA.

[6] Division of Cardiac Surgery, Department of Cardiothoracic Surgery, Heart and Vascular Institute, University of Pittsburgh Medical Center, Pittsburgh, Pennsylvania, USA.

[7] Department of Surgery, Division of Cardiac Surgery, Brigham and Women's Hospital & Harvard Medical School, Boston, Maryland, USA.

[8] Department of Bioengineering, University of Pittsburgh, Pittsburgh, Pennsylvania, USA.

[9] Department of Cardiothoracic Surgery, University of Pittsburgh, Pittsburgh, Pennsylvania, USA

Running Title: TERT/STAT5 is required for valvular calcification

*Corresponding Author Contact Info:
Cynthia St. Hilaire, PhD, FAHA
University of Pittsburgh
BSTWR 1744.1
200 Lothrop Street, Pittsburgh, PA 15261
+1 412-648-9441 sthilair@pitt.edu

TOTAL WORD COUNT: 7285
ABSTRACT WORD COUNT: 302

Background: Calcific aortic valve disease (CAVD) is the pathological remodeling of valve leaflets. The initial steps in valve leaflet osteogenic reprogramming are not fully understood. As telomerase reverse transcriptase (TERT) overexpression primes mesenchymal stem cells to differentiate into osteoblasts, we investigated whether TERT contributes to the osteogenic reprogramming of valve interstitial cells (VICs).
Methods: Human control and CAVD aortic valve leaflets and patient-specific hVICs were used in in vivo and in vitro calcification assays. Loss of function experiments in hVICs and cells isolated from *Tert*$^{-/-}$ and *Terc*$^{-/-}$ mice were used for mechanistic studies. Calcification was assessed in *Tert*$^{+/+}$ and *Tert*$^{-/-}$ mice ex vivo and in vivo. In silico modeling, proximity ligation and co-immunoprecipitation assays defined novel TERT interacting partners. Chromatin immunoprecipitation and CUT&TAG sequencing defined protein-DNA interactions.
Results: TERT protein was highly expressed in calcified valve leaflets without changes in telomere length, DNA damage, or senescence markers, and these features were retained in isolated primary hVICs. *TERT* expression increased with osteogenic or inflammatory stimuli,

and knock-down or genetic deletion of *TERT* prevented calcification in vitro and in vivo. Mechanistically, TERT was upregulated via NF-κB and required to initiate osteogenic reprogramming, independent of its canonical reverse transcriptase activity and the lncRNA *TERC*. TERT exerts non-canonical osteogenic functions via binding with Signal Transducer and Activator of Transcription 5 (STAT5). Depletion or inhibition of STAT5 prevented calcification. STAT5 was found to bind the promoter region of Runt-Related Transcription Factor 2 (*RUNX2*), the master regulator of osteogenic reprogramming. Lastly, we demonstrate that TERT and STAT5 are upregulated and colocalized in CAVD tissue compared to control tissue.

Conclusions: TERT's non-canonical activity is required to initiate calcification. TERT is upregulated via inflammatory signaling pathways and partners with STAT5 to bind the *RUNX2* gene promoter. These data identify a novel mechanism and potential therapeutic target to decrease vascular calcification.

ABBREVIATIONS:

CAVD, calcific aortic valve disease; CNN, calponin; CUT&Run, cleavage under targets & release using nuclease; CUT&Tag, cleavage under targets & tagmentation; CFAST, fluorescence-activating and absorption-shifting tag, C-domain; Ch-IP, chromatin immunoprecipitation; E2F1, E2F transcription factor 1; ECM, extracellular matrix; GO, gene ontology; γ-H2AX, phosphorylated gamma histone 2AX; hCASMCs, human coronary smooth muscle cells; hVICs, human aortic valve interstitial cells; IP, immunoprecipitation; lncRNA, long non-coding RNA; LPS, lipopolysaccharide; BMMSCs, bone marrow mesenchymal stem cells; MSCs, mesenchymal stem cells; NFAST, fluorescence-activating and absorption-shifting tag, N-domain; NT, no treatment; mVICs, mouse aortic valve interstitial cells OPN, osteopontin; OST, osteogenic treatment; PCNA, proliferating cell nuclear antigen; PLA, proximity ligation assay ; RUNX2, runt-related transcription factor 2; αSMA, alpha 2 smooth muscle actin; SMARCA4,

76 SWI/SNF chromatin remodeling complex A4; STAT5, signal transducer and activator of
77 transcription 5A/B; *lncTERC*, telomerase RNA component; TERT, telomerase reverse
78 transcriptase; TL, telomere length; TNAP, Tissue-Nonspecific Alkaline Phosphatase; TSS,
79 transcription start site, αTUB, alpha-tubulin
80

81 **Key Words:**
82 calcific aortic valve disease, vascular calcification, osteogenic reprogramming, TERT, STAT5
83

84 **Novelty and Significance**

85 *What is known?*

86 • Calcific aortic valve disease (CAVD) is the most prevalent form of aortic valve pathology.
87 CAVD strongly correlates with age and leads to heart failure and a high risk of stroke.
88 Currently, the only therapeutic option is valve replacement, which comes with significant
89 healthcare costs and additional risks to patients.
90 • Runt-related transcription factor 2 (RUNX2) is the master transcription factor required for
91 osteogenic differentiation of stem cells to osteoblasts and osteogenic reprogramming of
92 cardiovascular cells. Yet, the early events driving its activity in aortic valve cells are poorly
93 defined.
94 • In addition to its reverse transcriptase enzymatic activity, TERT exhibits non-canonical
95 transcriptional regulatory functions and overexpression of TERT primes mesenchymal stem
96 cells to differentiate down the osteoblast lineage.
97

98 *What new information does this article contribute?*

99 • TERT protein levels in calcified aortic leaflets and valve interstitial cells, and its non-
100 canonical osteogenic activity are independent of changes in telomere length and cell
101 senescence.
102 • Genetic loss or depletion of TERT prevented calcification in valve interstitial cells, coronary
103 smooth muscle cells, and mesenchymal stem cells in vitro and the vasculature in vivo.
104 • Early in the osteogenic reprogramming inflammatory signaling promotes TERT to co-localize
105 with SMARCA4 and STAT5, and this TERT-tethered STAT5 binds to the *RUNX2* gene
106 promoter, the master regulator of osteogenic transcriptional programs.
107 • STAT5 depletion and pharmacological inhibition prevent calcification of human valve
108 interstitial cells, coronary smooth muscle cells, and mesenchymal stem cells.
109
110 *What are the clinical implications?*
111 • We have identified TERT-STAT5 as a novel signaling axis that orchestrates the early steps
112 in the osteogenic reprogramming of aortic valve cells. Inhibiting TERT/STAT5 interaction or
113 their activity may be leveraged for the development of therapeutic strategies to halt or
114 prevent calcification in the aortic valve, bioprosthetic valves, and or perhaps other
115 cardiovascular tissues.
116 • Invasive and expensive surgical procedures are currently the only treatment option for
117 patients with CAVD. The discovery and defining of the early events driving vascular
118 calcification identifies novel and druggable targets for developing non-surgical therapies.
119

120 **INTRODUCTION**

121 Calcific aortic valve disease (CAVD) encompasses a spectrum of pathological remodeling of the
122 valve leaflet, ranging from mild valve thickening that displays microcalcifications to
123 macrocalcifications that predominate in more advanced disease stages.[1,2] The advanced state,
124 aortic stenosis, results from fibrotic remodeling and the formation of calcified nodules on the
125 valve leaflet that impede and disrupt blood flow, causing excessive strain on the cardiac tissue,
126 increasing the risk of stroke and leading to heart failure.[3] CAVD severity and incidence increase
127 with age, with CAVD prevalence >1,000 per 100,000 individuals ≥75 years of age.[4,5] Further,
128 roughly 0.4-0.6% of the population harbors bicuspid aortic valve malformations, and these
129 malformed valves are prone to calcify and develop CAVD.[4] Currently, no therapeutic treatment
130 halts or reverses pathologic calcification that occurs in the aortic valve leaflets or other
131 cardiovascular tissues. The only therapeutic option to treat aortic stenosis is valve replacement
132 via surgical or transcatheter procedures, incurring substantial medical costs and health care
133 burdens to the patient.[6]
134
135 Aortic valve interstitial cells (VICs) are the primary cell type within the valve leaflet and are
136 responsible for maintaining leaflet integrity. VICs reside in a quiescent state; however, adaptive
137 or maladaptive responses to environmental factors such as inflammation, extracellular matrix
138 (ECM) breakdown, and mechanical stress may disrupt VIC homeostasis.[7,8] With alterations in
139 homeostasis, VICs acquire a myofibroblast-like phenotype, termed “activated VICs,” capable of
140 proliferation, contraction, and secretion of proteins that further remodel the extracellular milieu.[9]
141 Activated VICs can transition into calcifying cells; however, the initial steps regulating this
142 process are not fully understood. It is well established that the osteogenic reprogramming of
143 cardiovascular cells such as VICs and vascular smooth muscle cells (SMCs) is analogous to the

144 differentiation of mesenchymal stem cells (MSCs) into bone-forming osteoblasts; osteogenic
145 differentiation of MSCs and the reprogramming of cardiovascular cells is primarily orchestrated
146 by Runt-related transcription factor 2 (*RUNX2*), the master regulator of osteogenic
147 transcriptional programs.[10-12] Other osteogenic signature markers, such as osteocalcin, alkaline
148 phosphatase, and osteopontin, are upregulated in the differentiation of stem cells to osteoblasts
149 and the calcifying of VICs.[9,13] While it is accepted that VICs upregulate the expression of
150 osteogenic genes in response to stresses such as inflammation, ECM remodeling, and
151 mechanical stress, the specific mechanistic steps between those stresses and the initial
152 reprogramming events in the activation of osteogenic transcriptional reprogramming remain ill-
153 defined.
154
155 The telomerase complex extends and maintains the ends of chromosomes after cell division.
156 The core complex consists of the telomerase long non-coding RNA component (*lncTERC*) and
157 telomerase reverse transcriptase (TERT) protein, along with other scaffolding proteins.[14] In
158 addition to reverse transcriptase activity, TERT also exhibits non-canonical functions
159 independent of telomere extension, such as regulating gene expression and orchestrating
160 chromatin remodeling.[15-17] For example, TERT acts as a cofactor in Wnt-dependent promoter
161 activation by interacting with the chromatin remodeling protein SWI/SNF related, matrix
162 associated, actin dependent regulator of chromatin, subfamily a, member 4 (SMARCA4),
163 facilitating the expression of Wnt/β-catenin target genes in stem cells.[18] In a murine model of
164 atherosclerosis, TERT induced chromatin remodeling and SMC proliferation by chaperoning the
165 retinoblastoma-associated transcription factor 1 (E2F1) binding to S-phase gene promoters.[19,20]
166 Linking together the themes of calcification and non-canonical TERT, two co-published studies
167 identified that the overexpression of *TERT* primed human MSCs to differentiate down the
168 osteogenic lineage and develop bone-like structures.[21,22] The mechanism by which TERT drives

169 the osteogenic differentiation of human MSCs is unknown. Collectively, these studies provide
170 strong evidence of telomerase-independent functions of TERT in altering chromatin states and
171 regulating gene expression via various protein-protein interactions.
172
173 Although telomere length is recognized as a biomarker of aging, it can vary significantly among
174 individuals of the same age, including twins.[23] Studies have examined the association between
175 shortened telomeres in circulating leukocytes and various vascular conditions, with mixed
176 results.[24-26] One study compared telomere lengths in leukocytes of control patients and those
177 with atherosclerotic plaques, as well as the atherosclerotic plaques themselves and found that
178 while atherosclerotic patients' leukocytes had shorter telomeres than controls, their plaque cells
179 exhibited longer telomeres than both groups' leukocytes, suggesting heightened telomerase
180 activity in the diseased tissue.[27-29] Thus, whether leukocyte telomere length can be used as a
181 biomarker remains speculative. A notable aspect of these prior studies is the lack of TERT
182 protein assessment or a focused investigation of telomere length in disease tissues.
183
184 Signal transducers and activators of transcription (STAT) proteins play essential roles in
185 inflammatory, proliferative, and apoptotic programs, mediating the signal transduction pathways
186 of various cytokines and growth factors.[30] STAT proteins function as transcription factors and
187 recruit chromatin remodeling and histone-modifying proteins to upregulate gene transcription.[31]
188 STAT5A and STAT5B are encoded by two highly conserved genes in humans and mice; 96% of
189 their amino acid sequence is shared, and many of their activities are redundant.[32] Herein,
190 unless specific tools are utilized to allow a distinction, we will generally refer to both as STAT5.
191 Upon phosphorylation, STAT5 dimerizes and translocates into the nucleus to bind the
192 consensus motif (TTCNNNGAA) and activates the promoters of various target genes by

193 recruiting transcriptional co-activators.[33,34] Crucially, studies have shown that several osteogenic
194 genes depend on STAT5 to promote chondrocyte and osteoblast differentiation.[35,36]
195
196 In this study, we tested the hypothesis that TERT contributes to the osteogenic reprogramming
197 of VICs. We utilized primary human aortic valve tissues from control donors and CAVD patients
198 and generated patient-specific VIC lines for in vitro disease modeling. We established baseline
199 patterns and osteogenic induction of *TERT* and calcification markers in CAVD tissue and VICs.
200 We assessed the consequences of genetic deletion or depletion of *TERT* during osteogenic
201 reprogramming in several cell types and in in vivo and ex vivo calcification models. We further
202 defined the underlying mechanism by which TERT and STAT5 participate in the osteogenic
203 reprogramming of VICs.
204

205 **METHODS**

206 **Data Availability**

207 The Materials, Methods, and Major Resources Table are found in the Supplemental Material.
208 The raw data, experimental materials, and analytic methods are available from the
209 corresponding author upon reasonable request.
210

211 **RESULTS**

212 **TERT is elevated in CAVD tissues.**

213 Human aortic valves were collected after surgical aortic valve replacement procedures or from
214 cadaveric tissue obtained via the Center for Organ Recovery and Education (CORE) of the
215 University of Pittsburgh Medical Center and processed as previously described.[37] Macroscopic
216 examination and histological staining with Von Kossa were used to determine and confirm

217 whether valves could be classified as a non-calcified control or as having calcific aortic valve
218 disease (CAVD) (**Figure 1A, Supplemental Figure 1A, Supplemental Table 1**). RUNX2 is the
219 master transcription factor required to initiate stem cells to differentiate into osteoblasts and is
220 critical for the pathological osteogenic reprogramming of vascular cells.[38-41] Immunofluorescent
221 staining showed RUNX2, and the late calcification marker osteopontin (OPN) were significantly
222 upregulated in CAVD tissue compared to control tissues, indicating activation of osteogenic
223 transcriptional programs in CAVD tissues (**Supplemental Figure 1B**). Previous studies found
224 that overexpression of TERT primes human MSCs to differentiate down the osteogenic
225 lineage.[21,22] We found that *TERT* transcript levels were significantly upregulated in CAVD tissue
226 relative to control samples (**Figure 1B**), and *TERT* expression levels showed no correlation with
227 the donor's age (**Supplemental Figure 1C**). Markers of senescence (cyclin-dependent kinase
228 inhibitor 1A, *CDKN1A*, galactosidase beta 1, *GLB1*), proliferation (proliferating cell nuclear
229 antigen, *PCNA*), DNA damage (tumor protein 53, *TP53*), and cytoskeletal markers (actin alpha
230 2 smooth muscle, *ACTA2*, vimentin, *VIM,* interleukin 6, *IL6*) showed no statistically significant
231 differences, while the inflammatory marker and tumor necrosis factor-alpha (*TNF)* was
232 significantly elevated in CAVD samples (**Supplemental Figure 1D**), supporting observations by
233 others that indicate a role for inflammatory signaling in aortic valve calcification
234 pathogenesis.[42,43]
235
236 We detected elevated TERT protein signal in CAVD valves compared to non-calcified controls,
237 with the signal localized to areas of calcification. Similarly, the number of cells expressing TERT
238 was significantly elevated in our CAVD tissues compared to non-calcified control tissues
239 (**Figure 1C**). No statistically significant differences were observed in the staining levels of
240 proliferation marker PCNA or the DNA damage indicator phosphorylated gamma histone 2AX
241 (γ-H2AX) between CAVD and control tissues (**Supplemental Figure 1E**). We also found no

242 statistically significant differences in the relative mean telomere length between the control and
243 CAVD tissues in our study (**Figure 1D**), indicating no overt influence of the canonical telomere-
244 extending functions of TERT. The mean age of CAVD patients in this study was slightly
245 elevated compared to the control patients, 68 and 54 years old, respectively (**Figure 1E**).
246 Together, these data show that TERT, osteogenic markers, and inflammatory signatures are
247 upregulated in CAVD tissues compared to controls, while markers indicating alterations in
248 proliferation, DNA damage, and senescence are not altered, suggesting that the non-canonical
249 activity of TERT is operative.
250

251 **CAVD human VICs at baseline recapitulate observations in CAVD tissues.**

252 We created patient-specific valve interstitial cell (VIC) lines from CAVD and control valves.[37] At
253 baseline, freshly isolated hVICs from CAVD and control patients exhibited no morphological or
254 statistical differences in their proliferative or migratory capacity (**Figure 2, A- C, and**
255 **Supplemental Figure 1F**). TERT and RUNX2 proteins were significantly elevated at baseline in
256 CAVD hVICs compared to control hVICs (**Figure 2D**). We observed no statistical differences in
257 the protein levels of the hVIC activation markers SM22 or αSMA between CAVD and control
258 hVICs, but observed a significant increase of the mineralizing enzyme tissue non-specific
259 alkaline phosphatase (TNAP) in CAVD hVICs at baseline (**Supplemental 1G**). As in the leaflets,
260 there was no statistical difference in the relative telomere length between CAVD and control
261 hVICs (**Figure 2E**). These data show that hVICs isolated from CAVD patients display gene
262 expression and protein signatures that recapitulate the osteogenic phenotype observed in
263 CAVD leaflet tissue.
264

265 **TERT expression is upregulated in human VICs in an in vitro osteogenic disease model.**

266 To model CAVD in vitro and investigate a role for TERT during hVIC osteogenic
267 reprogramming, we cultured CAVD and control hVICs in osteogenic media conditions (OST), a
268 media widely utilized to induce osteogenic differentiation of stem cells to osteoblasts.[44] Alizarin
269 Red staining for calcification revealed that both OST-treated CAVD and control hVICs lay down
270 calcified matrix as early as 14 days (d14), CAVD hVICs calcified earlier relative to control hVICs
271 (**Figure 2F**). Importantly, we observed that CAVD hVICs calcify de novo under no treatment
272 (NT) conditions, suggesting that CAVD hVICs are primed for osteogenic reprogramming (**Figure**
273 **2F**). The calcification markers RUNX2 and OPN were significantly upregulated in both control
274 and CAVD hVICs at d14 OST, indicating active osteogenic reprogramming (**Figure 2G**). TERT
275 protein levels were also significantly increased in control and CAVD hVICs after d14 of OST
276 (**Figure 2G**). TERT protein signal can be seen in CAVD hVICs at d14 under NT conditions
277 (**Figure 2H**, left panels). At d14 of OST, the TERT protein staining was elevated and localized
278 near areas of calcification in both control and CAVD hVICs; however, CAVD hVICs formed
279 larger calcified nodules (**Figure 2H**, right panels). We observed no significant differences in cell
280 numbers at the end of the d14 assay under NT or OST treatment conditions (**Supplemental**
281 **Figure 2A**). As we observed that CAVD hVICs exhibit elevated osteogenic markers at baseline
282 (**Supplemental Figure 1G**) and are prone to calcify (**Figure 2H**) de novo, we assessed
283 transcriptional differences between control hVICs under NT or OST. Osteogenic markers *BMP2*,
284 *THBS1*, *ALPL,* and myofibroblast markers *CNN1*, *TAGLN*, and *SMTN* were significantly
285 upregulated in control hVICs at d14 of OST treatment (**Figure 2I**). Likewise, the calcification-
286 associated gene *FOXO1* and the CAVD-associated metalloproteinase *MMP13* were also
287 significantly upregulated in OST conditions.[45,46] Lastly, the pro-inflammatory transcription factor
288 signal transducer and activator of transcription 5A *(STAT5A)* was significantly upregulated,
289 while the expression of the isoform *STAT5B* remained unchanged. These results show that
290 hVICs are undergoing osteogenic reprogramming and not de novo mineral nucleation.[47]

291

292 In cancer and stem cells, elevated expression of TERT is associated with long telomeres and
293 enables unlimited proliferation, while short telomeres can trigger cellular senescence.[48,49]
294 Although we observed no differences in telomere length in our tissues and cells in this study
295 (Figures 1D and 2E), we assessed cellular senescence and observed no significant differences
296 in the expression of senescence-associated β-galactosidase (SA-β-gal, *GLB1*) between CAVD
297 and control hVICs at baseline **(Supplemental Figure 2B)** nor increased in control hVICs in OST
298 treatment (**Figure 2I**). SA-β-gal activity staining indicated that cellular senescence was not
299 engaged even after 28 days of OST treatment (**Supplemental Figure 2C**). These data
300 confirmed that cellular senescence is not operative during hVICs osteogenic reprogramming.
301

302 NF-κB is a transcription factor complex that acts downstream of inflammatory signals to mediate
303 inflammatory responses, and the c-Myc transcription factor mediates cell proliferation and
304 differentiation. Others have shown that both NF-κB and c-Myc can upregulate transcription of
305 the *TERT* gene.[50-52] We found that inhibiting NF-κB with BAY-107082, an irreversible inhibitor
306 that blocks the phosphorylation of IκB-α,[53,54] inhibited *TERT* expression during the osteogenic
307 reprogramming of hVICs. We also observed downregulation of *RUNX2* expression, consistent
308 with upstream TERT's regulatory role on *RUNX2* expression (**Supplemental Figure 2D**).
309 Likewise, we found that inhibiting c-MYC with 10058-F4 inhibited *TERT* expression during the
310 osteogenic differentiation of hVICs (**Supplemental Figure 2E**), validating previous research
311 showing that c-MYC regulates *TERT* gene expression.[16] These results further support that
312 inflammatory signaling contributes to the development of CAVD.
313

314 **TERT is required for the osteogenic differentiation of human MSCs.**

315 Previous studies have shown that the overexpression of TERT primes human mesenchymal
316 stem cells (hMSCs) to differentiate into osteoblasts.[21,22] To assess the role of endogenous
317 TERT in osteogenic differentiation, we subjected hMSCs to NT and OST treatment. OST
318 treatment induced robust calcification as early as d14, while cells in NT conditions did not calcify
319 (**Supplemental Figure 3A**). Protein analysis showed that the TERT protein levels significantly
320 increased on day 3 of the OST treatment, coinciding with increased *RUNX2* expression and
321 RUNX2 protein levels (**Supplemental Figures 3B and 3C**). hMSCs in OST treatment exhibited
322 intense TERT staining, and TERT-positive cells clustered around calcified nodules
323 (**Supplemental Figure 3D**). Using lentiviral-mediated transduction of expressing short-hairpin
324 RNA to deplete TERT (shTERT) or scrambled control (shControl), we found that knockdown of
325 *TERT* significantly inhibited the calcification of hMSCs (**Supplemental Figures 3E and 3F**).
326 While previous studies show that overexpression of *TERT* primed hMSCs to undergo
327 osteogenic differentiation, our data show that TERT is required for the osteogenic differentiation
328 of hMSCs.[21,22]
329
330 **TERT is required for calcification in vitro and in vivo.**
331 Control hVICs were transduced with shControl and shTERT lentivirus, and like hMSCs,
332 knockdown of *TERT* significantly inhibited calcification compared to the control group and
333 downregulated RUNX2 protein levels (**Figures 3A and 3B**). We assessed TERT's role in
334 calcifying human coronary artery smooth muscle cells (hCASMCs), which calcify in
335 atherosclerotic plaques.[55] Knocking down TERT significantly inhibited hCASMCs calcification
336 (**Figure 3C**). Together, these data indicate that TERT is essential for the osteogenic
337 reprogramming of hVICs and hCASMCs. Next, mice VIC (mVICs) and bone marrow MSCs
338 (mBMMSCs) lines were generated from *Tert*$^{+/+}$ and *Tert*$^{-/-}$ mice.[56] In line with our observations in
339 human cells with depleted TERT, we observed significant inhibition of calcification in *Tert*$^{-/-}$

340 mVICs (**Figure 3D**) and *Tert*$^{-/-}$ mBMMSCs (**Supplemental Figure 4A**) compared to *Tert*$^{+/+}$ cells.
341 No statistically significant differences were observed in senescence-associated β-galactosidase
342 activity in mVICs or mBMMSCs (**Supplemental Figures 4B** and **4C**).
343
344 To determine whether TERT is required to initiate and/or maintain osteogenic reprogramming,
345 we cultured control hVICs in OST and transduced shTERT lentivirus on d7 or d14, and
346 calcification was assessed on d21. Control hVICs transduced with shTERT on day 7 showed a
347 significant reduction in calcification compared to the OST alone, while transduction of shTERT
348 on day 14 did not show any decrease in calcification (**Supplemental Figure 4D**), indicating that
349 TERT is required to initiate, not maintain, reprogramming to the osteogenic phenotype.
350
351 Next, we used *Tert*$^{+/+}$ and *Tert*$^{-/-}$ mice strains to test whether TERT is required for diet-induced
352 non-atherosclerotic medial arterial calcification in vivo in mice. Of note, *Tert*$^{-/-}$ mice were
353 generated from heterozygous breeding pairs (F1 generation) and thus did not exhibit shortened
354 telomeres.[57] *Tert*$^{+/+}$ and *Tert*$^{-/-}$ mice were fed an adenine-phosphate (A6P6) diet, which was
355 previously shown to induce medial arterial calcification in the vasculature of mice.[58] At the end
356 of the 12-week regime, we observed significantly higher levels of calcification in the aorta of
357 *Tert*$^{+/+}$ compared to *Tert*$^{-/-}$ mice (**Figure 3E**). Staining for Runx2 protein mirrored calcification
358 presentation and was significantly higher in the *Tert*$^{+/+}$ compared to *Tert*$^{-/-}$ tissue (**Figure 3F**).
359 These findings were validated in an ex vivo calcification assay. Thoracic aortic rings obtained
360 from the *Tert*$^{+/+}$ and *Tert*$^{-/-}$ mice were cultured in ex vivo OST or control NT medium. *Tert*$^{+/+}$
361 aortic rings exhibited significantly elevated calcification compared to aortic rings from *Tert*$^{-/-}$ mice
362 on d14 (**Supplemental Figure 4E**). *Tert*$^{+/+}$ aortic rings also exhibited prominent staining for
363 Runx2 protein, which was absent in aortic rings from *Tert*$^{-/-}$ mice (**Supplemental Figure 4F**),
364 and western blot analysis confirmed elevated Runx2 protein levels in *Tert*$^{+/+}$ aortic rings

365 compared to *Tert*$^{-/-}$ (**Supplemental Figure 4G**). Neither calcification nor Runx2 was detected in
366 the NT groups. Together, these data show that TERT is required for osteogenic reprogramming
367 of cells in vitro and in vivo.
368
369 TERT's canonical telomere-extending activity requires the telomerase long non-coding RNA
370 component (*lncTerc*) to maintain chromosome telomere length and genome integrity.[14,59] *LncTerc*
371 exerts a dual function in the telomerase complex; it guides the telomerase complex to the telomere
372 ends and is the primer for TERT reverse transcriptase activity, and it serves as a scaffold for
373 tethering additional proteins to the telomerase complex (i.e., Dyskerin, NOP10, GAR1, and
374 NHP2).[60] To evaluate that TERT's role in calcification is independent of its canonical telomere-
375 extending function, we isolated mVICs from *Terc*$^{-/-}$ mice. While *Tert*$^{-/-}$ mVICs did not calcify under
376 OST conditions, *Terc*$^{-/-}$ mVICs were significantly calcified (**Figure 3G**). Similarly, in hVICs,
377 BIBR1532, which blocks the reverse transcriptase activity of TERT,[61] did not prevent calcification
378 nor decrease the expression of *RUNX2* (**Supplemental Figure 4H and 4I**). Together, these data
379 illustrate that the canonical telomere-extending function of TERT does not contribute to
380 osteogenic reprogramming.
381
382 **TERT/STAT5 interact and bind to the *RUNX2* gene promoter to initiate osteogenic**
383 **reprogramming.**
384 Several studies have shown that TERT participates in gene transcription by physically
385 interacting with transcription factors.[17,20,62,63] RUNX2 is the master regulator of osteogenic
386 differentiation of stem cells.[38,39] Increased *RUNX2* expression and transcriptional activity are the
387 hallmarks of osteoblast differentiation and cardiovascular calcification and are required for
388 osteogenic reprogramming of vascular cells.[40,41] As our data show that RUNX2 is significantly
389 downregulated in *TERT*-knockdown and deficient cells (Figure 3), we used the LASAGNA[64] and

390 TRANSFAC/MATCH[65] programs to identify putative transcription factor binding sites in the 5 kb
391 region upstream of the human *RUNX2* gene promoter (NM_001015051.3) and identified eight
392 potential STAT5 binding sites (**Supplemental Table 2**). We sought to determine whether
393 STAT5 is bound to the *RUNX2* gene promoter and focused on the two most proximal predicted
394 STAT5 sites located at -1371 bp and -193 bp upstream of the transcriptional start site (TSS), as
395 both have high homology to the tetrameric consensus STAT5 binding site and show an elevated
396 likelihood of being functional sites (**Figures 4A** and **4B**). As inflammation and inflammatory
397 signaling pathways are known to contribute to CAVD pathogenesis[1,66], and *TERT* expression
398 was induced via that inflammatory transcription factor NF-κB (Supplemental Figure 2D), we
399 used bacterial lipopolysaccharide (LPS) as a broad method to activate inflammatory response
400 pathways in hVICs. We found that LPS was sufficient to induce calcification of hVICs and that
401 TERT-positive cells accumulated near calcified nodules (**Figure 4C**). Protein analysis showed
402 that OST and LPS significantly upregulate TERT, RUNX2, and STAT5 proteins (**Figure 4D**).
403 TERT protein levels were elevated in both the cytosol and nucleus of cells upon OST
404 stimulation (**Supplemental Figure 5A**). Under NT conditions, STAT5 is observed in the
405 membrane and cytosol but translocates and accumulates in the nucleus of hVICs in OST
406 (**Supplemental Figure 5B**). Next, we used genetic and pharmacological approaches to
407 determine the requirement of STAT5 for the calcification of hVICs. The small molecules StafiA-1
408 and StafiB-1 specifically inhibit STAT5A and STAT5B, respectively.[67,68] We found that StafiA-1
409 significantly inhibited the calcification of control hVICs during a 21-day OST assay and that this
410 inhibition was greater than the inhibition observed with StafiB-1 (**Figure 4E**). In line with these
411 findings, we also observed that inhibition of STAT5A significantly reduced the expression of
412 *RUNX2* at d7 of osteogenic differentiation of hVICs, suggesting that STAT5A is a main
413 participant during the osteogenic reprogramming of hVICs (**Figure 4F**). Similarly, StafiA-1
414 significantly reduced calcification in hCASMCs and hMSCs (**Supplemental Figures 5C** and

415 **5D**). Lentiviral-mediated delivery of shControl or shSTAT5 constructs showed that depletion of
416 STAT5 significantly attenuated calcification and *RUNX2* expression (**Figure 4G and 4H**),
417 confirming an essential role for STAT5 in the osteogenic reprogramming of hVICs. Similar to
418 TERT (Supplemental Figure 4D), knocking down STAT5 after 7 or 14 days of OST treatment did
419 not reduce calcification (**Figure 4I**), indicating that STAT5 activity is required during the initial
420 steps of osteogenic reprogramming. Others have established that TERT can interact with
421 transcription factors to regulate gene expression.[17,20,62,63] We assessed whether TERT and
422 STAT5 directly interact. Three methods were utilized: proximity ligation assay (PLA), co-
423 immunoprecipitation (IP), and exogenously expressing TERT and STAT5 reporters. PLA can
424 detect protein-protein proximity <40 nm apart.[69] PLA revealed that OST significantly increased
425 TERT and STAT5 colocalization in control hVICs after 21 days of OST treatment relative to NT
426 condition (**Figure 4J**). Focusing on nuclear co-localization, TERT/STAT5 puncta are
427 significantly elevated in the nucleus of calcifying hVICs relative to the NT condition
428 (**Supplementary Figure 5E**). Protein IP shows that TERT and STAT5 physically interact in
429 hVICs upon OST treatment relative to NT condition (**Figure 4K**). A Dual-Luciferase reporter
430 assay shows that the human *RUNX2* promoter, containing the -194 and -1371 putative STAT5
431 binding sites, is upregulated early (d3) under OST treatment relative to NT, and that this
432 upregulation is abrogated with pharmacological inhibition of STAT5A, validating the functionality
433 of the predicted STAT5 binding in the *RUNX2* promoter (**Supplementary Figure 5F**).
434 Furthermore, an electrophoretic mobility shift assay (EMSA) confirmed the physical binding of
435 STAT5A to DNA oligos containing the predicted -194 STAT5A binding site on the RUNX2
436 promoter (wt RUNX2 oligo). This interaction was validated by challenging the oligo-STAT5
437 complex with increasing amounts of unlabeled (cold) oligos. Moreover, the binding was entirely
438 abrogated by incubating the STAT5 extract with oligos where the STAT5A binding site was
439 entirely randomized (mut RUNX2 oligo) (**Supplementary Figure 5G**). Supporting a role for

440 STAT5 in osteogenic reprogramming, STAT5 protein levels were significantly lower in the aorta
441 of *Tert*$^{-/-}$ mice fed the A6P6 diet compared to the aorta from *Tert*$^{+/+}$ mice (**Supplemental Figures**
442 **5H**), and these findings were replicated in the ex vivo calcification assay (**Supplemental Figure**
443 **5I**). These experiments demonstrate that STAT5 directly acts on DNA in the *RUNX2* promoter
444 and contributes to osteogenic reprogramming in cardiovascular tissues.
445
446 While the domains of TERT were initially defined by their role in the telomere-extending
447 functions of TERT, protein partners required for the known non-canonical functions of TERT
448 have been found in several domains throughout the protein.[70] Further, sites for protein binding
449 partners to STAT5, such as epigenetic modifiers and transcriptional regulators, have been found
450 throughout the protein.[71] We used AI-assisted technology to generate tertiary structures of
451 TERT and STAT5 dimers and predict how they may interact. AlphaFold[72] mapped the
452 interaction between human TERT and dimerized human STAT5A, and these binding data were
453 visualized using HDOCK[73] (**Supplemental Figure 5J and 5K**). To gain a more comprehensive
454 and detailed understanding of the TERT/STAT5 interaction we will utilize a next-generation
455 fluorescence-based complementation system developed by Tebo and Gautier in 2019
456 (splitFAST).[74] This system has very low background fluorescence and can be temporally
457 regulated, enabling the visualization of transient TERT/STAT5 interactions in living cells or fixed
458 cells, to provide a scalable model that can be used to screen for compounds that block the
459 TERT/STAT5 interaction. We fused the human cDNA of TERT and STAT5 to NFAST and
460 CFAST splitFAST reporters, respectively, to generate TERT-NFAST and STAT5A-CFAST
461 fusion proteins. This approach allows monitoring of the formation and dissociation of a protein
462 assembly.[74] Control hVICs were co-transfected with TERT-NFAST and STAT5A-CFAST
463 plasmids and 5 μM HBR-3,5DOM (4-hydroxy-3,5- dimethoxy benzylidene rhodamine)
464 administered at d3, d5, and d7 of OST or NT. We found that the TERT/STAT5 splitFAST signal

465 was highly elevated in calcifying control hVICs relative to the NT condition as early as d3
466 throughout d7, supporting the early formation of the TERT/STAT5 complex in calcifying hVICs
467 (**Figure 4L**). Together, these approaches confirm TERT and STAT5 interaction and
468 translocation into the nucleus during osteogenic reprogramming.
469
470 To assess the function of TERT-STAT5 interaction, we performed chromatin
471 immunoprecipitation analysis (Ch-IP). We found that STAT5 is significantly enriched on both
472 putative STAT5 binding sites in the *RUNX2* promoter during osteogenic reprogramming (**Figure**
473 **4M**). *RUNX2* transcription is initiated from two distinct promoters: the distal promoter region P1,
474 located upstream of exon 1, and the proximal P2 promoter, located upstream of exon 2.[75,76] The
475 P1 promoter is highly active and required for osteoblast progenitor expansion, osteoblast
476 maturation, and bone formation, while the P2 promoter-derived isoform is expressed in
477 osteoblastic and non-osteoblastic mesenchymal cells.[77-79] Genome-wide CUT&Run analysis of
478 the histone marker H3K4me3 showed that RUNX2 promoters P1 and P2 are significantly
479 upregulated during osteogenic differentiation on human VICs, while Gene Ontology (GO)
480 pathway analysis revealed that genes related to the telomerase complex, chromatin remodeling,
481 and metabolic pathways are upregulated during osteogenic differentiation of hVICs
482 (**Supplementary Figures 5L and 5M**, GEO accession GSE280657). We assessed STAT5
483 binding to the *Runx2* P1 and P2 promoters during osteogenic differentiation using CUT&Tag
484 analysis in the *Tert*$^{+/+}$ and *Tert*$^{-/-}$ mVICs. We found that STAT5 binds to the *Runx2* P1 and P2
485 promoters during osteogenic differentiation and that STAT5 was absent from these regions in
486 *Tert*$^{-/-}$ mVICs, highlighting the Tert requirement for Stat5 binding to *Runx2* gene promoters
487 (**Figure 4N**, GEO accession GSE274226). By comparing *Tert*$^{+/+}$ and *Tert*$^{-/-}$ mVICs CUT&Tag
488 sequencing, we found that Stat5 occupies promoter, intragenic, and intergenic regions
489 throughout the genome (**Figure 4O**). GO pathway analysis revealed that genes with high Stat5

490 binding participate in biological processes related to protein phosphorylation, JAK/STAT
491 signaling, inflammation, osteoblast differentiation, SMC function, and chromatin remodeling
492 (**Figure 4P**). Together, these data identify that TERT's effects are mediated via STAT5 binding
493 on the *Runx2* gene promoter and the promoters involved in several pathways known to be
494 operative during osteogenic reprogramming of cardiovascular cells.
495
496 **TERT and STAT5 are upregulated in calcified tissue.**
497 Confirming our in vitro, ex vivo, and in vivo data above, in human CAVD tissue we found that
498 STAT5 protein levels are significantly elevated and localized to areas of calcification in the
499 calcified leaflet alongside TERT distribution. Additionally, the number of STAT5-positive cells
500 was significantly higher in CAVD tissue compared to control tissue (**Figure 5A**). Furthermore,
501 the number of TERT/STAT5 co-positive nuclei was significantly greater in CAVD valves
502 compared to control valves (**Figure 5B**). These data support our in vitro investigations and
503 indicate that TERT/STAT5 interaction contributes to human CAVD pathogenesis.
504
505 **TERT interacts with SMARCA4 during the osteogenic reprogramming of VICs.**
506 Studies by others have shown that TERT facilitates chromatin accessibility and transcription by
507 recruiting SMARCA4 (previously referred to as BRG1), the catalytic subunit of the SWI/SNF
508 chromatin remodeling complex, to specific DNA loci.[18,80,81] We investigated whether SMARCA4
509 plays a role in the osteogenic reprogramming of hVICs via interacting with TERT. There was no
510 difference in SMARCA4 protein staining in the aorta of *Tert*$^{+/+}$ and *Tert*$^{-/-}$ mice fed the A6P6 diet,
511 nor in aortic rings ex vivo (**Supplemental Figures 6A and 6B**). However, in hVICs, expression
512 analysis revealed significant upregulation of *SMARCA4* transcripts as early as d5 of OST
513 stimulation (**Supplementary Figure 6C**). Immunoprecipitation showed that TERT and
514 SMARCA4 physically interact in hVICs upon OST treatment (**Supplementary Figure 6D**).

515 Immunofluorescence staining showed that TERT and SMARCA4 are detected and colocalized
516 in cells in the calcified human leaflet (**Supplementary Figure 6E**), mirroring TERT and STAT5
517 distribution in human CAVD tissue. These findings suggest that SMARCA4 plays an active role
518 in the osteogenic reprogramming of VICs.
519

520 **DISCUSSION**

521 This study investigated the early steps required for the osteogenic reprogramming of human
522 valve interstitial cells in CAVD and establishes a critical role for TERT and STAT5 in this
523 process (**Figure 6**). Specifically, our data show that 1) TERT is upregulated in CAVD tissue and
524 elevated in primary VIC lines stimulated with osteogenic media. While TERT is elevated in these
525 calcified tissues and cells, telomere length is not impacted, nor is there evidence of cell
526 senescence; 2) TERT is required for the calcification of VICs, CASMCs, and MSCs. The
527 requirement for TERT occurs early in the process of osteogenic reprogramming, as knocking
528 down TERT protein levels after seven days of osteogenic stimulation did not deter calcification.
529 These osteogenic reprogramming activities of TERT are independent of its telomerase
530 enzymatic activity, as *Terc*$^{-/-}$ cells or the use of the TERT reverse transcriptase inhibitor did not
531 deter calcification. Further, TERT co-immunoprecipitated with the chromatin remodeling enzyme
532 SMARCA4, and these two proteins were also found in the nucleus of CAVD tissues; 3)
533 Inflammatory signals are known to contribute to CAVD pathogenesis, and we found such
534 signaling can increase TERT levels, as well as the transcription factor STAT5. In silico modeling
535 predicted TERT/STAT5 interaction, which was proven experimentally with immunoprecipitation,
536 proximity ligation assay, and a fluorescence complementation system developed for the
537 visualization of transient protein-protein interactions, and like TERT, genetic knockdown of
538 STAT5, or specific inhibition of STAT5 activity, prevented calcification. We found that STAT5

539 directly binds the DNA of the RUNX2 promoter, as well as genes in pathways related to
540 chromatin remodeling and cellular proliferation and differentiation. Lastly, the requirement for
541 TERT was established in in vivo and ex vivo calcification models. Collectively, these
542 experiments support a novel role for TERT and STAT5 in driving CAVD pathogenesis and
543 cardiovascular reprogramming and identify a unique, druggable target for cardiovascular
544 calcification.
545
546 TERT is well-known for its canonical telomere-extending activity, yet TERT also regulates gene
547 expression and chromatin remodeling independent of affecting telomere integrity. TERT
548 interacts physically with several transcription factors to promote the expression of several
549 genes, including β-catenin, to stimulate genes involved in bone development.[15,16,62] In a wire-
550 injury restenosis model, TERT binds to the transcription factors SP1 at the *VEGF* promoter and
551 E2F1 at *MCM7*, *CCNA1*, and *PCNA* promoters, stimulating SMC proliferation and neointima
552 formation.[20,56,63,82] We did not detect proliferative or migratory differences between control and
553 CAVD VICs despite elevated levels of TERT at baseline (Figures 2B and 2C), indicating cell-
554 specific and stress-specific functions of TERT.
555
556 In addition to supporting transcription factor function, TERT can act as a cofactor to orchestrate
557 chromatin remodeling machinery. Studies have shown that TERT serves as a chaperone to
558 facilitate the recruitment of SMARCA4 and histone acetyltransferases to stimulate chromatin
559 accessibility and transcription or to maintain heterochromatin structure,[18,80,81] and loss of TERT
560 abrogates the cellular response to DNA double-strand breaks and alters the overall chromatin
561 configuration without affecting telomere integrity.[17] We now show that TERT is upregulated in
562 calcified valve tissues and VICs under osteogenic and inflammatory stimuli. TERT interacts with
563 STAT5, which binds to the *RUNX2* gene promoter and drives osteogenic reprogramming of the

564 aortic valve cells. TERT depletion reduced *RUNX2* expression and calcification in several cell
565 types, and TERT, STAT5, and the chromatin remodeling enzyme SMARCA4 co-
566 immunoprecipitated in OST-treated VICs (Supplementary Figure 6). Further, TERT and
567 SMARCA4 co-localized in the nucleus of CAVD tissues. These discoveries, along with the
568 findings of others showing that *TERT* overexpression drives osteogenic differentiation in human
569 MSCs,[21,22] support a broad role for TERT serving as a co-factor bridging chromatin remodeling
570 complexes and transcription factors to facilitate euchromatin formation to modulating cellular
571 phenotypic transition and osteogenic reprogramming.
572
573 Telomere length is considered a biomarker of aging, yet it varies widely between people of the
574 same age, even twins.[23] Several studies have utilized circulating leukocytes to investigate
575 whether shortened telomeres correlate with various vascular disease states.[24,25] One study
576 correlated telomere length in circulating leukocytes with aortic stenosis and found that leukocyte
577 telomere length was slightly shorter in individuals with aortic stenosis than in age-matched
578 controls.[26] However, telomere length in leukocytes does not indicate global telomere length in
579 an individual, telomerase complex activity, or TERT protein function in all cell types. Further,
580 somatic mosaicism and clonal hematopoiesis discoveries underscore the importance of not
581 ascribing telomere length in one cell type to telomere length and/or TERT activities in another.[28]
582 Short telomeres in circulating leukocytes may reflect increased cell turnover due to systemic
583 inflammation, as leukocytes are highly proliferative, and telomere attrition is highly likely to be a
584 tissue- and disease-dependent process. In this regard, Huzen et al. compared the telomere
585 length of the leukocytes of age-matched controls and patients with atherosclerosis and the
586 telomere length of the cells in the atherosclerotic plaques of the patients.[27] They found that
587 while telomere length in leukocytes from the atherosclerosis patient group was significantly
588 shorter than in the control group, telomere length in the atherosclerotic plaques was significantly

589 longer, indicative of increased telomerase activity. Thus, total leukocyte telomere length does
590 not represent telomere length in the diseased tissue. Our study investigated TERT protein levels
591 directly in the valve tissue and patient-specific VICs. We determined that the expression levels
592 of TERT and osteogenic markers in CAVD tissue and cells were elevated, without changes in
593 telomere length, proliferation, and DNA damage markers (Figures 1-2, Supplemental Figures 1-
594 4), suggesting non-canonical TERT activity in these cells.
595
596 VIC calcification shares aspects of the transcriptional program observed during the
597 differentiation of MSCs into osteoblasts, including the upregulation of *RUNX2, BGLAP, TNAP*,
598 and the secretion of bone-forming proteins and accumulation of calcium minerals.[10,12,83]
599 Likewise, signals such as mechanical stress, disturbed flow, and inflammation promote VIC
600 calcification and the osteogenic differentiation of MSCs.[84] These observations suggest that VICs
601 switch from their quiescent state and undergo an osteogenic reprogramming akin to the
602 differentiation of MSCs into osteoblasts, acquiring a calcifying phenotype. The mechanisms
603 coordinating the early molecular events in these cell transitions have yet to be fully understood.
604 We have hypothesized that fully differentiated cells can de-differentiate into a transitory,
605 multipotent stem cell-like state and then acquire an osteogenic phenotype.[85] VICs exhibit the
606 potential to differentiate into osteogenic, chondrogenic, or adipogenic lineages, properties
607 comparable to mesenchymal stem cells.[86] We chose to investigate TERT in the osteogenic
608 reprogramming of VICs as TERT is highly expressed in stem cells, and its overexpression
609 primes mesenchymal stem cells into the osteogenic lineage.[21,22] Our data supports the role of
610 TERT in the osteogenic reprogramming of VICs, whereby TERT serves as a bridge between
611 DNA-binding transcription factors and chromatin remodeling enzymes.
612

613 The osteogenic differentiation of stem cells is orchestrated by RUNX2, which is also required for
614 the osteogenic reprogramming of valvular and vascular cells.[40,41] In a recent transcriptomic
615 study, Xu et al. identified 14 cell populations in aortic valve tissue samples from two control and
616 four CAVD valves.[87] The severity of CAVD was assessed via ultrasound imaging, which detects
617 leaflet mobility; however, examining the macroscopic pictures and histological staining of valve
618 leaflets used in this analysis shows that while these valves are indeed stiff, they do not exhibit
619 robust nodules of calcification as do the valves in our data set (Figures 1, 5, and Supplemental
620 Figure 1). Analysis by Xu et al identified three VIC populations defined by expression of *FOS,*
621 *HSPA6, and SPARC.* However, cells from six valves were pooled, with 10.4% of cells from
622 control tissue and the remaining 89.6% from CAVD tissues. Bulk transcriptomic data from these
623 tissues show only a small 1.49-fold increase in *RUNX2* gene expression in CAVD tissues, in
624 stark contrast with our more stringent analysis of *RUNX2* expression by quantitative PCR
625 (Figure 2, Supplemental Figure 4).[10-12] Inspection of the publicly available bulk RNA-sequencing
626 data (PRJNA552159) showed no increase in *TERT* transcript expression. While the
627 hemodynamic data showed those valves had undergone fibrotic remodeling, few calcifying cells
628 were present, as seen by their histological staining. This lack of calcification may explain why
629 TERT expression was undetected in their study. In the general population, aortic sclerosis
630 commonly goes undetected until a patient develops symptoms such as dyspnea, angina, and
631 syncope, as the stiffness and remodeling of the leaflet obstructs ventricular outflow. A
632 population-based study assessed aortic valve disease in 552 randomly selected men and
633 women aged 55 to 86. Using imaging and Doppler echocardiography, mild calcification was
634 observed in 40% of the individuals, severe calcification in 13%, and symptomatic stenosis in
635 only 2.2%.[88] This population-based study illustrates how common aortic valve remodeling is and
636 highlights the importance of using multiple modalities to accurately determine valve pathology
637 (i.e., fibrotic vs calcified). In our study, a portion of each patient valve was used for cell isolation

638 while the rest was utilized for calcification assessment by histological staining, following a
639 workflow that we developed that guarantees that cells isolated from surgically removed and
640 postmortem tissues retain their proliferative capacity and endothelial and interstitial phenotypes
641 in culture.[37] While unbiased sequencing approaches may help uncover novel mechanisms
642 contributing to disease states, they are skewed towards genes exhibiting the largest changes in
643 gene expression in a snapshot of time and can miss short-lived transitory events.
644
645 The function of STAT5 in bone formation is multifaceted. While it was shown that STAT5 could
646 promote the differentiation of MSCs into osteoblasts by upregulating the osteogenic genes in a
647 Jak2-dependent manner, a *Stat5a* global knockout mouse exhibited elevated bone mass and
648 mineral density.[89,90] These conflicting reports indicate that the role of STAT5 in bone formation
649 and remodeling is complex, and more studies are required. STAT5 has diverse functions as a
650 transcription factor: it interacts with histone acetyltransferases and transcription factors such as
651 the glucocorticoid receptor, SP1, YY1, and C/EBPβ to stimulate gene expression,[91-93] and
652 studies in cancer cells identified that STAT5 can induce *TERT* expression.[94,95] Using in silico
653 modeling we found multiple putative STAT5 binding sites in the *RUNX2* P1 promoter region,
654 which were confirmed with Ch-IP assays. This supports our hypothesis that STAT5/TERT acts
655 to initiate the osteogenic reprogramming of VICs, establishing a novel mechanism in CAVD
656 pathogenesis whereby TERT/STAT5 bind to each other and activate osteogenic gene
657 transcription, which drives the early events in cellular osteogenic reprogramming. Cell
658 phenotype reprogramming requires chromatin restructuring to allow for the transcription of
659 repressed genes. As observed in other cell types, we found TERT co-immunoprecipitated with
660 SMARCA4, as well as STAT5, and genetic depletion of TERT or STAT5 midway through the
661 OST assay (i.e., after d7) did not perturb the calcification of cells. Our observations strongly
662 supports that TERT complexes with SMARCA4 to remodel chromatin and with the STAT5

663 transcription factor to bind and activate *RUNX2* gene transcription. We explored the potential
664 physical direct interaction between TERT and STAT5, and we propose that the RNA binding
665 domain of TERT is the most likely candidate to interact with STAT5 (Supplemental Figure 5).
666 This location is of interest, as we found that *Terc*$^{-/-}$ *mVICs* robustly calcify; this begs the question
667 of whether the loss of *lncTERC* binding is what enables or regulates the non-canonical activities
668 of TERT. Studies identifying critical domains for interaction are currently ongoing.
669
670 The strengths of this study lie in the utilization of patient-specific tissues and cell lines generated
671 from valve leaflets, and the use mouse models and knockout cells for mechanistic studies.
672 While our results are robust, it is important to address the limitations of our study. Firstly, we
673 worked with a limited number of human samples obtained from age- and sex-matched donors.
674 Due to this limited sample size, we limited our statistical analyses to non-parametric analysis,
675 comparing two to four groups, and no mixed models were included. Regardless, one strength of
676 our study is the multiprong approach to determining the role of TERT and STAT5 in vascular
677 calcification. Secondly, STAT5A and STAT5B are two different genes, with 96% of their amino
678 acid sequence shared and their activities redundant.[32] We have determined that VICs express
679 both variants; however, our antibodies and shRNA constructs could not differentiate between
680 the two variants. Thus, the two isoforms may interact with TERT to bind the *RUNX2* gene
681 promoter. STAT5 is activated by multiple cytokines, including IL-2, IL-6, and TNF-α, and it was
682 shown that IL-2 specifically activates STAT5 to induce TERT expression in cancer cells.[94,96]
683 Whether STAT5 first induces TERT expression and then TERT and STAT5 cooperate to control
684 the expression of *RUNX2* needs to be determined. Thirdly, there is redundancy regarding
685 STAT1/3/5 functions and signaling.[97] Our study was not designed to address all the
686 complexities of STAT signaling per se but rather to investigate the role of TERT as a key protein

687 that orchestrates the osteogenic reprogramming of aortic valve cells; our future studies will
688 explore the role of STAT5 further.
689
690 Our work highlights the importance of primary human tissue-based studies. Murine models are
691 not ideal for studying non-genetic drivers of CAVD, as mice do not develop CAVD de novo.[98,99]
692 Mouse leaflets' structure differs from human leaflets as they lack a trilaminar organization and
693 present a melanocyte cell population not present in human valves.[100-102] Recent elegant work
694 from the Giachelli group showed that in mice, calcification happens in the sinus wall and, to a
695 lesser extent, at the leaflet hinge, the region between the leaflet VICs and SMCs of the aorta,
696 with no detectable calcification in the aortic valve leaflets after 26 weeks of a high-fat diet in a
697 *Ldlr* knockout mice model.[103] This distribution of aortic root calcification is also observed in a
698 mouse model described by a Honda et al which detected calcification in the sinus wall 16 weeks
699 post wire-induced mechanical injury.[98] Due to the lack of aortic valve leaflet calcification in
700 atherosclerotic or mechanical injury murine models, we utilized a adenine/phosphate diet-
701 induced model of medial arterial calcification (MAC).[58] MAC is not associated with lipid
702 deposition, fibrous cap formation, or intimal hyperplasia; instead, MAC stems from the
703 progressive accumulation of calcium and phosphate within the arterial walls.[104] These structural
704 features distinguish MAC from atherosclerosis and are more representative of the pathogenesis
705 of valve leaflet calcification.[2,104]
706
707 This study has uncovered the early molecular events that enable the osteogenic reprogramming
708 of the interstitial cells of the aortic valve. Current CAVD therapies are surgical, limited to
709 mechanical or bioprosthetic valve replacement, and performed only when the disease has
710 progressed to the advanced point of affecting blood flow and heart function. Our data show that
711 perturbing TERT or STAT5 can inhibit calcification; however, broadly inhibiting one or the other

712 of these proteins may have deleterious off-target effects. Understanding the specific binding
713 domains and other protein binding partners of TERT and STAT5 will enable the development of
714 small molecules to block their interaction, which is a more feasible therapeutic strategy for aortic
715 valve calcification than global inhibition. CAVD affects over 9.5 million people in the U.S. and
716 has an associated 56-67% 5-year mortality rate; hence, the need for early, non-surgical
717 therapies is great.[4] This study uncovers a novel and targetable pathway that may be leveraged
718 to halt or prevent CAVD progression.
719

720 **ACKNOWLEDGEMENTS**

721 We want to acknowledge and thank the Center for Organ Research and Education for their help
722 and support, as well as tissue donors and their families for making this study possible. We thank
723 Dr. Alison Tebo for her guidance and assistance in constructing the SplitFAST plasmids tool
724 used in this study. We would also like to thank Kristin Konopka, tissue bank coordinator at The
725 Department of Cardiothoracic Surgery, UPMC. We thank Jason Dobbins for his critical reading
726 of this manuscript.
727

728 **SOURCES OF FUNDING**

729 This study was supported by funds from the National Institutes of Health (R01 HL142932, R56
730 HL168657, St. Hilaire), the American Heart Association (20IPA35260111, St. Hilaire; 902641,
731 Cuevas; 24POST1186619, Behzadi), the McKamish Family Foundation (St. Hilaire and Sultan)
732 and the Samuel and Emma Winters Foundation (St. Hilaire).
733

734 **DISCLOSURES**

735 The University of Pittsburgh has filed a provisional patent application regarding technology on
736 behalf of CSH and RAC based on the findings presented in this manuscript. IS receives

737 institutional research support from Atricure and Medtronic and is a consultant for Medtronic
738 Vascular. None of these conflicts of interest are related to this work. All other authors have nothing
739 to disclose.
740
741 **FIGURE LEGENDS**
742 **Figure 1. TERT is elevated in CAVD tissues.** (A) Examples of non-calcified control (top) and
743 calcified CAVD (bottom) human valves used in this study. Arrowheads indicate calcified nodules
744 Scalebar. 1 cm. (B), TERT mRNA transcript quantification in control and CAVD valve tissues. n
745 = 8 control, n= 9 CAVD. (C), Representative serial sections of Von Kossa (dark precipitation)
746 and TERT immunofluorescent staining in control and CAVD valve tissues. Scalebar 100 µm.
747 Graphs show the quantification of TERT intensity and the number of TERT-positive cells. n = 9
748 control, n = 9 CAVD. (D), Telomere length measurements in valve tissues. n = 19 control, n =
749 12 CAVD. (E), Age of the patients utilized in this study. n = 25 control, n = 16 CAVD. Data are
750 shown as means ± SD. P values were calculated using the Mann-Whitney U test and shown on
751 each graph. L = lumen.
752
753 **Figure 2. TERT is elevated in CAVD hVICs at baseline and upregulation during**
754 **osteogenic reprogramming.** (A), Representative images showing cell morphology of control
755 and CAVD hVICs. Scalebar 50 µm. (B), Proliferation of control and CAVD hVICs at baseline. n
756 = 3 both groups. (C) Relative migration distances of control and CAVD VICs. n = 10 both
757 groups. (D) Western blot staining of control and CAVD hVICs at baseline. Quantification of
758 protein levels is shown on the right panels. n = 4 both groups. (E) Telomere length
759 measurements in VICs. n = 8, control, n = 5 CAVD. (F) Representative images of early
760 calcification in hVICs growing in normal conditions (no treatment NT) or stimulated with
761 osteogenic media (OST) for 14 days. Calcium deposition was visualized by Alizarin Red

762 staining. Scalebar 50 µm. Quantification of calcification on the right graphs. n = 7 both groups.
763 (G), Western blot staining of samples from control and CAVD hVICs after 14 days of NT or
764 OST. Quantification of protein levels is shown on the bottom graphs. n = 4 both groups. (H),
765 Representative immunofluorescent staining images of TERT in control and CAVD hVICs after
766 14 days of NT or OST. Calcium deposition was visualized with OsteoImage. Scalebar 100 µm.
767 (I) Expression profile control VICs after 14 days of NT and OST treatment. n = 4 both groups.
768 Data are shown as means ± SD. P values were calculated with the Mann-Whitney U test
769 (Figures B, C, D, E, G, and I) and the Kruskal-Wallis H test with Dunn post hoc test (Figure F)
770 and shown on each graph
771
772 **Figure 3. TERT is required to initiate osteogenic transition and calcification.** (A) Control
773 hVICs were transduced lentivirus containing shControl or shTERT and followed by OST
774 stimulation for up to 28 days. Calcium deposition was visualized by Alizarin Red staining. n = 6
775 shControl, n = 6 shTERT at 21 days and n = 9 each group at day 28. Scalebar 400 µm. (B)
776 Representative western blot staining of control hVICs transduced with lentivirus containing
777 either shControl or shTERT followed by 7 days of OST. (C) hCASMCs were transduced with
778 shControl or shTERT and stimulated with OST for 14 and 21 days. n = 4 for each group at both
779 time points. Scalebar 400 µm. (D) Representative images of mVIC isolated from *Tert*$^{+/+}$ and *Tert*$^{-}$
780 $^{/-}$ mice were stimulated with OST for 28 days. Scalebar 400 µm. (E) Representative Von Kossa
781 staining images of *Tert*$^{+/+}$ and *Tert*$^{-/-}$ mice aortas (dark precipitation). Scale bar 400 µm.
782 Quantification of calcification is shown on the right panel. (F) Representative immunofluorescent
783 images of Runx2 expression indicative of calcification (red, insert) on *Tert*$^{+/+}$ and *Tert*$^{-/-}$ mice
784 aorta. Scale bar 400 *µ*m. Runx2 quantification of calcification is shown on the right panel. (G)
785 Representative images of mVICs isolated from F1 *Tert*$^{-/-}$ *or Terc*$^{-/-}$ mice were stimulated with
786 OST for up to 21 days. Scalebar 100 µm. Data are shown as means ± SD. P values were

787 calculated using the Kruskal-Wallis H test, Dunn post hoc test (Figures A, C, and G), and Mann-
788 Whitney U test (Figures D, E, and F).
789
790 **Figure 4. STAT5 binds to TERT and is required for the calcification of human VICs.** (A)
791 Graphic of in silico analysis identifying the consensus binding site for STAT5. (B), Diagram
792 depicting STAT5 binding to RUNX2 promoter and the positions of the predicted STAT5 binding
793 sites (purple boxes). (C) Representative immunofluorescence images of control hVICs after 14
794 days of LPS treatment or OST stimulation. Scalebar 50 µm. (D) Representative western blot
795 staining of hVICs after 14 days of OST stimulation. (E) Representative images of control hVICs
796 treated with 10 µM of the STAT5 inhibitors StafiA-1 or StafiB-1 throughout 28 days of
797 osteogenic stimulation. Scalebar 400 µm. n = 8 each group. The quantification of calcification is
798 shown on the right graph. (F) RUNX2 mRNA transcript quantification at d7 OST, n = 10. (G)
799 Control hVICs were transduced with lentivirus containing shControl or shSTAT5 constructs and
800 treated with OST for 21 days. Calcium deposition was visualized by Alizarin Red staining. n = 9
801 for each group. Scalebar 400 µm. (H) RUNX2 mRNA transcript quantification at d7 OST, n = 6.
802 (I) Schematic of OST treatment with delayed shTERT transduction (top panel).Representative
803 images of hVIC (left panels) treated with 10 µM of the STAT5 inhibitors StafiA-1 at d7 or d14 of
804 OST treatment. Samples were collected at d21 (bottom panel). Scalebar 400 µm. n = 6 for each
805 group. (J) Representative images of TERT/STAT5 complex (red foci) in control hVICs cultured
806 for 21 days in osteogenic medium and detected by PLA. Scalebar 100 µm. n = 4 for each group.
807 (K) STAT5 co-immunoprecipitation in control hVICs under OST for 10 days to detect
808 TERT/STAT5 interaction. (L) Control hVIC co-expressing TERT-NFAST and STAT5A-CFAST
809 were labeled with 5 µM HBR-3,5DOM (4-hydroxy-3,5- dimethoxybenzylidene rhodamine, coral)
810 and imaged at d3, d5, and d7 of osteogenic treatment (OST) or control no-treatment (NT). Scale
811 bars 50 µm. (M) Chromatin immunoprecipitation shows enrichment of STAT5 on RUNX2

812 promoter OST conditions compared to NT. The base position is indicated in the blue boxes. n=4
813 for each group as in B. (N) STAT5 CUT&Tag sequencing tracks in genomic regions of Runx2 in
814 no-treatment control and osteogenic condition-treated mice VICs. (O) Stacked chart
815 representing genome-wide STAT5 occupancy in promoters, genes, and intergenic regions
816 frequency in mice VICs. (P) Top 20 GO pathways enriched in genes with significant loss of
817 STAT5 in Tert+/+ vs Tert-/- mice VICs. Data are shown as means ± SD. P values were
818 calculated by the Mann-Whitney U test (Figures F, H, and J) and the Kruskal-Wallis H test
819 (Figures E and G) and indicated on top of each graph.
820
821 **Figure 5. TERT and STAT5 are upregulated and colocalized in CAVD tissue.** (A)
822 Representative serial sections of Von Kossa (dark precipitation) and TERT and STAT5
823 immunofluorescent staining in control and CAVD tissues. Scalebar 100 µm. STAT5 intensity
824 and STAT5-positive cells (STAT5+) are quantified on the right panels. (B) Quantification of
825 STAT5-TERT-positive cells. Data are shown as means ± SD, n = 5 control, n = 6 CAVD. P
826 values were calculated with the Mann-Whitney U test and indicated on each graph. L = lumen.
827
828 **Figure 6. TERT/STAT5 promotes osteogenic reprogramming.** Inflammatory signals promote
829 the upregulation and interaction of TERT and STAT5A. The TERT/STAT5 complex translocates
830 into the nucleus, where TERT interacts with SMARCA4 (also known as BRG1), which facilitates
831 a permissive chromatin configuration, and STAT5A binds specific sites on the RUNX2 promoter,
832 leading to the osteogenic reprogramming of valve interstitial cells during the early stages of
833 CAVD pathogenesis.
834
835 **Supplemental Figure 1. Characterization of human CAVD valves and patient-isolated**
836 **VICs at baseline.** (A) Representative section of Von Kossa staining in control and valve CAVD

837 leaflets tissue. Scalebar 1 mm. (B) Representative serial sections of RUNX2 immunofluorescent
838 staining and OPN in control and CAVD valve tissues. Scalebar 100 µm. Quantification of
839 RUNX2-positive cells and OPN-positive cells on the leaflet specimen is shown on the right
840 graphs. n = 5 control, n = 6 CAVD. (C) Correlation between age of the donor and TERT
841 expression in valve tissues. n = 8 control, n = 9 CAVD. (D) Gene expression profile in the valve
842 leaflets. n = 7 each group. (E) Representative images of immunofluorescent staining of PCNA
843 (top panels) and γ-H2AX (bottom panels) in control and CAVD valve tissues. Scalebar 100 µm.
844 Quantification of PCNA-positive cells and γ-H2AX-positive cells are shown on the right graphs.
845 n = 4 control, n = 3 CAVD. (F) Representative images of a scratch assay in control and CAVD
846 hVICs. Time points are indicated on top of each panel. Blue lines denote the cell migration front.
847 Scalebar 1 mm. n = 10 of each group. (G) Representative images of αSMA, CNN, SM22, TNAP,
848 and f-Actin in control and CAVD hVICs. Scalebar 50 µm. Signal quantification is shown on the
849 right. n = 4 each group. Data are shown as means ± SD. P values were calculated using the
850 Mann-Whitney U test (Figures B, D, E, and G) and the Pearson correlation test (Figure C). L =
851 lumen.
852
853 **Supplemental Figure 2. Inhibition of reverse transcriptase activity of TERT does not**
854 **prevent osteogenic reprogramming of hVICs**. (A) Cell counts of control and CAVD hVICs
855 after 14 days of NT or OST stimulation. n = 4 each group. (B) β-galactosidase (BLG1) mRNA
856 transcript quantification in control and CAVD hVICs at baseline. n = 5 control, n= 4 CAVD. (C)
857 Representative images of senescence-associated β-galactosidase activity staining of hVICs
858 after 28 days of NT or OST stimulation. Blue cells were considered positive for senescence.
859 Quantification of senescence is shown on the right graph. n = 4 each group. Scalebar 400 µm.
860 (D) hVICs growing in no treatment (NT), OST media, or OST media supplemented with the NF-
861 κβ inhibitor BAY-117082 for 7 days, n = 6. (E) hVICs growing in no treatment (NT), OST media,

862 or OST media supplemented with the c-MYC inhibitor 10058-F4 for 7 days, n = 7. qRT-PCR
863 quantified TERT and RUNX2 gene expression. In D and E, inhibitors were dissolved in DMSO
864 thus NT and OST were supplemented with the highest volume of vehicle (DMSO) used in
865 treatment groups. Data are shown as means ± SD. P values were calculated with the Mann-
866 Whitney U test (Figure B) and the Kruskal-Wallis H test with Dunn pairwise comparison post hoc
867 test (Figures A, C-E) and shown on top of each graph.
868
869 **Supplemental Figure 3. TERT is upregulated and required for the osteogenic**
870 **differentiation of human mesenchymal stem cells**. (A) Representative images of hMSCs
871 stimulated with OST for 14 days. Calcium deposition was visualized by Alizarin Red staining.
872 Scalebar 50 µm. (B) Western blot staining of samples from hMSCs collected during the 14 days
873 of OST treatment. (C) RUNX2 expression profile of differentiating hMSCs stimulated for 14 days
874 with OST media. n = 3. (D) Representative TERT immunofluorescent staining images of hMSCs
875 stimulated with OST for 14 days. Scalebar 100 µm. (E) Representative images of hMSCs
876 infected with shTERT or shControl virus and stimulated with OST for 14 days. Calcium
877 deposition was visualized by Alizarin Red staining. The quantification of calcification is shown
878 on the right graph. n = 3. (F) Western blot staining of samples from hMSCs collected during the
879 14 days of OST treatment. Data are shown as means ± SD. P values were calculated with the
880 Kruskal-Wallis H test with Dunn pairwise comparison post hoc test (Figure C) and the Mann-
881 Whitney U test (Figure E) and shown on each graph.
882
883 **Supplemental Figure 4. Inhibition of reverse transcriptase activity of TERT does not**
884 **prevent osteogenic reprogramming of VICs.** (A) Representative images of mBMMSCs
885 isolated from *Tert*$^{+/+}$ or *Tert*$^{-/-}$ mice and stimulated with OST for 21 days. Scalebar 100 µm.
886 Quantification of calcification is presented as average absorbance on the right graphs, n = 5 for

887 each group. (B, C) Representative images of a senescence-associated β-galactosidase (SA-β-
888 gal) staining of mVICs and mBMMSCs isolated from *Tert*$^{+/+}$ or F1 *Tert*$^{-/-}$ mice after 21 days of
889 OST stimulation. In each group, blue cells were considered positive for senescence, n = 5. (D)
890 Schematic of OST treatment with delayed shTERT transduction (top panel). VICs were
891 transduced with shTERT, and calcification was assessed with Alizarin Red S stain at day 21.
892 Scalebar 400 µm. n = 6 for each group. (E) Representative sections of Von Kossa staining in
893 thoracic aortic rings isolated from *Tert*$^{+/+}$ and *Tert*$^{-/-}$ mice after 14 days of OST treatment relative
894 to NT control treatment. Quantification is shown on the right. Scale bar 400 *µ*m (F)
895 Immunofluorescence staining of thoracic aortic rings after OST treatment as in B. Quantification
896 of Runx2 is shown on the right graph. Scale bar 400 *µ*m (G) Western blot staining of aortic ring
897 specimens collected and treated in B. Quantification of Runx2 is shown on the right graph. (H)
898 Human VICs were treated with the TERT inhibitor BiBR1532 and stimulated with OST, and
899 calcification was assessed on day 28, with n = 5 in each group. (I) TERT, RUNX2, and STAT5A
900 expression were evaluated on day 14, n = 6 DMSO, n = 5 BIBR1532. Data are shown as means
901 ± SD. P values were calculated with the Kruskal-Wallis H test with Dunn pairwise comparison
902 post hoc test (Figures A, B, C, E, H) and the Mann-Whitney U test (Figures D, F, G, I) and are
903 shown on top of each graph.
904
905 **Supplemental Figure 5. STAT5 is upregulated, binds to TERT, and is required for**
906 **osteogenic reprogramming of VICs.** (A) Western blot analysis of cytoplasmic and nuclear
907 fractions of TERT from control VICs obtained after seven days of OST stimulation. TUB,
908 (tubuline); H3, (Histone H3); Cyt, cytoplasmic fraction; Nuc, nuclear fraction. (B) Representative
909 immunofluorescence image of STAT5 subcellular distribution after 14 days of NT and OST
910 stimulation. Scalebar 40 µm. (C) Representative images of human CASMCs treated with 10 µM
911 of the STAT5 inhibitors StafiA-1 or StafiB-1 during the 14 days of OST stimulation. Scalebar 400

912 µm. n = 4 for each group. (D) Representative images of human MSCs treated with 10 µM of the
913 STAT5 inhibitors StafiA-1 or StafiB-1 during the 21 days of OST stimulation. Scalebar 400 µm. n
914 = 4 for each group. (E) Representative images of TERT/STAT5 complex (red foci) detected by
915 proximity ligation assay (PLA) in the nucleus of control VICs. Scalebar 25 µm. n = 4 for each
916 group. (F) Relative luciferase activity in hVICS after transfection of *hRUNX2* Promoter GLuc-ON
917 pEZX-PG04.1. Samples were analyzed 72 hours after OST treatment. STAT5A inhibitor StafiA-
918 1 (10 µM) was dissolved in DMSO. NT and OST conditions were also supplemented with
919 DMSO, n = 10 per group. (G) Biotin-labeled 60 bp oligos containing the -194 STAT5 binding
920 sequence on the promoter of human RUNX2 were incubated cell extracts from HEK293s in
921 which STAT5 protein was overexpressed (lane 1). Extracts were also incubated with an
922 increasing amounts of unlabeled oligos (lanes 2-5). Cell extract was also incubated with a oligo
923 containing a mutated STAT5A site (mut RUNX2 DNA) (line 9) and incubated with an increased
924 amount of unlabeled mut RUNX2 oligo (lanes 10-13). Blots include the positive and negative
925 controls include in the LightShift Chemiluminescent EMSA Kit (lanes 6-8 and 14-16). (H)
926 Representative immunofluorescent images of Stat5 expression after 12 weeks of high adenine
927 high phosphate diet on Tert-/- and Tert-/- mice aorta. Scale bar 400 μm. Quantification of Stat5
928 expression is shown on the right panel. (I) Representative images of Stat5 immunofluorescence
929 staining of thoracic aortic rings isolated from Tert+/+ and Tert-/- mice after 14 days of OST
930 treatment relative to NT control treatment. Quantification of Stat5 is shown on the right graph.
931 Scale bar 400 μm. (J) Mol*3D Viewer rendering of the TERT-STAT5 dimer interaction predicted
932 by the HDock. Red boxes indicate the position of the interaction between TERT and STAT5. (K)
933 The diagram shows the regions involved in the predicted interaction as indicated in A, and the
934 docking and confidence scores predicted by HDock are indicated. TEN: DNA anchor domain for
935 processive telomeric repeat addition, RBD: Telomerase RNA binding domain, RT: Finger and
936 palm region of the reverse transcriptase domain, CTE: C-terminal extension or putative thumb

937 domain of the reverse transcriptase, CCD: Coiled-coil domain, required for nuclear localization,
938 DBD: DNA binding domain, HLK: Helical linker and DNA binding domain, SH2: Domain required
939 for activation and dimerization, TD: Transactivation domain. (L) H3K4me3 CUT&Run
940 sequencing tracks in genomic regions of Runx2 in no-treatment control and osteogenic
941 condition-treated human VICs. (M) Top 20 GO pathways enriched in genes with significant loss
942 of H3K4me3 in OST- vs NT-treated human VICs. Data are shown as means ± SD. P values
943 were calculated with the Mann-Whitney U test (Figures E and G) and the Kruskal-Wallis H test
944 with Dunn pairwise comparison post-test (Figures C, D, and H) and indicated in each graph.
945
946 **Supplemental Figure 6. Chromatin remodeling enzyme SMARCA4 is upregulated and**
947 **interacts with TERT during the osteogenic reprogramming of VICs.** (A) Representative
948 immunofluorescent images of Smarca4 expression after 12 weeks of high adenine high
949 phosphate diet on *Tert*$^{-/-}$ and *Tert*$^{-/-}$ mice aorta. Scale bar 400 μm. Quantification of Smarca4
950 expression is shown on the right panel. (B) Representative images of Smarca4
951 immunofluorescence staining of thoracic aortic rings isolated from *Tert*$^{+/+}$ and *Tert*$^{-/-}$ mice after
952 14 days of OST treatment relative to NT control treatment. Quantification of Smarca4 is shown
953 on the right graph. (C) SMARCA4 expression was evaluated on days 5 and 10 on VICs
954 stimulated with OST. n = 5 each group. (E) TERT/STAT and TERT/SMARCA4 interaction was
955 detected by co-immunoprecipitation upon osteogenic stimulation on VIC. (E) Representative
956 TERT and SMARCA4 immunofluorescent staining in control and CAVD tissues. The number of
957 positive cells is shown on the right graphs. n = 9 control, n = 9 CAVD. Scalebar 100 µm. Data
958 are shown as means ± SD, and P values were calculated with the Mann-Whitney U test and
959 indicated on each graph in Figures A and C. L = lumen.
960
961 **REFERENCES**

962 1. Kraler S, Blaser MC, Aikawa E, Camici GG, Luscher TF. Calcific aortic valve disease:
963 from molecular and cellular mechanisms to medical therapy. *Eur Heart J*. 2022;43:683-
964 697. doi: 10.1093/eurheartj/ehab757
965 2. Small AM, Yutzey KE, Binstadt BA, Voigts Key K, Bouatia-Naji N, Milan D, Aikawa E,
966 Otto CM, St Hilaire C, American Heart Association Council on G, et al. Unraveling the
967 Mechanisms of Valvular Heart Disease to Identify Medical Therapy Targets: A Scientific
968 Statement From the American Heart Association. *Circulation*. 2024;150:e109-e128. doi:
969 10.1161/CIR.0000000000001254
970 3. Buttner P, Feistner L, Lurz P, Thiele H, Hutcheson JD, Schlotter F. Dissecting Calcific
971 Aortic Valve Disease-The Role, Etiology, and Drivers of Valvular Fibrosis. *Front*
972 *Cardiovasc Med*. 2021;8:660797. doi: 10.3389/fcvm.2021.660797
973 4. Coffey S, Roberts-Thomson R, Brown A, Carapetis J, Chen M, Enriquez-Sarano M,
974 Zuhlke L, Prendergast BD. Global epidemiology of valvular heart disease. *Nat Rev*
975 *Cardiol*. 2021;18:853-864. doi: 10.1038/s41569-021-00570-z
976 5. Roth GA, Mensah GA, Johnson CO, Addolorato G, Ammirati E, Baddour LM, Barengo
977 NC, Beaton AZ, Benjamin EJ, Benziger CP, et al. Global Burden of Cardiovascular
978 Diseases and Risk Factors, 1990-2019: Update From the GBD 2019 Study. *J Am Coll*
979 *Cardiol*. 2020;76:2982-3021. doi: 10.1016/j.jacc.2020.11.010
980 6. Virani SS, Alonso A, Benjamin EJ, Bittencourt MS, Callaway CW, Carson AP,
981 Chamberlain AM, Chang AR, Cheng S, Delling FN, et al. Heart Disease and Stroke
982 Statistics-2020 Update: A Report From the American Heart Association. *Circulation*.
983 2020;141:e139-e596. doi: 10.1161/CIR.0000000000000757
984 7. Rajamannan NM, Evans FJ, Aikawa E, Grande-Allen KJ, Demer LL, Heistad DD,
985 Simmons CA, Masters KS, Mathieu P, O'Brien KD, et al. Calcific aortic valve disease:
986 not simply a degenerative process: A review and agenda for research from the National
987 Heart and Lung and Blood Institute Aortic Stenosis Working Group. Executive summary:
988 Calcific aortic valve disease-2011 update. *Circulation*. 2011;124:1783-1791. doi:
989 10.1161/CIRCULATIONAHA.110.006767
990 8. Chen JH, Simmons CA. Cell-matrix interactions in the pathobiology of calcific aortic
991 valve disease: critical roles for matricellular, matricrine, and matrix mechanics cues. *Circ*
992 *Res*. 2011;108:1510-1524. doi: 10.1161/CIRCRESAHA.110.234237

993 9. Liu AC, Joag VR, Gotlieb AI. The emerging role of valve interstitial cell phenotypes in
994 regulating heart valve pathobiology. *Am J Pathol*. 2007;171:1407-1418. doi:
995 10.2353/ajpath.2007.070251
996 10. Rajamannan NM, Subramaniam M, Rickard D, Stock SR, Donovan J, Springett M,
997 Orszulak T, Fullerton DA, Tajik AJ, Bonow RO, et al. Human aortic valve calcification is
998 associated with an osteoblast phenotype. *Circulation*. 2003;107:2181-2184. doi:
999 10.1161/01.CIR.0000070591.21548.69
1000 11. Rajamannan NM. Calcific aortic valve disease: cellular origins of valve calcification.
1001 *Arterioscler Thromb Vasc Biol*. 2011;31:2777-2778. doi: 10.1161/ATVBAHA.111.237610
1002 12. Aikawa E, Libby P. A Rock and a Hard Place: Chiseling Away at the Multiple
1003 Mechanisms of Aortic Stenosis. *Circulation*. 2017;135:1951-1955. doi:
1004 10.1161/CIRCULATIONAHA.117.027776
1005 13. Wirrig EE, Yutzey KE. Conserved transcriptional regulatory mechanisms in aortic valve
1006 development and disease. *Arterioscler Thromb Vasc Biol*. 2014;34:737-741. doi:
1007 10.1161/ATVBAHA.113.302071
1008 14. Calado RT, Young NS. Telomere diseases. *N Engl J Med*. 2009;361:2353-2365. doi:
1009 10.1056/NEJMra0903373
1010 15. Stewart SA, Hahn WC, O'Connor BF, Banner EN, Lundberg AS, Modha P, Mizuno H,
1011 Brooks MW, Fleming M, Zimonjic DB, et al. Telomerase contributes to tumorigenesis by
1012 a telomere length-independent mechanism. *Proc Natl Acad Sci U S A*. 2002;99:12606-
1013 12611. doi: 10.1073/pnas.182407599
1014 16. Choi J, Southworth LK, Sarin KY, Venteicher AS, Ma W, Chang W, Cheung P, Jun S,
1015 Artandi MK, Shah N, et al. TERT promotes epithelial proliferation through transcriptional
1016 control of a Myc- and Wnt-related developmental program. *PLoS Genet*. 2008;4:e10.
1017 doi: 10.1371/journal.pgen.0040010
1018 17. Masutomi K, Possemato R, Wong JM, Currier JL, Tothova Z, Manola JB, Ganesan S,
1019 Lansdorp PM, Collins K, Hahn WC. The telomerase reverse transcriptase regulates
1020 chromatin state and DNA damage responses. *Proc Natl Acad Sci U S A*.
1021 2005;102:8222-8227. doi: 10.1073/pnas.0503095102
1022 18. Park JI, Venteicher AS, Hong JY, Choi J, Jun S, Shkreli M, Chang W, Meng Z, Cheung
1023 P, Ji H, et al. Telomerase modulates Wnt signalling by association with target gene
1024 chromatin. *Nature*. 2009;460:66-72. doi: 10.1038/nature08137

1025 19. Aono J, Ruiz-Rodriguez E, Qing H, Findeisen HM, Jones KL, Heywood EB, Bruemmer
1026 D. Telomerase Inhibition by Everolimus Suppresses Smooth Muscle Cell Proliferation
1027 and Neointima Formation Through Epigenetic Gene Silencing. *JACC Basic Transl Sci*.
1028 2016;1:49-60. doi: 10.1016/j.jacbts.2016.01.002
1029 20. Endorf EB, Qing H, Aono J, Terami N, Doyon G, Hyzny E, Jones KL, Findeisen HM,
1030 Bruemmer D. Telomerase Reverse Transcriptase Deficiency Prevents Neointima
1031 Formation Through Chromatin Silencing of E2F1 Target Genes. *Arterioscler Thromb*
1032 *Vasc Biol*. 2017;37:301-311. doi: 10.1161/ATVBAHA.116.308717
1033 21. Shi S, Gronthos S, Chen S, Reddi A, Counter CM, Robey PG, Wang CY. Bone
1034 formation by human postnatal bone marrow stromal stem cells is enhanced by
1035 telomerase expression. *Nat Biotechnol*. 2002;20:587-591. doi: 10.1038/nbt0602-587
1036 22. Simonsen JL, Rosada C, Serakinci N, Justesen J, Stenderup K, Rattan SI, Jensen TG,
1037 Kassem M. Telomerase expression extends the proliferative life-span and maintains the
1038 osteogenic potential of human bone marrow stromal cells. *Nat Biotechnol*. 2002;20:592-
1039 596. doi: 10.1038/nbt0602-592
1040 23. Slagboom PE, Droog S, Boomsma DI. Genetic determination of telomere size in
1041 humans: a twin study of three age groups. *Am J Hum Genet*. 1994;55:876-882.
1042 24. Brouilette S, Singh RK, Thompson JR, Goodall AH, Samani NJ. White cell telomere
1043 length and risk of premature myocardial infarction. *Arterioscler Thromb Vasc Biol*.
1044 2003;23:842-846. doi: 10.1161/01.ATV.0000067426.96344.32
1045 25. Samani NJ, Boultby R, Butler R, Thompson JR, Goodall AH. Telomere shortening in
1046 atherosclerosis. *Lancet*. 2001;358:472-473. doi: 10.1016/S0140-6736(01)05633-1
1047 26. Kurz DJ, Kloeckener-Gruissem B, Akhmedov A, Eberli FR, Buhler I, Berger W, Bertel O,
1048 Luscher TF. Degenerative aortic valve stenosis, but not coronary disease, is associated
1049 with shorter telomere length in the elderly. *Arterioscler Thromb Vasc Biol*. 2006;26:e114-
1050 117. doi: 10.1161/01.ATV.0000222961.24912.69
1051 27. Huzen J, Peeters W, de Boer RA, Moll FL, Wong LS, Codd V, de Kleijn DP, de Smet BJ,
1052 van Veldhuisen DJ, Samani NJ, et al. Circulating leukocyte and carotid atherosclerotic
1053 plaque telomere length: interrelation, association with plaque characteristics, and
1054 restenosis after endarterectomy. *Arterioscler Thromb Vasc Biol*. 2011;31:1219-1225. doi:
1055 10.1161/ATVBAHA.110.217158
1056 28. Evans MA, Walsh K. Clonal hematopoiesis, somatic mosaicism, and age-associated
1057 disease. *Physiol Rev*. 2023;103:649-716. doi: 10.1152/physrev.00004.2022

1058 29. Steinmetz M, Schmitter C, Radecke T, Stundl A, Nickenig G, Schaefer C, Schahab N,
1059 Vasa-Nicotera M, Sinning JM. Brief report - Telomere length is a poor biomarker to
1060 predict 1-year mortality or cardiovascular comorbidity in patients with transcatheter aortic
1061 valve replacement. *PLoS One*. 2019;14:e0213250. doi: 10.1371/journal.pone.0213250
1062 30. Leonard WJ, O'Shea JJ. Jaks and STATs: biological implications. *Annu Rev Immunol*.
1063 1998;16:293-322. doi: 10.1146/annurev.immunol.16.1.293
1064 31. Hu X, Li J, Fu M, Zhao X, Wang W. The JAK/STAT signaling pathway: from bench to
1065 clinic. *Signal Transduct Target Ther*. 2021;6:402. doi: 10.1038/s41392-021-00791-1
1066 32. Okutani Y, Kitanaka A, Tanaka T, Kamano H, Ohnishi H, Kubota Y, Ishida T, Takahara
1067 J. Src directly tyrosine-phosphorylates STAT5 on its activation site and is involved in
1068 erythropoietin-induced signaling pathway. *Oncogene*. 2001;20:6643-6650. doi:
1069 10.1038/sj.onc.1204807
1070 33. Wingelhofer B, Neubauer HA, Valent P, Han X, Constantinescu SN, Gunning PT, Muller
1071 M, Moriggl R. Implications of STAT3 and STAT5 signaling on gene regulation and
1072 chromatin remodeling in hematopoietic cancer. *Leukemia*. 2018;32:1713-1726. doi:
1073 10.1038/s41375-018-0117-x
1074 34. Gu L, Liao Z, Hoang DT, Dagvadorj A, Gupta S, Blackmon S, Ellsworth E, Talati P, Leiby
1075 B, Zinda M, et al. Pharmacologic inhibition of Jak2-Stat5 signaling By Jak2 inhibitor
1076 AZD1480 potently suppresses growth of both primary and castrate-resistant prostate
1077 cancer. *Clin Cancer Res*. 2013;19:5658-5674. doi: 10.1158/1078-0432.CCR-13-0422
1078 35. Dieudonne FX, Severe N, Biosse-Duplan M, Weng JJ, Su Y, Marie PJ. Promotion of
1079 osteoblast differentiation in mesenchymal cells through Cbl-mediated control of STAT5
1080 activity. *Stem Cells*. 2013;31:1340-1349. doi: 10.1002/stem.1380
1081 36. Wu X, Chen C, Han T, Bian H, Chen J, Hei R, Meng Y, Wu C, Lu Y, Gu J, et al. Stat5a
1082 promotes Col10a1 gene expression during chondrocyte hypertrophic differentiation. *Am*
1083 *J Transl Res*. 2023;15:4006-4019.
1084 37. Cuevas RA, Chu CC, Moorhead WJ, 3rd, Wong R, Sultan I, St Hilaire C. Isolation of
1085 Human Primary Valve Cells for In vitro Disease Modeling. *J Vis Exp*. 2021:e62439. doi:
1086 10.3791/62439
1087 38. Ducy P, Zhang R, Geoffroy V, Ridall AL, Karsenty G. Osf2/Cbfa1: a transcriptional
1088 activator of osteoblast differentiation. *Cell*. 1997;89:747-754. doi: 10.1016/s0092-
1089 8674(00)80257-3

1090 39. Otto F, Thornell AP, Crompton T, Denzel A, Gilmour KC, Rosewell IR, Stamp GW,
1091 Beddington RS, Mundlos S, Olsen BR, et al. Cbfa1, a candidate gene for cleidocranial
1092 dysplasia syndrome, is essential for osteoblast differentiation and bone development.
1093 *Cell*. 1997;89:765-771. doi: 10.1016/s0092-8674(00)80259-7
1094 40. Sun Y, Byon CH, Yuan K, Chen J, Mao X, Heath JM, Javed A, Zhang K, Anderson PG,
1095 Chen Y. Smooth muscle cell-specific runx2 deficiency inhibits vascular calcification. *Circ*
1096 *Res*. 2012;111:543-552. doi: 10.1161/CIRCRESAHA.112.267237
1097 41. Lin ME, Chen T, Leaf EM, Speer MY, Giachelli CM. Runx2 Expression in Smooth
1098 Muscle Cells Is Required for Arterial Medial Calcification in Mice. *Am J Pathol*.
1099 2015;185:1958-1969. doi: 10.1016/j.ajpath.2015.03.020
1100 42. Parra-Izquierdo I, Castanos-Mollor I, Lopez J, Gomez C, San Roman JA, Sanchez
1101 Crespo M, Garcia-Rodriguez C. Calcification Induced by Type I Interferon in Human
1102 Aortic Valve Interstitial Cells Is Larger in Males and Blunted by a Janus Kinase Inhibitor.
1103 *Arterioscler Thromb Vasc Biol*. 2018;38:2148-2159. doi: 10.1161/ATVBAHA.118.311504
1104 43. Parra-Izquierdo I, Castanos-Mollor I, Lopez J, Gomez C, San Roman JA, Sanchez
1105 Crespo M, Garcia-Rodriguez C. Lipopolysaccharide and interferon-gamma team up to
1106 activate HIF-1alpha via STAT1 in normoxia and exhibit sex differences in human aortic
1107 valve interstitial cells. *Biochim Biophys Acta Mol Basis Dis*. 2019;1865:2168-2179. doi:
1108 10.1016/j.bbadis.2019.04.014
1109 44. Jin H, St Hilaire C, Huang Y, Yang D, Dmitrieva NI, Negro A, Schwartzbeck R, Liu Y, Yu
1110 Z, Walts A, et al. Increased activity of TNAP compensates for reduced adenosine
1111 production and promotes ectopic calcification in the genetic disease ACDC. *Sci Signal*.
1112 2016;9:ra121. doi: 10.1126/scisignal.aaf9109
1113 45. Moorhead WJ, 3rd, Chu CC, Cuevas RA, Callahan Jt, Wong R, Regan C, Boufford CK,
1114 Sur S, Liu M, Gomez D, et al. Dysregulation of FOXO1 (Forkhead Box O1 Protein)
1115 Drives Calcification in Arterial Calcification due to Deficiency of CD73 and Is Present in
1116 Peripheral Artery Disease. *Arterioscler Thromb Vasc Biol*. 2020;40:1680-1694. doi:
1117 10.1161/ATVBAHA.119.313765
1118 46. Jung JJ, Razavian M, Kim HY, Ye Y, Golestani R, Toczek J, Zhang J, Sadeghi MM.
1119 Matrix metalloproteinase inhibitor, doxycycline and progression of calcific aortic valve
1120 disease in hyperlipidemic mice. *Sci Rep*. 2016;6:32659. doi: 10.1038/srep32659
1121 47. Millan A, Lanzer P, Sorribas V. The Thermodynamics of Medial Vascular Calcification.
1122 *Front Cell Dev Biol*. 2021;9:633465. doi: 10.3389/fcell.2021.633465

1123 48. Kim NW, Piatyszek MA, Prowse KR, Harley CB, West MD, Ho PL, Coviello GM, Wright
1124 WE, Weinrich SL, Shay JW. Specific association of human telomerase activity with
1125 immortal cells and cancer. *Science*. 1994;266:2011-2015. doi: 10.1126/science.7605428
1126 49. Hao LY, Armanios M, Strong MA, Karim B, Feldser DM, Huso D, Greider CW. Short
1127 telomeres, even in the presence of telomerase, limit tissue renewal capacity. *Cell*.
1128 2005;123:1121-1131. doi: 10.1016/j.cell.2005.11.020
1129 50. Bu DX, Johansson ME, Ren J, Xu DW, Johnson FB, Edfeldt K, Yan ZQ. Nuclear factor
1130 kappaB-mediated transactivation of telomerase prevents intimal smooth muscle cell from
1131 replicative senescence during vascular repair. *Arterioscler Thromb Vasc Biol*.
1132 2010;30:2604-2610. doi: 10.1161/ATVBAHA.110.213074
1133 51. Yuan X, Larsson C, Xu D. Mechanisms underlying the activation of TERT transcription
1134 and telomerase activity in human cancer: old actors and new players. *Oncogene*.
1135 2019;38:6172-6183. doi: 10.1038/s41388-019-0872-9
1136 52. Wu KJ, Grandori C, Amacker M, Simon-Vermot N, Polack A, Lingner J, Dalla-Favera R.
1137 Direct activation of TERT transcription by c-MYC. *Nat Genet*. 1999;21:220-224. doi:
1138 10.1038/6010
1139 53. Lee J, Rhee MH, Kim E, Cho JY. BAY 11-7082 is a broad-spectrum inhibitor with anti-
1140 inflammatory activity against multiple targets. *Mediators Inflamm*. 2012;2012:416036.
1141 doi: 10.1155/2012/416036
1142 54. Pierce JW, Schoenleber R, Jesmok G, Best J, Moore SA, Collins T, Gerritsen ME. Novel
1143 inhibitors of cytokine-induced IkappaBalpha phosphorylation and endothelial cell
1144 adhesion molecule expression show anti-inflammatory effects in vivo. *J Biol Chem*.
1145 1997;272:21096-21103. doi: 10.1074/jbc.272.34.21096
1146 55. Jin HY, Weir-McCall JR, Leipsic JA, Son JW, Sellers SL, Shao M, Blanke P, Ahmadi A,
1147 Hadamitzky M, Kim YJ, et al. The Relationship Between Coronary Calcification and the
1148 Natural History of Coronary Artery Disease. *JACC Cardiovasc Imaging*. 2021;14:233-
1149 242. doi: 10.1016/j.jcmg.2020.08.036
1150 56. Ogawa D, Nomiyama T, Nakamachi T, Heywood EB, Stone JF, Berger JP, Law RE,
1151 Bruemmer D. Activation of peroxisome proliferator-activated receptor gamma
1152 suppresses telomerase activity in vascular smooth muscle cells. *Circ Res*. 2006;98:e50-
1153 59. doi: 10.1161/01.RES.0000218271.93076.c3
1154 57. Chiang YJ, Hemann MT, Hathcock KS, Tessarollo L, Feigenbaum L, Hahn WC, Hodes
1155 RJ. Expression of telomerase RNA template, but not telomerase reverse transcriptase,

1156 is limiting for telomere length maintenance in vivo. *Mol Cell Biol*. 2004;24:7024-7031.
1157 doi: 10.1128/MCB.24.16.7024-7031.2004
1158 58. Tani T, Orimo H, Shimizu A, Tsuruoka S. Development of a novel chronic kidney
1159 disease mouse model to evaluate the progression of hyperphosphatemia and associated
1160 mineral bone disease. *Sci Rep*. 2017;7:2233. doi: 10.1038/s41598-017-02351-6
1161 59. Feng J, Funk WD, Wang SS, Weinrich SL, Avilion AA, Chiu CP, Adams RR, Chang E,
1162 Allsopp RC, Yu J, et al. The RNA component of human telomerase. *Science*.
1163 1995;269:1236-1241. doi: 10.1126/science.7544491
1164 60. Roake CM, Artandi SE. Regulation of human telomerase in homeostasis and disease.
1165 *Nat Rev Mol Cell Biol*. 2020;21:384-397. doi: 10.1038/s41580-020-0234-z
1166 61. Pascolo E, Wenz C, Lingner J, Hauel N, Priepke H, Kauffmann I, Garin-Chesa P, Rettig
1167 WJ, Damm K, Schnapp A. Mechanism of human telomerase inhibition by BIBR1532, a
1168 synthetic, non-nucleosidic drug candidate. *J Biol Chem*. 2002;277:15566-15572. doi:
1169 10.1074/jbc.M201266200
1170 62. Ghosh A, Saginc G, Leow SC, Khattar E, Shin EM, Yan TD, Wong M, Zhang Z, Li G,
1171 Sung WK, et al. Telomerase directly regulates NF-kappaB-dependent transcription. *Nat*
1172 *Cell Biol*. 2012;14:1270-1281. doi: 10.1038/ncb2621
1173 63. Liu N, Ding D, Hao W, Yang F, Wu X, Wang M, Xu X, Ju Z, Liu JP, Song Z, et al. hTERT
1174 promotes tumor angiogenesis by activating VEGF via interactions with the Sp1
1175 transcription factor. *Nucleic Acids Res*. 2016;44:8693-8703. doi: 10.1093/nar/gkw549
1176 64. Lee C, Huang CH. LASAGNA: a novel algorithm for transcription factor binding site
1177 alignment. *BMC Bioinformatics*. 2013;14:108. doi: 10.1186/1471-2105-14-108
1178 65. Wingender E, Dietze P, Karas H, Knuppel R. TRANSFAC: a database on transcription
1179 factors and their DNA binding sites. *Nucleic Acids Res*. 1996;24:238-241. doi:
1180 10.1093/nar/24.1.238
1181 66. Babu AN, Meng X, Zou N, Yang X, Wang M, Song Y, Cleveland JC, Weyant M,
1182 Banerjee A, Fullerton DA. Lipopolysaccharide stimulation of human aortic valve
1183 interstitial cells activates inflammation and osteogenesis. *Ann Thorac Surg*. 2008;86:71-
1184 76. doi: 10.1016/j.athoracsur.2008.03.008
1185 67. Natarajan K, Muller-Klieser D, Rubner S, Berg T. Stafia-1: a STAT5a-Selective Inhibitor
1186 Developed via Docking-Based Screening of in Silico O-Phosphorylated Fragments.
1187 *Chemistry*. 2020;26:148-154. doi: 10.1002/chem.201904147

1188 68. Elumalai N, Berg A, Natarajan K, Scharow A, Berg T. Nanomolar inhibitors of the
1189 transcription factor STAT5b with high selectivity over STAT5a. *Angew Chem Int Ed Engl*.
1190 2015;54:4758-4763. doi: 10.1002/anie.201410672
1191 69. Fredriksson S, Gullberg M, Jarvius J, Olsson C, Pietras K, Gustafsdottir SM, Ostman A,
1192 Landegren U. Protein detection using proximity-dependent DNA ligation assays. *Nat*
1193 *Biotechnol*. 2002;20:473-477. doi: 10.1038/nbt0502-473
1194 70. Gillis AJ, Schuller AP, Skordalakes E. Structure of the Tribolium castaneum telomerase
1195 catalytic subunit TERT. *Nature*. 2008;455:633-637. doi: 10.1038/nature07283
1196 71. Neculai D, Neculai AM, Verrier S, Straub K, Klumpp K, Pfitzner E, Becker S. Structure of
1197 the unphosphorylated STAT5a dimer. *J Biol Chem*. 2005;280:40782-40787. doi:
1198 10.1074/jbc.M507682200
1199 72. Jumper J, Evans R, Pritzel A, Green T, Figurnov M, Ronneberger O, Tunyasuvunakool
1200 K, Bates R, Zidek A, Potapenko A, et al. Highly accurate protein structure prediction with
1201 AlphaFold. *Nature*. 2021;596:583-589. doi: 10.1038/s41586-021-03819-2
1202 73. Yan Y, Tao H, He J, Huang SY. The HDOCK server for integrated protein-protein
1203 docking. *Nat Protoc*. 2020;15:1829-1852. doi: 10.1038/s41596-020-0312-x
1204 74. Tebo AG, Gautier A. A split fluorescent reporter with rapid and reversible
1205 complementation. *Nat Commun*. 2019;10:2822. doi: 10.1038/s41467-019-10855-0
1206 75. Liu JC, Lengner CJ, Gaur T, Lou Y, Hussain S, Jones MD, Borodic B, Colby JL,
1207 Steinman HA, van Wijnen AJ, et al. Runx2 protein expression utilizes the Runx2 P1
1208 promoter to establish osteoprogenitor cell number for normal bone formation. *J Biol*
1209 *Chem*. 2011;286:30057-30070. doi: 10.1074/jbc.M111.241505
1210 76. Stock M, Otto F. Control of RUNX2 isoform expression: the role of promoters and
1211 enhancers. *J Cell Biochem*. 2005;95:506-517. doi: 10.1002/jcb.20471
1212 77. Zhang S, Xiao Z, Luo J, He N, Mahlios J, Quarles LD. Dose-dependent effects of Runx2
1213 on bone development. *J Bone Miner Res*. 2009;24:1889-1904. doi: 10.1359/jbmr.090502
1214 78. Okura H, Sato S, Kishikawa S, Kaneto S, Nakashima T, Yoshida N, Takayanagi H,
1215 Kiyono H. Runx2-I isoform contributes to fetal bone formation even in the absence of
1216 specific N-terminal amino acids. *PLoS One*. 2014;9:e108294. doi:
1217 10.1371/journal.pone.0108294
1218 79. Banerjee C, Javed A, Choi JY, Green J, Rosen V, van Wijnen AJ, Stein JL, Lian JB,
1219 Stein GS. Differential regulation of the two principal Runx2/Cbfa1 n-terminal isoforms in

1220 response to bone morphogenetic protein-2 during development of the osteoblast
1221 phenotype. *Endocrinology*. 2001;142:4026-4039. doi: 10.1210/endo.142.9.8367
1222 80. Maida Y, Yasukawa M, Okamoto N, Ohka S, Kinoshita K, Totoki Y, Ito TK, Minamino T,
1223 Nakamura H, Yamaguchi S, et al. Involvement of telomerase reverse transcriptase in
1224 heterochromatin maintenance. *Mol Cell Biol*. 2014;34:1576-1593. doi:
1225 10.1128/MCB.00093-14
1226 81. Okamoto N, Yasukawa M, Nguyen C, Kasim V, Maida Y, Possemato R, Shibata T, Ligon
1227 KL, Fukami K, Hahn WC, et al. Maintenance of tumor initiating cells of defined genetic
1228 composition by nucleostemin. *Proc Natl Acad Sci U S A*. 2011;108:20388-20393. doi:
1229 10.1073/pnas.1015171108
1230 82. Gizard F, Nomiyama T, Zhao Y, Findeisen HM, Heywood EB, Jones KL, Staels B,
1231 Bruemmer D. The PPARalpha/p16INK4a pathway inhibits vascular smooth muscle cell
1232 proliferation by repressing cell cycle-dependent telomerase activation. *Circ Res*.
1233 2008;103:1155-1163. doi: 10.1161/CIRCRESAHA.108.186205
1234 83. Yutzey KE, Demer LL, Body SC, Huggins GS, Towler DA, Giachelli CM, Hofmann-
1235 Bowman MA, Mortlock DP, Rogers MB, Sadeghi MM, et al. Calcific aortic valve disease:
1236 a consensus summary from the Alliance of Investigators on Calcific Aortic Valve
1237 Disease. *Arterioscler Thromb Vasc Biol*. 2014;34:2387-2393. doi:
1238 10.1161/ATVBAHA.114.302523
1239 84. Hoerstrup SP, Kadner A, Melnitchouk S, Trojan A, Eid K, Tracy J, Sodian R, Visjager JF,
1240 Kolb SA, Grunenfelder J, et al. Tissue engineering of functional trileaflet heart valves
1241 from human marrow stromal cells. *Circulation*. 2002;106:I143-150.
1242 85. Hortells L, Sur S, St Hilaire C. Cell Phenotype Transitions in Cardiovascular
1243 Calcification. *Front Cardiovasc Med*. 2018;5:27. doi: 10.3389/fcvm.2018.00027
1244 86. Bogdanova M, Zabirnyk A, Malashicheva A, Enayati KZ, Karlsen TA, Kaljusto ML,
1245 Kvitting JP, Dissen E, Sullivan GJ, Kostareva A, et al. Interstitial cells in calcified aortic
1246 valves have reduced differentiation potential and stem cell-like properties. *Sci Rep*.
1247 2019;9:12934. doi: 10.1038/s41598-019-49016-0
1248 87. Xu K, Xie S, Huang Y, Zhou T, Liu M, Zhu P, Wang C, Shi J, Li F, Sellke FW, et al. Cell-
1249 Type Transcriptome Atlas of Human Aortic Valves Reveal Cell Heterogeneity and
1250 Endothelial to Mesenchymal Transition Involved in Calcific Aortic Valve Disease.
1251 *Arterioscler Thromb Vasc Biol*. 2020;40:2910-2921. doi: 10.1161/ATVBAHA.120.314789

1252 88. Lindroos M, Kupari M, Heikkila J, Tilvis R. Prevalence of aortic valve abnormalities in the
1253 elderly: an echocardiographic study of a random population sample. *J Am Coll Cardiol*.
1254 1993;21:1220-1225. doi: 10.1016/0735-1097(93)90249-z
1255 89. Joung YH, Lim EJ, Darvin P, Chung SC, Jang JW, Do Park K, Lee HK, Kim HS, Park T,
1256 Yang YM. MSM enhances GH signaling via the Jak2/STAT5b pathway in osteoblast-like
1257 cells and osteoblast differentiation through the activation of STAT5b in MSCs. *PLoS*
1258 *One*. 2012;7:e47477. doi: 10.1371/journal.pone.0047477
1259 90. Lee KM, Park KH, Hwang JS, Lee M, Yoon DS, Ryu HA, Jung HS, Park KW, Kim J,
1260 Park SW, et al. Inhibition of STAT5A promotes osteogenesis by DLX5 regulation. *Cell*
1261 *Death Dis*. 2018;9:1136. doi: 10.1038/s41419-018-1184-7
1262 91. Paulson M, Pisharody S, Pan L, Guadagno S, Mui AL, Levy DE. Stat protein
1263 transactivation domains recruit p300/CBP through widely divergent sequences. *J Biol*
1264 *Chem*. 1999;274:25343-25349. doi: 10.1074/jbc.274.36.25343
1265 92. Martino A, Holmes JHt, Lord JD, Moon JJ, Nelson BH. Stat5 and Sp1 regulate
1266 transcription of the cyclin D2 gene in response to IL-2. *J Immunol*. 2001;166:1723-1729.
1267 doi: 10.4049/jimmunol.166.3.1723
1268 93. Bergad PL, Towle HC, Berry SA. Yin-yang 1 and glucocorticoid receptor participate in
1269 the Stat5-mediated growth hormone response of the serine protease inhibitor 2.1 gene.
1270 *J Biol Chem*. 2000;275:8114-8120. doi: 10.1074/jbc.275.11.8114
1271 94. Yamada O, Ozaki K, Furukawa T, Machida M, Wang YH, Motoji T, Mitsuishi T, Akiyama
1272 M, Yamada H, Kawauchi K, et al. Activation of STAT5 confers imatinib resistance on
1273 leukemic cells through the transcription of TERT and MDR1. *Cell Signal*. 2011;23:1119-
1274 1127. doi: 10.1016/j.cellsig.2011.02.005
1275 95. Yamada O, Ozaki K, Akiyama M, Kawauchi K. JAK-STAT and JAK-PI3K-mTORC1
1276 pathways regulate telomerase transcriptionally and posttranslationally in ATL cells. *Mol*
1277 *Cancer Ther*. 2012;11:1112-1121. doi: 10.1158/1535-7163.MCT-11-0850
1278 96. Tormo AJ, Letellier MC, Sharma M, Elson G, Crabe S, Gauchat JF. IL-6 activates
1279 STAT5 in T cells. *Cytokine*. 2012;60:575-582. doi: 10.1016/j.cyto.2012.07.002
1280 97. Tanabe Y, Nishibori T, Su L, Arduini RM, Baker DP, David M. Cutting edge: role of
1281 STAT1, STAT3, and STAT5 in IFN-alpha beta responses in T lymphocytes. *J Immunol*.
1282 2005;174:609-613. doi: 10.4049/jimmunol.174.2.609
1283 98. Honda S, Miyamoto T, Watanabe T, Narumi T, Kadowaki S, Honda Y, Otaki Y,
1284 Hasegawa H, Netsu S, Funayama A, et al. A novel mouse model of aortic valve stenosis

1285 induced by direct wire injury. *Arterioscler Thromb Vasc Biol*. 2014;34:270-278. doi:
1286 10.1161/ATVBAHA.113.302610
1287 99. Sider KL, Blaser MC, Simmons CA. Animal models of calcific aortic valve disease. *Int J*
1288 *Inflam*. 2011;2011:364310. doi: 10.4061/2011/364310
1289 100. Balani K, Brito FC, Kos L, Agarwal A. Melanocyte pigmentation stiffens murine cardiac
1290 tricuspid valve leaflet. *J R Soc Interface*. 2009;6:1097-1102. doi: 10.1098/rsif.2009.0174
1291 101. Carneiro F, Kruithof BP, Balani K, Agarwal A, Gaussin V, Kos L. Relationships between
1292 melanocytes, mechanical properties and extracellular matrix composition in mouse heart
1293 valves. *J Long Term Eff Med Implants*. 2015;25:17-26. doi:
1294 10.1615/jlongtermeffmedimplants.2015011748
1295 102. Mjaatvedt CH, Kern CB, Norris RA, Fairey S, Cave CL. Normal distribution of
1296 melanocytes in the mouse heart. *Anat Rec A Discov Mol Cell Evol Biol*. 2005;285:748-
1297 757. doi: 10.1002/ar.a.20210
1298 103. Dharmarajan S, Speer MY, Pierce K, Lally J, Leaf EM, Lin ME, Scatena M, Giachelli CM.
1299 Role of Runx2 in Calcific Aortic Valve Disease in Mouse Models. *Front Cardiovasc Med*.
1300 2021;8:687210. doi: 10.3389/fcvm.2021.687210
1301 104. Lanzer P, Hannan FM, Lanzer JD, Janzen J, Raggi P, Furniss D, Schuchardt M,
1302 Thakker R, Fok PW, Saez-Rodriguez J, et al. Medial Arterial Calcification: JACC State-
1303 of-the-Art Review. *J Am Coll Cardiol*. 2021;78:1145-1165. doi:
1304 10.1016/j.jacc.2021.06.049
1305

Non-canonical Telomerase Reverse Transcriptase Controls Osteogenic Reprogramming of Aortic Valve Cells Through STAT5

Rolando A. Cuevas[1], Luis Hortells[2], Claire C. Chu[1], Ryan Wong[1], Alex Crane[1], Camille Boufford[1], Cailyn Regan[1], William J. Moorhead III[1], Michael J. Bashline[1], Aneesha Parwal[1], Angelina M. Parise[1], Parya Behzadi[1], Mark J. Brown[1], Aditi Gurkar[3], Dennis Bruemmer[4], John Sembrat[5], Ibrahim Sultan[6], Thomas G. Gleason[6], Marie Billaud[6], and Cynthia St. Hilaire[1,8,9*]

[1] Division of Cardiology, Department of Medicine, Pittsburgh Heart, Lung, Blood and Vascular Medicine Institute, University of Pittsburgh, Pittsburgh, Pennsylvania, USA.

[2] Cardiovascular Research Group, Department of Medical Biology, Faculty of Health Science, UiT-The Arctic University of Norway, 9019 Tromsø, Norway.

[3] Aging Institute, Division of Geriatrics, Department of Medicine, University of Pittsburgh, Pittsburgh, Pennsylvania, USA.

[4] Department of Cardiovascular Medicine, Cleveland Clinic, Cleveland, OH, USA.

[5] Division of Pulmonary, Allergy, and Critical Care Medicine, University of Pittsburgh School of Medicine, Pittsburgh, PA, USA.

[6] Division of Cardiac Surgery, Department of Cardiothoracic Surgery, Heart and Vascular Institute, University of Pittsburgh Medical Center, Pittsburgh, Pennsylvania, USA.

[7] Department of Surgery, Division of Cardiac Surgery, Brigham and Women's Hospital & Harvard Medical School, Boston, Maryland, USA.

[8] Department of Bioengineering, University of Pittsburgh, Pittsburgh, Pennsylvania, USA.

[9] Department of Cardiothoracic Surgery, University of Pittsburgh, Pittsburgh, Pennsylvania, USA

Running Title: TERT/STAT5 is required for valvular calcification

*Corresponding Author Contact Info:
Cynthia St. Hilaire, PhD, FAHA
University of Pittsburgh
BSTWR 1744.1
200 Lothrop Street, Pittsburgh, PA 15261
+1 412-648-9441 sthilair@pitt.edu

TOTAL WORD COUNT: 7285
ABSTRACT WORD COUNT: 302

Background: Calcific aortic valve disease (CAVD) is the pathological remodeling of valve leaflets. The initial steps in valve leaflet osteogenic reprogramming are not fully understood. As telomerase reverse transcriptase (TERT) overexpression primes mesenchymal stem cells to differentiate into osteoblasts, we investigated whether TERT contributes to the osteogenic reprogramming of valve interstitial cells (VICs).
Methods: Human control and CAVD aortic valve leaflets and patient-specific hVICs were used in in vivo and in vitro calcification assays. Loss of function experiments in hVICs and cells isolated from *Tert*$^{-/-}$ and *Terc*$^{-/-}$ mice were used for mechanistic studies. Calcification was assessed in *Tert*$^{+/+}$ and *Tert*$^{-/-}$ mice ex vivo and in vivo. In silico modeling, proximity ligation and co-immunoprecipitation assays defined novel TERT interacting partners. Chromatin immunoprecipitation and CUT&TAG sequencing defined protein-DNA interactions.
Results: TERT protein was highly expressed in calcified valve leaflets without changes in telomere length, DNA damage, or senescence markers, and these features were retained in isolated primary hVICs. *TERT* expression increased with osteogenic or inflammatory stimuli,

and knock-down or genetic deletion of *TERT* prevented calcification in vitro and in vivo. Mechanistically, TERT was upregulated via NF-κB and required to initiate osteogenic reprogramming, independent of its canonical reverse transcriptase activity and the lncRNA *TERC*. TERT exerts non-canonical osteogenic functions via binding with Signal Transducer and Activator of Transcription 5 (STAT5). Depletion or inhibition of STAT5 prevented calcification. STAT5 was found to bind the promoter region of Runt-Related Transcription Factor 2 (*RUNX2*), the master regulator of osteogenic reprogramming. Lastly, we demonstrate that TERT and STAT5 are upregulated and colocalized in CAVD tissue compared to control tissue.

Conclusions: TERT's non-canonical activity is required to initiate calcification. TERT is upregulated via inflammatory signaling pathways and partners with STAT5 to bind the *RUNX2* gene promoter. These data identify a novel mechanism and potential therapeutic target to decrease vascular calcification.

ABBREVIATIONS:

CAVD, calcific aortic valve disease; CNN, calponin; CUT&Run, cleavage under targets & release using nuclease; CUT&Tag, cleavage under targets & tagmentation; CFAST, fluorescence-activating and absorption-shifting tag, C-domain; Ch-IP, chromatin immunoprecipitation; E2F1, E2F transcription factor 1; ECM, extracellular matrix; GO, gene ontology; γ-H2AX, phosphorylated gamma histone 2AX; hCASMCs, human coronary smooth muscle cells; hVICs, human aortic valve interstitial cells; IP, immunoprecipitation; lncRNA, long non-coding RNA; LPS, lipopolysaccharide; BMMSCs, bone marrow mesenchymal stem cells; MSCs, mesenchymal stem cells; NFAST, fluorescence-activating and absorption-shifting tag, N-domain; NT, no treatment; mVICs, mouse aortic valve interstitial cells OPN, osteopontin; OST, osteogenic treatment; PCNA, proliferating cell nuclear antigen; PLA, proximity ligation assay ; RUNX2, runt-related transcription factor 2; αSMA, alpha 2 smooth muscle actin; SMARCA4,

76 SWI/SNF chromatin remodeling complex A4; STAT5, signal transducer and activator of
77 transcription 5A/B; *lncTERC*, telomerase RNA component; TERT, telomerase reverse
78 transcriptase; TL, telomere length; TNAP, Tissue-Nonspecific Alkaline Phosphatase; TSS,
79 transcription start site, αTUB, alpha-tubulin
80

81 **Key Words:**
82 calcific aortic valve disease, vascular calcification, osteogenic reprogramming, TERT, STAT5
83

84 **Novelty and Significance**

85 *What is known?*

86 • Calcific aortic valve disease (CAVD) is the most prevalent form of aortic valve pathology.
87 CAVD strongly correlates with age and leads to heart failure and a high risk of stroke.
88 Currently, the only therapeutic option is valve replacement, which comes with significant
89 healthcare costs and additional risks to patients.
90 • Runt-related transcription factor 2 (RUNX2) is the master transcription factor required for
91 osteogenic differentiation of stem cells to osteoblasts and osteogenic reprogramming of
92 cardiovascular cells. Yet, the early events driving its activity in aortic valve cells are poorly
93 defined.
94 • In addition to its reverse transcriptase enzymatic activity, TERT exhibits non-canonical
95 transcriptional regulatory functions and overexpression of TERT primes mesenchymal stem
96 cells to differentiate down the osteoblast lineage.
97

98 *What new information does this article contribute?*

99 • TERT protein levels in calcified aortic leaflets and valve interstitial cells, and its non-
100 canonical osteogenic activity are independent of changes in telomere length and cell
101 senescence.
102 • Genetic loss or depletion of TERT prevented calcification in valve interstitial cells, coronary
103 smooth muscle cells, and mesenchymal stem cells in vitro and the vasculature in vivo.
104 • Early in the osteogenic reprogramming inflammatory signaling promotes TERT to co-localize
105 with SMARCA4 and STAT5, and this TERT-tethered STAT5 binds to the *RUNX2* gene
106 promoter, the master regulator of osteogenic transcriptional programs.
107 • STAT5 depletion and pharmacological inhibition prevent calcification of human valve
108 interstitial cells, coronary smooth muscle cells, and mesenchymal stem cells.
109
110 *What are the clinical implications?*
111 • We have identified TERT-STAT5 as a novel signaling axis that orchestrates the early steps
112 in the osteogenic reprogramming of aortic valve cells. Inhibiting TERT/STAT5 interaction or
113 their activity may be leveraged for the development of therapeutic strategies to halt or
114 prevent calcification in the aortic valve, bioprosthetic valves, and or perhaps other
115 cardiovascular tissues.
116 • Invasive and expensive surgical procedures are currently the only treatment option for
117 patients with CAVD. The discovery and defining of the early events driving vascular
118 calcification identifies novel and druggable targets for developing non-surgical therapies.
119

120 **INTRODUCTION**

121 Calcific aortic valve disease (CAVD) encompasses a spectrum of pathological remodeling of the
122 valve leaflet, ranging from mild valve thickening that displays microcalcifications to
123 macrocalcifications that predominate in more advanced disease stages.[1,2] The advanced state,
124 aortic stenosis, results from fibrotic remodeling and the formation of calcified nodules on the
125 valve leaflet that impede and disrupt blood flow, causing excessive strain on the cardiac tissue,
126 increasing the risk of stroke and leading to heart failure.[3] CAVD severity and incidence increase
127 with age, with CAVD prevalence >1,000 per 100,000 individuals ≥75 years of age.[4,5] Further,
128 roughly 0.4-0.6% of the population harbors bicuspid aortic valve malformations, and these
129 malformed valves are prone to calcify and develop CAVD.[4] Currently, no therapeutic treatment
130 halts or reverses pathologic calcification that occurs in the aortic valve leaflets or other
131 cardiovascular tissues. The only therapeutic option to treat aortic stenosis is valve replacement
132 via surgical or transcatheter procedures, incurring substantial medical costs and health care
133 burdens to the patient.[6]
134
135 Aortic valve interstitial cells (VICs) are the primary cell type within the valve leaflet and are
136 responsible for maintaining leaflet integrity. VICs reside in a quiescent state; however, adaptive
137 or maladaptive responses to environmental factors such as inflammation, extracellular matrix
138 (ECM) breakdown, and mechanical stress may disrupt VIC homeostasis.[7,8] With alterations in
139 homeostasis, VICs acquire a myofibroblast-like phenotype, termed “activated VICs,” capable of
140 proliferation, contraction, and secretion of proteins that further remodel the extracellular milieu.[9]
141 Activated VICs can transition into calcifying cells; however, the initial steps regulating this
142 process are not fully understood. It is well established that the osteogenic reprogramming of
143 cardiovascular cells such as VICs and vascular smooth muscle cells (SMCs) is analogous to the

144 differentiation of mesenchymal stem cells (MSCs) into bone-forming osteoblasts; osteogenic
145 differentiation of MSCs and the reprogramming of cardiovascular cells is primarily orchestrated
146 by Runt-related transcription factor 2 (*RUNX2*), the master regulator of osteogenic
147 transcriptional programs.[10-12] Other osteogenic signature markers, such as osteocalcin, alkaline
148 phosphatase, and osteopontin, are upregulated in the differentiation of stem cells to osteoblasts
149 and the calcifying of VICs.[9,13] While it is accepted that VICs upregulate the expression of
150 osteogenic genes in response to stresses such as inflammation, ECM remodeling, and
151 mechanical stress, the specific mechanistic steps between those stresses and the initial
152 reprogramming events in the activation of osteogenic transcriptional reprogramming remain ill-
153 defined.
154
155 The telomerase complex extends and maintains the ends of chromosomes after cell division.
156 The core complex consists of the telomerase long non-coding RNA component (*lncTERC*) and
157 telomerase reverse transcriptase (TERT) protein, along with other scaffolding proteins.[14] In
158 addition to reverse transcriptase activity, TERT also exhibits non-canonical functions
159 independent of telomere extension, such as regulating gene expression and orchestrating
160 chromatin remodeling.[15-17] For example, TERT acts as a cofactor in Wnt-dependent promoter
161 activation by interacting with the chromatin remodeling protein SWI/SNF related, matrix
162 associated, actin dependent regulator of chromatin, subfamily a, member 4 (SMARCA4),
163 facilitating the expression of Wnt/β-catenin target genes in stem cells.[18] In a murine model of
164 atherosclerosis, TERT induced chromatin remodeling and SMC proliferation by chaperoning the
165 retinoblastoma-associated transcription factor 1 (E2F1) binding to S-phase gene promoters.[19,20]
166 Linking together the themes of calcification and non-canonical TERT, two co-published studies
167 identified that the overexpression of *TERT* primed human MSCs to differentiate down the
168 osteogenic lineage and develop bone-like structures.[21,22] The mechanism by which TERT drives

169 the osteogenic differentiation of human MSCs is unknown. Collectively, these studies provide
170 strong evidence of telomerase-independent functions of TERT in altering chromatin states and
171 regulating gene expression via various protein-protein interactions.
172
173 Although telomere length is recognized as a biomarker of aging, it can vary significantly among
174 individuals of the same age, including twins.[23] Studies have examined the association between
175 shortened telomeres in circulating leukocytes and various vascular conditions, with mixed
176 results.[24-26] One study compared telomere lengths in leukocytes of control patients and those
177 with atherosclerotic plaques, as well as the atherosclerotic plaques themselves and found that
178 while atherosclerotic patients' leukocytes had shorter telomeres than controls, their plaque cells
179 exhibited longer telomeres than both groups' leukocytes, suggesting heightened telomerase
180 activity in the diseased tissue.[27-29] Thus, whether leukocyte telomere length can be used as a
181 biomarker remains speculative. A notable aspect of these prior studies is the lack of TERT
182 protein assessment or a focused investigation of telomere length in disease tissues.
183
184 Signal transducers and activators of transcription (STAT) proteins play essential roles in
185 inflammatory, proliferative, and apoptotic programs, mediating the signal transduction pathways
186 of various cytokines and growth factors.[30] STAT proteins function as transcription factors and
187 recruit chromatin remodeling and histone-modifying proteins to upregulate gene transcription.[31]
188 STAT5A and STAT5B are encoded by two highly conserved genes in humans and mice; 96% of
189 their amino acid sequence is shared, and many of their activities are redundant.[32] Herein,
190 unless specific tools are utilized to allow a distinction, we will generally refer to both as STAT5.
191 Upon phosphorylation, STAT5 dimerizes and translocates into the nucleus to bind the
192 consensus motif (TTCNNNGAA) and activates the promoters of various target genes by

193 recruiting transcriptional co-activators.[33,34] Crucially, studies have shown that several osteogenic
194 genes depend on STAT5 to promote chondrocyte and osteoblast differentiation.[35,36]
195
196 In this study, we tested the hypothesis that TERT contributes to the osteogenic reprogramming
197 of VICs. We utilized primary human aortic valve tissues from control donors and CAVD patients
198 and generated patient-specific VIC lines for in vitro disease modeling. We established baseline
199 patterns and osteogenic induction of *TERT* and calcification markers in CAVD tissue and VICs.
200 We assessed the consequences of genetic deletion or depletion of *TERT* during osteogenic
201 reprogramming in several cell types and in in vivo and ex vivo calcification models. We further
202 defined the underlying mechanism by which TERT and STAT5 participate in the osteogenic
203 reprogramming of VICs.
204

205 **METHODS**

206 **Data Availability**

207 The Materials, Methods, and Major Resources Table are found in the Supplemental Material.
208 The raw data, experimental materials, and analytic methods are available from the
209 corresponding author upon reasonable request.
210

211 **RESULTS**

212 **TERT is elevated in CAVD tissues.**

213 Human aortic valves were collected after surgical aortic valve replacement procedures or from
214 cadaveric tissue obtained via the Center for Organ Recovery and Education (CORE) of the
215 University of Pittsburgh Medical Center and processed as previously described.[37] Macroscopic
216 examination and histological staining with Von Kossa were used to determine and confirm

217 whether valves could be classified as a non-calcified control or as having calcific aortic valve
218 disease (CAVD) (**Figure 1A, Supplemental Figure 1A, Supplemental Table 1**). RUNX2 is the
219 master transcription factor required to initiate stem cells to differentiate into osteoblasts and is
220 critical for the pathological osteogenic reprogramming of vascular cells.[38-41] Immunofluorescent
221 staining showed RUNX2, and the late calcification marker osteopontin (OPN) were significantly
222 upregulated in CAVD tissue compared to control tissues, indicating activation of osteogenic
223 transcriptional programs in CAVD tissues (**Supplemental Figure 1B**). Previous studies found
224 that overexpression of TERT primes human MSCs to differentiate down the osteogenic
225 lineage.[21,22] We found that *TERT* transcript levels were significantly upregulated in CAVD tissue
226 relative to control samples (**Figure 1B**), and *TERT* expression levels showed no correlation with
227 the donor's age (**Supplemental Figure 1C**). Markers of senescence (cyclin-dependent kinase
228 inhibitor 1A, *CDKN1A*, galactosidase beta 1, *GLB1*), proliferation (proliferating cell nuclear
229 antigen, *PCNA*), DNA damage (tumor protein 53, *TP53*), and cytoskeletal markers (actin alpha
230 2 smooth muscle, *ACTA2*, vimentin, *VIM,* interleukin 6, *IL6*) showed no statistically significant
231 differences, while the inflammatory marker and tumor necrosis factor-alpha (*TNF)* was
232 significantly elevated in CAVD samples (**Supplemental Figure 1D**), supporting observations by
233 others that indicate a role for inflammatory signaling in aortic valve calcification
234 pathogenesis.[42,43]
235
236 We detected elevated TERT protein signal in CAVD valves compared to non-calcified controls,
237 with the signal localized to areas of calcification. Similarly, the number of cells expressing TERT
238 was significantly elevated in our CAVD tissues compared to non-calcified control tissues
239 (**Figure 1C**). No statistically significant differences were observed in the staining levels of
240 proliferation marker PCNA or the DNA damage indicator phosphorylated gamma histone 2AX
241 (γ-H2AX) between CAVD and control tissues (**Supplemental Figure 1E**). We also found no

242 statistically significant differences in the relative mean telomere length between the control and
243 CAVD tissues in our study (**Figure 1D**), indicating no overt influence of the canonical telomere-
244 extending functions of TERT. The mean age of CAVD patients in this study was slightly
245 elevated compared to the control patients, 68 and 54 years old, respectively (**Figure 1E**).
246 Together, these data show that TERT, osteogenic markers, and inflammatory signatures are
247 upregulated in CAVD tissues compared to controls, while markers indicating alterations in
248 proliferation, DNA damage, and senescence are not altered, suggesting that the non-canonical
249 activity of TERT is operative.
250

251 **CAVD human VICs at baseline recapitulate observations in CAVD tissues.**

252 We created patient-specific valve interstitial cell (VIC) lines from CAVD and control valves.[37] At
253 baseline, freshly isolated hVICs from CAVD and control patients exhibited no morphological or
254 statistical differences in their proliferative or migratory capacity (**Figure 2, A- C, and**
255 **Supplemental Figure 1F**). TERT and RUNX2 proteins were significantly elevated at baseline in
256 CAVD hVICs compared to control hVICs (**Figure 2D**). We observed no statistical differences in
257 the protein levels of the hVIC activation markers SM22 or αSMA between CAVD and control
258 hVICs, but observed a significant increase of the mineralizing enzyme tissue non-specific
259 alkaline phosphatase (TNAP) in CAVD hVICs at baseline (**Supplemental 1G**). As in the leaflets,
260 there was no statistical difference in the relative telomere length between CAVD and control
261 hVICs (**Figure 2E**). These data show that hVICs isolated from CAVD patients display gene
262 expression and protein signatures that recapitulate the osteogenic phenotype observed in
263 CAVD leaflet tissue.
264

265 **TERT expression is upregulated in human VICs in an in vitro osteogenic disease model.**

266 To model CAVD in vitro and investigate a role for TERT during hVIC osteogenic
267 reprogramming, we cultured CAVD and control hVICs in osteogenic media conditions (OST), a
268 media widely utilized to induce osteogenic differentiation of stem cells to osteoblasts.[44] Alizarin
269 Red staining for calcification revealed that both OST-treated CAVD and control hVICs lay down
270 calcified matrix as early as 14 days (d14), CAVD hVICs calcified earlier relative to control hVICs
271 (**Figure 2F**). Importantly, we observed that CAVD hVICs calcify de novo under no treatment
272 (NT) conditions, suggesting that CAVD hVICs are primed for osteogenic reprogramming (**Figure**
273 **2F**). The calcification markers RUNX2 and OPN were significantly upregulated in both control
274 and CAVD hVICs at d14 OST, indicating active osteogenic reprogramming (**Figure 2G**). TERT
275 protein levels were also significantly increased in control and CAVD hVICs after d14 of OST
276 (**Figure 2G**). TERT protein signal can be seen in CAVD hVICs at d14 under NT conditions
277 (**Figure 2H**, left panels). At d14 of OST, the TERT protein staining was elevated and localized
278 near areas of calcification in both control and CAVD hVICs; however, CAVD hVICs formed
279 larger calcified nodules (**Figure 2H**, right panels). We observed no significant differences in cell
280 numbers at the end of the d14 assay under NT or OST treatment conditions (**Supplemental**
281 **Figure 2A**). As we observed that CAVD hVICs exhibit elevated osteogenic markers at baseline
282 (**Supplemental Figure 1G**) and are prone to calcify (**Figure 2H**) de novo, we assessed
283 transcriptional differences between control hVICs under NT or OST. Osteogenic markers *BMP2*,
284 *THBS1*, *ALPL,* and myofibroblast markers *CNN1*, *TAGLN*, and *SMTN* were significantly
285 upregulated in control hVICs at d14 of OST treatment (**Figure 2I**). Likewise, the calcification-
286 associated gene *FOXO1* and the CAVD-associated metalloproteinase *MMP13* were also
287 significantly upregulated in OST conditions.[45,46] Lastly, the pro-inflammatory transcription factor
288 signal transducer and activator of transcription 5A *(STAT5A)* was significantly upregulated,
289 while the expression of the isoform *STAT5B* remained unchanged. These results show that
290 hVICs are undergoing osteogenic reprogramming and not de novo mineral nucleation.[47]

291

292 In cancer and stem cells, elevated expression of TERT is associated with long telomeres and
293 enables unlimited proliferation, while short telomeres can trigger cellular senescence.[48,49]
294 Although we observed no differences in telomere length in our tissues and cells in this study
295 (Figures 1D and 2E), we assessed cellular senescence and observed no significant differences
296 in the expression of senescence-associated β-galactosidase (SA-β-gal, *GLB1*) between CAVD
297 and control hVICs at baseline **(Supplemental Figure 2B)** nor increased in control hVICs in OST
298 treatment (**Figure 2I**). SA-β-gal activity staining indicated that cellular senescence was not
299 engaged even after 28 days of OST treatment (**Supplemental Figure 2C**). These data
300 confirmed that cellular senescence is not operative during hVICs osteogenic reprogramming.
301

302 NF-κB is a transcription factor complex that acts downstream of inflammatory signals to mediate
303 inflammatory responses, and the c-Myc transcription factor mediates cell proliferation and
304 differentiation. Others have shown that both NF-κB and c-Myc can upregulate transcription of
305 the *TERT* gene.[50-52] We found that inhibiting NF-κB with BAY-107082, an irreversible inhibitor
306 that blocks the phosphorylation of IκB-α,[53,54] inhibited *TERT* expression during the osteogenic
307 reprogramming of hVICs. We also observed downregulation of *RUNX2* expression, consistent
308 with upstream TERT's regulatory role on *RUNX2* expression (**Supplemental Figure 2D**).
309 Likewise, we found that inhibiting c-MYC with 10058-F4 inhibited *TERT* expression during the
310 osteogenic differentiation of hVICs (**Supplemental Figure 2E**), validating previous research
311 showing that c-MYC regulates *TERT* gene expression.[16] These results further support that
312 inflammatory signaling contributes to the development of CAVD.
313

314 **TERT is required for the osteogenic differentiation of human MSCs.**

315 Previous studies have shown that the overexpression of TERT primes human mesenchymal
316 stem cells (hMSCs) to differentiate into osteoblasts.[21,22] To assess the role of endogenous
317 TERT in osteogenic differentiation, we subjected hMSCs to NT and OST treatment. OST
318 treatment induced robust calcification as early as d14, while cells in NT conditions did not calcify
319 (**Supplemental Figure 3A**). Protein analysis showed that the TERT protein levels significantly
320 increased on day 3 of the OST treatment, coinciding with increased *RUNX2* expression and
321 RUNX2 protein levels (**Supplemental Figures 3B and 3C**). hMSCs in OST treatment exhibited
322 intense TERT staining, and TERT-positive cells clustered around calcified nodules
323 (**Supplemental Figure 3D**). Using lentiviral-mediated transduction of expressing short-hairpin
324 RNA to deplete TERT (shTERT) or scrambled control (shControl), we found that knockdown of
325 *TERT* significantly inhibited the calcification of hMSCs (**Supplemental Figures 3E and 3F**).
326 While previous studies show that overexpression of *TERT* primed hMSCs to undergo
327 osteogenic differentiation, our data show that TERT is required for the osteogenic differentiation
328 of hMSCs.[21,22]
329
330 **TERT is required for calcification in vitro and in vivo.**
331 Control hVICs were transduced with shControl and shTERT lentivirus, and like hMSCs,
332 knockdown of *TERT* significantly inhibited calcification compared to the control group and
333 downregulated RUNX2 protein levels (**Figures 3A and 3B**). We assessed TERT's role in
334 calcifying human coronary artery smooth muscle cells (hCASMCs), which calcify in
335 atherosclerotic plaques.[55] Knocking down TERT significantly inhibited hCASMCs calcification
336 (**Figure 3C**). Together, these data indicate that TERT is essential for the osteogenic
337 reprogramming of hVICs and hCASMCs. Next, mice VIC (mVICs) and bone marrow MSCs
338 (mBMMSCs) lines were generated from *Tert*$^{+/+}$ and *Tert*$^{-/-}$ mice.[56] In line with our observations in
339 human cells with depleted TERT, we observed significant inhibition of calcification in *Tert*$^{-/-}$

340 mVICs (**Figure 3D**) and *Tert*$^{-/-}$ mBMMSCs (**Supplemental Figure 4A**) compared to *Tert*$^{+/+}$ cells.
341 No statistically significant differences were observed in senescence-associated β-galactosidase
342 activity in mVICs or mBMMSCs (**Supplemental Figures 4B** and **4C**).
343
344 To determine whether TERT is required to initiate and/or maintain osteogenic reprogramming,
345 we cultured control hVICs in OST and transduced shTERT lentivirus on d7 or d14, and
346 calcification was assessed on d21. Control hVICs transduced with shTERT on day 7 showed a
347 significant reduction in calcification compared to the OST alone, while transduction of shTERT
348 on day 14 did not show any decrease in calcification (**Supplemental Figure 4D**), indicating that
349 TERT is required to initiate, not maintain, reprogramming to the osteogenic phenotype.
350
351 Next, we used *Tert*$^{+/+}$ and *Tert*$^{-/-}$ mice strains to test whether TERT is required for diet-induced
352 non-atherosclerotic medial arterial calcification in vivo in mice. Of note, *Tert*$^{-/-}$ mice were
353 generated from heterozygous breeding pairs (F1 generation) and thus did not exhibit shortened
354 telomeres.[57] *Tert*$^{+/+}$ and *Tert*$^{-/-}$ mice were fed an adenine-phosphate (A6P6) diet, which was
355 previously shown to induce medial arterial calcification in the vasculature of mice.[58] At the end
356 of the 12-week regime, we observed significantly higher levels of calcification in the aorta of
357 *Tert*$^{+/+}$ compared to *Tert*$^{-/-}$ mice (**Figure 3E**). Staining for Runx2 protein mirrored calcification
358 presentation and was significantly higher in the *Tert*$^{+/+}$ compared to *Tert*$^{-/-}$ tissue (**Figure 3F**).
359 These findings were validated in an ex vivo calcification assay. Thoracic aortic rings obtained
360 from the *Tert*$^{+/+}$ and *Tert*$^{-/-}$ mice were cultured in ex vivo OST or control NT medium. *Tert*$^{+/+}$
361 aortic rings exhibited significantly elevated calcification compared to aortic rings from *Tert*$^{-/-}$ mice
362 on d14 (**Supplemental Figure 4E**). *Tert*$^{+/+}$ aortic rings also exhibited prominent staining for
363 Runx2 protein, which was absent in aortic rings from *Tert*$^{-/-}$ mice (**Supplemental Figure 4F**),
364 and western blot analysis confirmed elevated Runx2 protein levels in *Tert*$^{+/+}$ aortic rings

365 compared to *Tert*$^{-/-}$ (**Supplemental Figure 4G**). Neither calcification nor Runx2 was detected in
366 the NT groups. Together, these data show that TERT is required for osteogenic reprogramming
367 of cells in vitro and in vivo.
368
369 TERT's canonical telomere-extending activity requires the telomerase long non-coding RNA
370 component (*lncTerc*) to maintain chromosome telomere length and genome integrity.[14,59] *LncTerc*
371 exerts a dual function in the telomerase complex; it guides the telomerase complex to the telomere
372 ends and is the primer for TERT reverse transcriptase activity, and it serves as a scaffold for
373 tethering additional proteins to the telomerase complex (i.e., Dyskerin, NOP10, GAR1, and
374 NHP2).[60] To evaluate that TERT's role in calcification is independent of its canonical telomere-
375 extending function, we isolated mVICs from *Terc*$^{-/-}$ mice. While *Tert*$^{-/-}$ mVICs did not calcify under
376 OST conditions, *Terc*$^{-/-}$ mVICs were significantly calcified (**Figure 3G**). Similarly, in hVICs,
377 BIBR1532, which blocks the reverse transcriptase activity of TERT,[61] did not prevent calcification
378 nor decrease the expression of *RUNX2* (**Supplemental Figure 4H and 4I**). Together, these data
379 illustrate that the canonical telomere-extending function of TERT does not contribute to
380 osteogenic reprogramming.
381
382 **TERT/STAT5 interact and bind to the *RUNX2* gene promoter to initiate osteogenic**
383 **reprogramming.**
384 Several studies have shown that TERT participates in gene transcription by physically
385 interacting with transcription factors.[17,20,62,63] RUNX2 is the master regulator of osteogenic
386 differentiation of stem cells.[38,39] Increased *RUNX2* expression and transcriptional activity are the
387 hallmarks of osteoblast differentiation and cardiovascular calcification and are required for
388 osteogenic reprogramming of vascular cells.[40,41] As our data show that RUNX2 is significantly
389 downregulated in *TERT*-knockdown and deficient cells (Figure 3), we used the LASAGNA[64] and

390 TRANSFAC/MATCH[65] programs to identify putative transcription factor binding sites in the 5 kb
391 region upstream of the human *RUNX2* gene promoter (NM_001015051.3) and identified eight
392 potential STAT5 binding sites (**Supplemental Table 2**). We sought to determine whether
393 STAT5 is bound to the *RUNX2* gene promoter and focused on the two most proximal predicted
394 STAT5 sites located at -1371 bp and -193 bp upstream of the transcriptional start site (TSS), as
395 both have high homology to the tetrameric consensus STAT5 binding site and show an elevated
396 likelihood of being functional sites (**Figures 4A** and **4B**). As inflammation and inflammatory
397 signaling pathways are known to contribute to CAVD pathogenesis[1,66], and *TERT* expression
398 was induced via that inflammatory transcription factor NF-κB (Supplemental Figure 2D), we
399 used bacterial lipopolysaccharide (LPS) as a broad method to activate inflammatory response
400 pathways in hVICs. We found that LPS was sufficient to induce calcification of hVICs and that
401 TERT-positive cells accumulated near calcified nodules (**Figure 4C**). Protein analysis showed
402 that OST and LPS significantly upregulate TERT, RUNX2, and STAT5 proteins (**Figure 4D**).
403 TERT protein levels were elevated in both the cytosol and nucleus of cells upon OST
404 stimulation (**Supplemental Figure 5A**). Under NT conditions, STAT5 is observed in the
405 membrane and cytosol but translocates and accumulates in the nucleus of hVICs in OST
406 (**Supplemental Figure 5B**). Next, we used genetic and pharmacological approaches to
407 determine the requirement of STAT5 for the calcification of hVICs. The small molecules StafiA-1
408 and StafiB-1 specifically inhibit STAT5A and STAT5B, respectively.[67,68] We found that StafiA-1
409 significantly inhibited the calcification of control hVICs during a 21-day OST assay and that this
410 inhibition was greater than the inhibition observed with StafiB-1 (**Figure 4E**). In line with these
411 findings, we also observed that inhibition of STAT5A significantly reduced the expression of
412 *RUNX2* at d7 of osteogenic differentiation of hVICs, suggesting that STAT5A is a main
413 participant during the osteogenic reprogramming of hVICs (**Figure 4F**). Similarly, StafiA-1
414 significantly reduced calcification in hCASMCs and hMSCs (**Supplemental Figures 5C** and

415 **5D**). Lentiviral-mediated delivery of shControl or shSTAT5 constructs showed that depletion of
416 STAT5 significantly attenuated calcification and *RUNX2* expression (**Figure 4G and 4H**),
417 confirming an essential role for STAT5 in the osteogenic reprogramming of hVICs. Similar to
418 TERT (Supplemental Figure 4D), knocking down STAT5 after 7 or 14 days of OST treatment did
419 not reduce calcification (**Figure 4I**), indicating that STAT5 activity is required during the initial
420 steps of osteogenic reprogramming. Others have established that TERT can interact with
421 transcription factors to regulate gene expression.[17,20,62,63] We assessed whether TERT and
422 STAT5 directly interact. Three methods were utilized: proximity ligation assay (PLA), co-
423 immunoprecipitation (IP), and exogenously expressing TERT and STAT5 reporters. PLA can
424 detect protein-protein proximity <40 nm apart.[69] PLA revealed that OST significantly increased
425 TERT and STAT5 colocalization in control hVICs after 21 days of OST treatment relative to NT
426 condition (**Figure 4J**). Focusing on nuclear co-localization, TERT/STAT5 puncta are
427 significantly elevated in the nucleus of calcifying hVICs relative to the NT condition
428 (**Supplementary Figure 5E**). Protein IP shows that TERT and STAT5 physically interact in
429 hVICs upon OST treatment relative to NT condition (**Figure 4K**). A Dual-Luciferase reporter
430 assay shows that the human *RUNX2* promoter, containing the -194 and -1371 putative STAT5
431 binding sites, is upregulated early (d3) under OST treatment relative to NT, and that this
432 upregulation is abrogated with pharmacological inhibition of STAT5A, validating the functionality
433 of the predicted STAT5 binding in the *RUNX2* promoter (**Supplementary Figure 5F**).
434 Furthermore, an electrophoretic mobility shift assay (EMSA) confirmed the physical binding of
435 STAT5A to DNA oligos containing the predicted -194 STAT5A binding site on the RUNX2
436 promoter (wt RUNX2 oligo). This interaction was validated by challenging the oligo-STAT5
437 complex with increasing amounts of unlabeled (cold) oligos. Moreover, the binding was entirely
438 abrogated by incubating the STAT5 extract with oligos where the STAT5A binding site was
439 entirely randomized (mut RUNX2 oligo) (**Supplementary Figure 5G**). Supporting a role for

440 STAT5 in osteogenic reprogramming, STAT5 protein levels were significantly lower in the aorta
441 of *Tert*$^{-/-}$ mice fed the A6P6 diet compared to the aorta from *Tert*$^{+/+}$ mice (**Supplemental Figures**
442 **5H**), and these findings were replicated in the ex vivo calcification assay (**Supplemental Figure**
443 **5I**). These experiments demonstrate that STAT5 directly acts on DNA in the *RUNX2* promoter
444 and contributes to osteogenic reprogramming in cardiovascular tissues.
445
446 While the domains of TERT were initially defined by their role in the telomere-extending
447 functions of TERT, protein partners required for the known non-canonical functions of TERT
448 have been found in several domains throughout the protein.[70] Further, sites for protein binding
449 partners to STAT5, such as epigenetic modifiers and transcriptional regulators, have been found
450 throughout the protein.[71] We used AI-assisted technology to generate tertiary structures of
451 TERT and STAT5 dimers and predict how they may interact. AlphaFold[72] mapped the
452 interaction between human TERT and dimerized human STAT5A, and these binding data were
453 visualized using HDOCK[73] (**Supplemental Figure 5J and 5K**). To gain a more comprehensive
454 and detailed understanding of the TERT/STAT5 interaction we will utilize a next-generation
455 fluorescence-based complementation system developed by Tebo and Gautier in 2019
456 (splitFAST).[74] This system has very low background fluorescence and can be temporally
457 regulated, enabling the visualization of transient TERT/STAT5 interactions in living cells or fixed
458 cells, to provide a scalable model that can be used to screen for compounds that block the
459 TERT/STAT5 interaction. We fused the human cDNA of TERT and STAT5 to NFAST and
460 CFAST splitFAST reporters, respectively, to generate TERT-NFAST and STAT5A-CFAST
461 fusion proteins. This approach allows monitoring of the formation and dissociation of a protein
462 assembly.[74] Control hVICs were co-transfected with TERT-NFAST and STAT5A-CFAST
463 plasmids and 5 μM HBR-3,5DOM (4-hydroxy-3,5- dimethoxy benzylidene rhodamine)
464 administered at d3, d5, and d7 of OST or NT. We found that the TERT/STAT5 splitFAST signal

465 was highly elevated in calcifying control hVICs relative to the NT condition as early as d3
466 throughout d7, supporting the early formation of the TERT/STAT5 complex in calcifying hVICs
467 (**Figure 4L**). Together, these approaches confirm TERT and STAT5 interaction and
468 translocation into the nucleus during osteogenic reprogramming.
469
470 To assess the function of TERT-STAT5 interaction, we performed chromatin
471 immunoprecipitation analysis (Ch-IP). We found that STAT5 is significantly enriched on both
472 putative STAT5 binding sites in the *RUNX2* promoter during osteogenic reprogramming (**Figure**
473 **4M**). *RUNX2* transcription is initiated from two distinct promoters: the distal promoter region P1,
474 located upstream of exon 1, and the proximal P2 promoter, located upstream of exon 2.[75,76] The
475 P1 promoter is highly active and required for osteoblast progenitor expansion, osteoblast
476 maturation, and bone formation, while the P2 promoter-derived isoform is expressed in
477 osteoblastic and non-osteoblastic mesenchymal cells.[77-79] Genome-wide CUT&Run analysis of
478 the histone marker H3K4me3 showed that RUNX2 promoters P1 and P2 are significantly
479 upregulated during osteogenic differentiation on human VICs, while Gene Ontology (GO)
480 pathway analysis revealed that genes related to the telomerase complex, chromatin remodeling,
481 and metabolic pathways are upregulated during osteogenic differentiation of hVICs
482 (**Supplementary Figures 5L and 5M**, GEO accession GSE280657). We assessed STAT5
483 binding to the *Runx2* P1 and P2 promoters during osteogenic differentiation using CUT&Tag
484 analysis in the *Tert*$^{+/+}$ and *Tert*$^{-/-}$ mVICs. We found that STAT5 binds to the *Runx2* P1 and P2
485 promoters during osteogenic differentiation and that STAT5 was absent from these regions in
486 *Tert*$^{-/-}$ mVICs, highlighting the Tert requirement for Stat5 binding to *Runx2* gene promoters
487 (**Figure 4N**, GEO accession GSE274226). By comparing *Tert*$^{+/+}$ and *Tert*$^{-/-}$ mVICs CUT&Tag
488 sequencing, we found that Stat5 occupies promoter, intragenic, and intergenic regions
489 throughout the genome (**Figure 4O**). GO pathway analysis revealed that genes with high Stat5

490 binding participate in biological processes related to protein phosphorylation, JAK/STAT
491 signaling, inflammation, osteoblast differentiation, SMC function, and chromatin remodeling
492 (**Figure 4P**). Together, these data identify that TERT's effects are mediated via STAT5 binding
493 on the *Runx2* gene promoter and the promoters involved in several pathways known to be
494 operative during osteogenic reprogramming of cardiovascular cells.
495
496 **TERT and STAT5 are upregulated in calcified tissue.**
497 Confirming our in vitro, ex vivo, and in vivo data above, in human CAVD tissue we found that
498 STAT5 protein levels are significantly elevated and localized to areas of calcification in the
499 calcified leaflet alongside TERT distribution. Additionally, the number of STAT5-positive cells
500 was significantly higher in CAVD tissue compared to control tissue (**Figure 5A**). Furthermore,
501 the number of TERT/STAT5 co-positive nuclei was significantly greater in CAVD valves
502 compared to control valves (**Figure 5B**). These data support our in vitro investigations and
503 indicate that TERT/STAT5 interaction contributes to human CAVD pathogenesis.
504
505 **TERT interacts with SMARCA4 during the osteogenic reprogramming of VICs.**
506 Studies by others have shown that TERT facilitates chromatin accessibility and transcription by
507 recruiting SMARCA4 (previously referred to as BRG1), the catalytic subunit of the SWI/SNF
508 chromatin remodeling complex, to specific DNA loci.[18,80,81] We investigated whether SMARCA4
509 plays a role in the osteogenic reprogramming of hVICs via interacting with TERT. There was no
510 difference in SMARCA4 protein staining in the aorta of *Tert*$^{+/+}$ and *Tert*$^{-/-}$ mice fed the A6P6 diet,
511 nor in aortic rings ex vivo (**Supplemental Figures 6A and 6B**). However, in hVICs, expression
512 analysis revealed significant upregulation of *SMARCA4* transcripts as early as d5 of OST
513 stimulation (**Supplementary Figure 6C**). Immunoprecipitation showed that TERT and
514 SMARCA4 physically interact in hVICs upon OST treatment (**Supplementary Figure 6D**).

515 Immunofluorescence staining showed that TERT and SMARCA4 are detected and colocalized
516 in cells in the calcified human leaflet (**Supplementary Figure 6E**), mirroring TERT and STAT5
517 distribution in human CAVD tissue. These findings suggest that SMARCA4 plays an active role
518 in the osteogenic reprogramming of VICs.
519

520 **DISCUSSION**

521 This study investigated the early steps required for the osteogenic reprogramming of human
522 valve interstitial cells in CAVD and establishes a critical role for TERT and STAT5 in this
523 process (**Figure 6**). Specifically, our data show that 1) TERT is upregulated in CAVD tissue and
524 elevated in primary VIC lines stimulated with osteogenic media. While TERT is elevated in these
525 calcified tissues and cells, telomere length is not impacted, nor is there evidence of cell
526 senescence; 2) TERT is required for the calcification of VICs, CASMCs, and MSCs. The
527 requirement for TERT occurs early in the process of osteogenic reprogramming, as knocking
528 down TERT protein levels after seven days of osteogenic stimulation did not deter calcification.
529 These osteogenic reprogramming activities of TERT are independent of its telomerase
530 enzymatic activity, as *Terc*$^{-/-}$ cells or the use of the TERT reverse transcriptase inhibitor did not
531 deter calcification. Further, TERT co-immunoprecipitated with the chromatin remodeling enzyme
532 SMARCA4, and these two proteins were also found in the nucleus of CAVD tissues; 3)
533 Inflammatory signals are known to contribute to CAVD pathogenesis, and we found such
534 signaling can increase TERT levels, as well as the transcription factor STAT5. In silico modeling
535 predicted TERT/STAT5 interaction, which was proven experimentally with immunoprecipitation,
536 proximity ligation assay, and a fluorescence complementation system developed for the
537 visualization of transient protein-protein interactions, and like TERT, genetic knockdown of
538 STAT5, or specific inhibition of STAT5 activity, prevented calcification. We found that STAT5

539 directly binds the DNA of the RUNX2 promoter, as well as genes in pathways related to
540 chromatin remodeling and cellular proliferation and differentiation. Lastly, the requirement for
541 TERT was established in in vivo and ex vivo calcification models. Collectively, these
542 experiments support a novel role for TERT and STAT5 in driving CAVD pathogenesis and
543 cardiovascular reprogramming and identify a unique, druggable target for cardiovascular
544 calcification.
545
546 TERT is well-known for its canonical telomere-extending activity, yet TERT also regulates gene
547 expression and chromatin remodeling independent of affecting telomere integrity. TERT
548 interacts physically with several transcription factors to promote the expression of several
549 genes, including β-catenin, to stimulate genes involved in bone development.[15,16,62] In a wire-
550 injury restenosis model, TERT binds to the transcription factors SP1 at the *VEGF* promoter and
551 E2F1 at *MCM7*, *CCNA1*, and *PCNA* promoters, stimulating SMC proliferation and neointima
552 formation.[20,56,63,82] We did not detect proliferative or migratory differences between control and
553 CAVD VICs despite elevated levels of TERT at baseline (Figures 2B and 2C), indicating cell-
554 specific and stress-specific functions of TERT.
555
556 In addition to supporting transcription factor function, TERT can act as a cofactor to orchestrate
557 chromatin remodeling machinery. Studies have shown that TERT serves as a chaperone to
558 facilitate the recruitment of SMARCA4 and histone acetyltransferases to stimulate chromatin
559 accessibility and transcription or to maintain heterochromatin structure,[18,80,81] and loss of TERT
560 abrogates the cellular response to DNA double-strand breaks and alters the overall chromatin
561 configuration without affecting telomere integrity.[17] We now show that TERT is upregulated in
562 calcified valve tissues and VICs under osteogenic and inflammatory stimuli. TERT interacts with
563 STAT5, which binds to the *RUNX2* gene promoter and drives osteogenic reprogramming of the

564 aortic valve cells. TERT depletion reduced *RUNX2* expression and calcification in several cell
565 types, and TERT, STAT5, and the chromatin remodeling enzyme SMARCA4 co-
566 immunoprecipitated in OST-treated VICs (Supplementary Figure 6). Further, TERT and
567 SMARCA4 co-localized in the nucleus of CAVD tissues. These discoveries, along with the
568 findings of others showing that *TERT* overexpression drives osteogenic differentiation in human
569 MSCs,[21,22] support a broad role for TERT serving as a co-factor bridging chromatin remodeling
570 complexes and transcription factors to facilitate euchromatin formation to modulating cellular
571 phenotypic transition and osteogenic reprogramming.
572
573 Telomere length is considered a biomarker of aging, yet it varies widely between people of the
574 same age, even twins.[23] Several studies have utilized circulating leukocytes to investigate
575 whether shortened telomeres correlate with various vascular disease states.[24,25] One study
576 correlated telomere length in circulating leukocytes with aortic stenosis and found that leukocyte
577 telomere length was slightly shorter in individuals with aortic stenosis than in age-matched
578 controls.[26] However, telomere length in leukocytes does not indicate global telomere length in
579 an individual, telomerase complex activity, or TERT protein function in all cell types. Further,
580 somatic mosaicism and clonal hematopoiesis discoveries underscore the importance of not
581 ascribing telomere length in one cell type to telomere length and/or TERT activities in another.[28]
582 Short telomeres in circulating leukocytes may reflect increased cell turnover due to systemic
583 inflammation, as leukocytes are highly proliferative, and telomere attrition is highly likely to be a
584 tissue- and disease-dependent process. In this regard, Huzen et al. compared the telomere
585 length of the leukocytes of age-matched controls and patients with atherosclerosis and the
586 telomere length of the cells in the atherosclerotic plaques of the patients.[27] They found that
587 while telomere length in leukocytes from the atherosclerosis patient group was significantly
588 shorter than in the control group, telomere length in the atherosclerotic plaques was significantly

589 longer, indicative of increased telomerase activity. Thus, total leukocyte telomere length does
590 not represent telomere length in the diseased tissue. Our study investigated TERT protein levels
591 directly in the valve tissue and patient-specific VICs. We determined that the expression levels
592 of TERT and osteogenic markers in CAVD tissue and cells were elevated, without changes in
593 telomere length, proliferation, and DNA damage markers (Figures 1-2, Supplemental Figures 1-
594 4), suggesting non-canonical TERT activity in these cells.
595
596 VIC calcification shares aspects of the transcriptional program observed during the
597 differentiation of MSCs into osteoblasts, including the upregulation of *RUNX2, BGLAP, TNAP*,
598 and the secretion of bone-forming proteins and accumulation of calcium minerals.[10,12,83]
599 Likewise, signals such as mechanical stress, disturbed flow, and inflammation promote VIC
600 calcification and the osteogenic differentiation of MSCs.[84] These observations suggest that VICs
601 switch from their quiescent state and undergo an osteogenic reprogramming akin to the
602 differentiation of MSCs into osteoblasts, acquiring a calcifying phenotype. The mechanisms
603 coordinating the early molecular events in these cell transitions have yet to be fully understood.
604 We have hypothesized that fully differentiated cells can de-differentiate into a transitory,
605 multipotent stem cell-like state and then acquire an osteogenic phenotype.[85] VICs exhibit the
606 potential to differentiate into osteogenic, chondrogenic, or adipogenic lineages, properties
607 comparable to mesenchymal stem cells.[86] We chose to investigate TERT in the osteogenic
608 reprogramming of VICs as TERT is highly expressed in stem cells, and its overexpression
609 primes mesenchymal stem cells into the osteogenic lineage.[21,22] Our data supports the role of
610 TERT in the osteogenic reprogramming of VICs, whereby TERT serves as a bridge between
611 DNA-binding transcription factors and chromatin remodeling enzymes.
612

613 The osteogenic differentiation of stem cells is orchestrated by RUNX2, which is also required for
614 the osteogenic reprogramming of valvular and vascular cells.[40,41] In a recent transcriptomic
615 study, Xu et al. identified 14 cell populations in aortic valve tissue samples from two control and
616 four CAVD valves.[87] The severity of CAVD was assessed via ultrasound imaging, which detects
617 leaflet mobility; however, examining the macroscopic pictures and histological staining of valve
618 leaflets used in this analysis shows that while these valves are indeed stiff, they do not exhibit
619 robust nodules of calcification as do the valves in our data set (Figures 1, 5, and Supplemental
620 Figure 1). Analysis by Xu et al identified three VIC populations defined by expression of *FOS,*
621 *HSPA6, and SPARC.* However, cells from six valves were pooled, with 10.4% of cells from
622 control tissue and the remaining 89.6% from CAVD tissues. Bulk transcriptomic data from these
623 tissues show only a small 1.49-fold increase in *RUNX2* gene expression in CAVD tissues, in
624 stark contrast with our more stringent analysis of *RUNX2* expression by quantitative PCR
625 (Figure 2, Supplemental Figure 4).[10-12] Inspection of the publicly available bulk RNA-sequencing
626 data (PRJNA552159) showed no increase in *TERT* transcript expression. While the
627 hemodynamic data showed those valves had undergone fibrotic remodeling, few calcifying cells
628 were present, as seen by their histological staining. This lack of calcification may explain why
629 TERT expression was undetected in their study. In the general population, aortic sclerosis
630 commonly goes undetected until a patient develops symptoms such as dyspnea, angina, and
631 syncope, as the stiffness and remodeling of the leaflet obstructs ventricular outflow. A
632 population-based study assessed aortic valve disease in 552 randomly selected men and
633 women aged 55 to 86. Using imaging and Doppler echocardiography, mild calcification was
634 observed in 40% of the individuals, severe calcification in 13%, and symptomatic stenosis in
635 only 2.2%.[88] This population-based study illustrates how common aortic valve remodeling is and
636 highlights the importance of using multiple modalities to accurately determine valve pathology
637 (i.e., fibrotic vs calcified). In our study, a portion of each patient valve was used for cell isolation

638 while the rest was utilized for calcification assessment by histological staining, following a
639 workflow that we developed that guarantees that cells isolated from surgically removed and
640 postmortem tissues retain their proliferative capacity and endothelial and interstitial phenotypes
641 in culture.[37] While unbiased sequencing approaches may help uncover novel mechanisms
642 contributing to disease states, they are skewed towards genes exhibiting the largest changes in
643 gene expression in a snapshot of time and can miss short-lived transitory events.
644
645 The function of STAT5 in bone formation is multifaceted. While it was shown that STAT5 could
646 promote the differentiation of MSCs into osteoblasts by upregulating the osteogenic genes in a
647 Jak2-dependent manner, a *Stat5a* global knockout mouse exhibited elevated bone mass and
648 mineral density.[89,90] These conflicting reports indicate that the role of STAT5 in bone formation
649 and remodeling is complex, and more studies are required. STAT5 has diverse functions as a
650 transcription factor: it interacts with histone acetyltransferases and transcription factors such as
651 the glucocorticoid receptor, SP1, YY1, and C/EBPβ to stimulate gene expression,[91-93] and
652 studies in cancer cells identified that STAT5 can induce *TERT* expression.[94,95] Using in silico
653 modeling we found multiple putative STAT5 binding sites in the *RUNX2* P1 promoter region,
654 which were confirmed with Ch-IP assays. This supports our hypothesis that STAT5/TERT acts
655 to initiate the osteogenic reprogramming of VICs, establishing a novel mechanism in CAVD
656 pathogenesis whereby TERT/STAT5 bind to each other and activate osteogenic gene
657 transcription, which drives the early events in cellular osteogenic reprogramming. Cell
658 phenotype reprogramming requires chromatin restructuring to allow for the transcription of
659 repressed genes. As observed in other cell types, we found TERT co-immunoprecipitated with
660 SMARCA4, as well as STAT5, and genetic depletion of TERT or STAT5 midway through the
661 OST assay (i.e., after d7) did not perturb the calcification of cells. Our observations strongly
662 supports that TERT complexes with SMARCA4 to remodel chromatin and with the STAT5

663 transcription factor to bind and activate *RUNX2* gene transcription. We explored the potential
664 physical direct interaction between TERT and STAT5, and we propose that the RNA binding
665 domain of TERT is the most likely candidate to interact with STAT5 (Supplemental Figure 5).
666 This location is of interest, as we found that *Terc*$^{-/-}$ *mVICs* robustly calcify; this begs the question
667 of whether the loss of *lncTERC* binding is what enables or regulates the non-canonical activities
668 of TERT. Studies identifying critical domains for interaction are currently ongoing.
669
670 The strengths of this study lie in the utilization of patient-specific tissues and cell lines generated
671 from valve leaflets, and the use mouse models and knockout cells for mechanistic studies.
672 While our results are robust, it is important to address the limitations of our study. Firstly, we
673 worked with a limited number of human samples obtained from age- and sex-matched donors.
674 Due to this limited sample size, we limited our statistical analyses to non-parametric analysis,
675 comparing two to four groups, and no mixed models were included. Regardless, one strength of
676 our study is the multiprong approach to determining the role of TERT and STAT5 in vascular
677 calcification. Secondly, STAT5A and STAT5B are two different genes, with 96% of their amino
678 acid sequence shared and their activities redundant.[32] We have determined that VICs express
679 both variants; however, our antibodies and shRNA constructs could not differentiate between
680 the two variants. Thus, the two isoforms may interact with TERT to bind the *RUNX2* gene
681 promoter. STAT5 is activated by multiple cytokines, including IL-2, IL-6, and TNF-α, and it was
682 shown that IL-2 specifically activates STAT5 to induce TERT expression in cancer cells.[94,96]
683 Whether STAT5 first induces TERT expression and then TERT and STAT5 cooperate to control
684 the expression of *RUNX2* needs to be determined. Thirdly, there is redundancy regarding
685 STAT1/3/5 functions and signaling.[97] Our study was not designed to address all the
686 complexities of STAT signaling per se but rather to investigate the role of TERT as a key protein

687 that orchestrates the osteogenic reprogramming of aortic valve cells; our future studies will
688 explore the role of STAT5 further.
689
690 Our work highlights the importance of primary human tissue-based studies. Murine models are
691 not ideal for studying non-genetic drivers of CAVD, as mice do not develop CAVD de novo.[98,99]
692 Mouse leaflets' structure differs from human leaflets as they lack a trilaminar organization and
693 present a melanocyte cell population not present in human valves.[100-102] Recent elegant work
694 from the Giachelli group showed that in mice, calcification happens in the sinus wall and, to a
695 lesser extent, at the leaflet hinge, the region between the leaflet VICs and SMCs of the aorta,
696 with no detectable calcification in the aortic valve leaflets after 26 weeks of a high-fat diet in a
697 *Ldlr* knockout mice model.[103] This distribution of aortic root calcification is also observed in a
698 mouse model described by a Honda et al which detected calcification in the sinus wall 16 weeks
699 post wire-induced mechanical injury.[98] Due to the lack of aortic valve leaflet calcification in
700 atherosclerotic or mechanical injury murine models, we utilized a adenine/phosphate diet-
701 induced model of medial arterial calcification (MAC).[58] MAC is not associated with lipid
702 deposition, fibrous cap formation, or intimal hyperplasia; instead, MAC stems from the
703 progressive accumulation of calcium and phosphate within the arterial walls.[104] These structural
704 features distinguish MAC from atherosclerosis and are more representative of the pathogenesis
705 of valve leaflet calcification.[2,104]
706
707 This study has uncovered the early molecular events that enable the osteogenic reprogramming
708 of the interstitial cells of the aortic valve. Current CAVD therapies are surgical, limited to
709 mechanical or bioprosthetic valve replacement, and performed only when the disease has
710 progressed to the advanced point of affecting blood flow and heart function. Our data show that
711 perturbing TERT or STAT5 can inhibit calcification; however, broadly inhibiting one or the other

712 of these proteins may have deleterious off-target effects. Understanding the specific binding
713 domains and other protein binding partners of TERT and STAT5 will enable the development of
714 small molecules to block their interaction, which is a more feasible therapeutic strategy for aortic
715 valve calcification than global inhibition. CAVD affects over 9.5 million people in the U.S. and
716 has an associated 56-67% 5-year mortality rate; hence, the need for early, non-surgical
717 therapies is great.[4] This study uncovers a novel and targetable pathway that may be leveraged
718 to halt or prevent CAVD progression.
719

720 **ACKNOWLEDGEMENTS**

721 We want to acknowledge and thank the Center for Organ Research and Education for their help
722 and support, as well as tissue donors and their families for making this study possible. We thank
723 Dr. Alison Tebo for her guidance and assistance in constructing the SplitFAST plasmids tool
724 used in this study. We would also like to thank Kristin Konopka, tissue bank coordinator at The
725 Department of Cardiothoracic Surgery, UPMC. We thank Jason Dobbins for his critical reading
726 of this manuscript.
727

728 **SOURCES OF FUNDING**

729 This study was supported by funds from the National Institutes of Health (R01 HL142932, R56
730 HL168657, St. Hilaire), the American Heart Association (20IPA35260111, St. Hilaire; 902641,
731 Cuevas; 24POST1186619, Behzadi), the McKamish Family Foundation (St. Hilaire and Sultan)
732 and the Samuel and Emma Winters Foundation (St. Hilaire).
733

734 **DISCLOSURES**

735 The University of Pittsburgh has filed a provisional patent application regarding technology on
736 behalf of CSH and RAC based on the findings presented in this manuscript. IS receives

737 institutional research support from Atricure and Medtronic and is a consultant for Medtronic
738 Vascular. None of these conflicts of interest are related to this work. All other authors have nothing
739 to disclose.
740
741 **FIGURE LEGENDS**
742 **Figure 1. TERT is elevated in CAVD tissues.** (A) Examples of non-calcified control (top) and
743 calcified CAVD (bottom) human valves used in this study. Arrowheads indicate calcified nodules
744 Scalebar. 1 cm. (B), TERT mRNA transcript quantification in control and CAVD valve tissues. n
745 = 8 control, n= 9 CAVD. (C), Representative serial sections of Von Kossa (dark precipitation)
746 and TERT immunofluorescent staining in control and CAVD valve tissues. Scalebar 100 µm.
747 Graphs show the quantification of TERT intensity and the number of TERT-positive cells. n = 9
748 control, n = 9 CAVD. (D), Telomere length measurements in valve tissues. n = 19 control, n =
749 12 CAVD. (E), Age of the patients utilized in this study. n = 25 control, n = 16 CAVD. Data are
750 shown as means ± SD. P values were calculated using the Mann-Whitney U test and shown on
751 each graph. L = lumen.
752
753 **Figure 2. TERT is elevated in CAVD hVICs at baseline and upregulation during**
754 **osteogenic reprogramming.** (A), Representative images showing cell morphology of control
755 and CAVD hVICs. Scalebar 50 µm. (B), Proliferation of control and CAVD hVICs at baseline. n
756 = 3 both groups. (C) Relative migration distances of control and CAVD VICs. n = 10 both
757 groups. (D) Western blot staining of control and CAVD hVICs at baseline. Quantification of
758 protein levels is shown on the right panels. n = 4 both groups. (E) Telomere length
759 measurements in VICs. n = 8, control, n = 5 CAVD. (F) Representative images of early
760 calcification in hVICs growing in normal conditions (no treatment NT) or stimulated with
761 osteogenic media (OST) for 14 days. Calcium deposition was visualized by Alizarin Red

762 staining. Scalebar 50 µm. Quantification of calcification on the right graphs. n = 7 both groups.
763 (G), Western blot staining of samples from control and CAVD hVICs after 14 days of NT or
764 OST. Quantification of protein levels is shown on the bottom graphs. n = 4 both groups. (H),
765 Representative immunofluorescent staining images of TERT in control and CAVD hVICs after
766 14 days of NT or OST. Calcium deposition was visualized with OsteoImage. Scalebar 100 µm.
767 (I) Expression profile control VICs after 14 days of NT and OST treatment. n = 4 both groups.
768 Data are shown as means ± SD. P values were calculated with the Mann-Whitney U test
769 (Figures B, C, D, E, G, and I) and the Kruskal-Wallis H test with Dunn post hoc test (Figure F)
770 and shown on each graph
771
772 **Figure 3. TERT is required to initiate osteogenic transition and calcification.** (A) Control
773 hVICs were transduced lentivirus containing shControl or shTERT and followed by OST
774 stimulation for up to 28 days. Calcium deposition was visualized by Alizarin Red staining. n = 6
775 shControl, n = 6 shTERT at 21 days and n = 9 each group at day 28. Scalebar 400 µm. (B)
776 Representative western blot staining of control hVICs transduced with lentivirus containing
777 either shControl or shTERT followed by 7 days of OST. (C) hCASMCs were transduced with
778 shControl or shTERT and stimulated with OST for 14 and 21 days. n = 4 for each group at both
779 time points. Scalebar 400 µm. (D) Representative images of mVIC isolated from *Tert*$^{+/+}$ and *Tert*$^{-}$
780 $^{/-}$ mice were stimulated with OST for 28 days. Scalebar 400 µm. (E) Representative Von Kossa
781 staining images of *Tert*$^{+/+}$ and *Tert*$^{-/-}$ mice aortas (dark precipitation). Scale bar 400 µm.
782 Quantification of calcification is shown on the right panel. (F) Representative immunofluorescent
783 images of Runx2 expression indicative of calcification (red, insert) on *Tert*$^{+/+}$ and *Tert*$^{-/-}$ mice
784 aorta. Scale bar 400 *µ*m. Runx2 quantification of calcification is shown on the right panel. (G)
785 Representative images of mVICs isolated from F1 *Tert*$^{-/-}$ *or Terc*$^{-/-}$ mice were stimulated with
786 OST for up to 21 days. Scalebar 100 µm. Data are shown as means ± SD. P values were

787 calculated using the Kruskal-Wallis H test, Dunn post hoc test (Figures A, C, and G), and Mann-
788 Whitney U test (Figures D, E, and F).
789
790 **Figure 4. STAT5 binds to TERT and is required for the calcification of human VICs.** (A)
791 Graphic of in silico analysis identifying the consensus binding site for STAT5. (B), Diagram
792 depicting STAT5 binding to RUNX2 promoter and the positions of the predicted STAT5 binding
793 sites (purple boxes). (C) Representative immunofluorescence images of control hVICs after 14
794 days of LPS treatment or OST stimulation. Scalebar 50 µm. (D) Representative western blot
795 staining of hVICs after 14 days of OST stimulation. (E) Representative images of control hVICs
796 treated with 10 µM of the STAT5 inhibitors StafiA-1 or StafiB-1 throughout 28 days of
797 osteogenic stimulation. Scalebar 400 µm. n = 8 each group. The quantification of calcification is
798 shown on the right graph. (F) RUNX2 mRNA transcript quantification at d7 OST, n = 10. (G)
799 Control hVICs were transduced with lentivirus containing shControl or shSTAT5 constructs and
800 treated with OST for 21 days. Calcium deposition was visualized by Alizarin Red staining. n = 9
801 for each group. Scalebar 400 µm. (H) RUNX2 mRNA transcript quantification at d7 OST, n = 6.
802 (I) Schematic of OST treatment with delayed shTERT transduction (top panel).Representative
803 images of hVIC (left panels) treated with 10 µM of the STAT5 inhibitors StafiA-1 at d7 or d14 of
804 OST treatment. Samples were collected at d21 (bottom panel). Scalebar 400 µm. n = 6 for each
805 group. (J) Representative images of TERT/STAT5 complex (red foci) in control hVICs cultured
806 for 21 days in osteogenic medium and detected by PLA. Scalebar 100 µm. n = 4 for each group.
807 (K) STAT5 co-immunoprecipitation in control hVICs under OST for 10 days to detect
808 TERT/STAT5 interaction. (L) Control hVIC co-expressing TERT-NFAST and STAT5A-CFAST
809 were labeled with 5 µM HBR-3,5DOM (4-hydroxy-3,5- dimethoxybenzylidene rhodamine, coral)
810 and imaged at d3, d5, and d7 of osteogenic treatment (OST) or control no-treatment (NT). Scale
811 bars 50 µm. (M) Chromatin immunoprecipitation shows enrichment of STAT5 on RUNX2

812 promoter OST conditions compared to NT. The base position is indicated in the blue boxes. n=4
813 for each group as in B. (N) STAT5 CUT&Tag sequencing tracks in genomic regions of Runx2 in
814 no-treatment control and osteogenic condition-treated mice VICs. (O) Stacked chart
815 representing genome-wide STAT5 occupancy in promoters, genes, and intergenic regions
816 frequency in mice VICs. (P) Top 20 GO pathways enriched in genes with significant loss of
817 STAT5 in Tert+/+ vs Tert-/- mice VICs. Data are shown as means ± SD. P values were
818 calculated by the Mann-Whitney U test (Figures F, H, and J) and the Kruskal-Wallis H test
819 (Figures E and G) and indicated on top of each graph.
820
821 **Figure 5. TERT and STAT5 are upregulated and colocalized in CAVD tissue.** (A)
822 Representative serial sections of Von Kossa (dark precipitation) and TERT and STAT5
823 immunofluorescent staining in control and CAVD tissues. Scalebar 100 µm. STAT5 intensity
824 and STAT5-positive cells (STAT5+) are quantified on the right panels. (B) Quantification of
825 STAT5-TERT-positive cells. Data are shown as means ± SD, n = 5 control, n = 6 CAVD. P
826 values were calculated with the Mann-Whitney U test and indicated on each graph. L = lumen.
827
828 **Figure 6. TERT/STAT5 promotes osteogenic reprogramming.** Inflammatory signals promote
829 the upregulation and interaction of TERT and STAT5A. The TERT/STAT5 complex translocates
830 into the nucleus, where TERT interacts with SMARCA4 (also known as BRG1), which facilitates
831 a permissive chromatin configuration, and STAT5A binds specific sites on the RUNX2 promoter,
832 leading to the osteogenic reprogramming of valve interstitial cells during the early stages of
833 CAVD pathogenesis.
834
835 **Supplemental Figure 1. Characterization of human CAVD valves and patient-isolated**
836 **VICs at baseline.** (A) Representative section of Von Kossa staining in control and valve CAVD

837 leaflets tissue. Scalebar 1 mm. (B) Representative serial sections of RUNX2 immunofluorescent
838 staining and OPN in control and CAVD valve tissues. Scalebar 100 µm. Quantification of
839 RUNX2-positive cells and OPN-positive cells on the leaflet specimen is shown on the right
840 graphs. n = 5 control, n = 6 CAVD. (C) Correlation between age of the donor and TERT
841 expression in valve tissues. n = 8 control, n = 9 CAVD. (D) Gene expression profile in the valve
842 leaflets. n = 7 each group. (E) Representative images of immunofluorescent staining of PCNA
843 (top panels) and γ-H2AX (bottom panels) in control and CAVD valve tissues. Scalebar 100 µm.
844 Quantification of PCNA-positive cells and γ-H2AX-positive cells are shown on the right graphs.
845 n = 4 control, n = 3 CAVD. (F) Representative images of a scratch assay in control and CAVD
846 hVICs. Time points are indicated on top of each panel. Blue lines denote the cell migration front.
847 Scalebar 1 mm. n = 10 of each group. (G) Representative images of αSMA, CNN, SM22, TNAP,
848 and f-Actin in control and CAVD hVICs. Scalebar 50 µm. Signal quantification is shown on the
849 right. n = 4 each group. Data are shown as means ± SD. P values were calculated using the
850 Mann-Whitney U test (Figures B, D, E, and G) and the Pearson correlation test (Figure C). L =
851 lumen.
852
853 **Supplemental Figure 2. Inhibition of reverse transcriptase activity of TERT does not**
854 **prevent osteogenic reprogramming of hVICs**. (A) Cell counts of control and CAVD hVICs
855 after 14 days of NT or OST stimulation. n = 4 each group. (B) β-galactosidase (BLG1) mRNA
856 transcript quantification in control and CAVD hVICs at baseline. n = 5 control, n= 4 CAVD. (C)
857 Representative images of senescence-associated β-galactosidase activity staining of hVICs
858 after 28 days of NT or OST stimulation. Blue cells were considered positive for senescence.
859 Quantification of senescence is shown on the right graph. n = 4 each group. Scalebar 400 µm.
860 (D) hVICs growing in no treatment (NT), OST media, or OST media supplemented with the NF-
861 κβ inhibitor BAY-117082 for 7 days, n = 6. (E) hVICs growing in no treatment (NT), OST media,

862 or OST media supplemented with the c-MYC inhibitor 10058-F4 for 7 days, n = 7. qRT-PCR
863 quantified TERT and RUNX2 gene expression. In D and E, inhibitors were dissolved in DMSO
864 thus NT and OST were supplemented with the highest volume of vehicle (DMSO) used in
865 treatment groups. Data are shown as means ± SD. P values were calculated with the Mann-
866 Whitney U test (Figure B) and the Kruskal-Wallis H test with Dunn pairwise comparison post hoc
867 test (Figures A, C-E) and shown on top of each graph.
868
869 **Supplemental Figure 3. TERT is upregulated and required for the osteogenic**
870 **differentiation of human mesenchymal stem cells**. (A) Representative images of hMSCs
871 stimulated with OST for 14 days. Calcium deposition was visualized by Alizarin Red staining.
872 Scalebar 50 µm. (B) Western blot staining of samples from hMSCs collected during the 14 days
873 of OST treatment. (C) RUNX2 expression profile of differentiating hMSCs stimulated for 14 days
874 with OST media. n = 3. (D) Representative TERT immunofluorescent staining images of hMSCs
875 stimulated with OST for 14 days. Scalebar 100 µm. (E) Representative images of hMSCs
876 infected with shTERT or shControl virus and stimulated with OST for 14 days. Calcium
877 deposition was visualized by Alizarin Red staining. The quantification of calcification is shown
878 on the right graph. n = 3. (F) Western blot staining of samples from hMSCs collected during the
879 14 days of OST treatment. Data are shown as means ± SD. P values were calculated with the
880 Kruskal-Wallis H test with Dunn pairwise comparison post hoc test (Figure C) and the Mann-
881 Whitney U test (Figure E) and shown on each graph.
882
883 **Supplemental Figure 4. Inhibition of reverse transcriptase activity of TERT does not**
884 **prevent osteogenic reprogramming of VICs.** (A) Representative images of mBMMSCs
885 isolated from *Tert*$^{+/+}$ or *Tert*$^{-/-}$ mice and stimulated with OST for 21 days. Scalebar 100 µm.
886 Quantification of calcification is presented as average absorbance on the right graphs, n = 5 for

887 each group. (B, C) Representative images of a senescence-associated β-galactosidase (SA-β-
888 gal) staining of mVICs and mBMMSCs isolated from *Tert*$^{+/+}$ or F1 *Tert*$^{-/-}$ mice after 21 days of
889 OST stimulation. In each group, blue cells were considered positive for senescence, n = 5. (D)
890 Schematic of OST treatment with delayed shTERT transduction (top panel). VICs were
891 transduced with shTERT, and calcification was assessed with Alizarin Red S stain at day 21.
892 Scalebar 400 µm. n = 6 for each group. (E) Representative sections of Von Kossa staining in
893 thoracic aortic rings isolated from *Tert*$^{+/+}$ and *Tert*$^{-/-}$ mice after 14 days of OST treatment relative
894 to NT control treatment. Quantification is shown on the right. Scale bar 400 *µ*m (F)
895 Immunofluorescence staining of thoracic aortic rings after OST treatment as in B. Quantification
896 of Runx2 is shown on the right graph. Scale bar 400 *µ*m (G) Western blot staining of aortic ring
897 specimens collected and treated in B. Quantification of Runx2 is shown on the right graph. (H)
898 Human VICs were treated with the TERT inhibitor BiBR1532 and stimulated with OST, and
899 calcification was assessed on day 28, with n = 5 in each group. (I) TERT, RUNX2, and STAT5A
900 expression were evaluated on day 14, n = 6 DMSO, n = 5 BIBR1532. Data are shown as means
901 ± SD. P values were calculated with the Kruskal-Wallis H test with Dunn pairwise comparison
902 post hoc test (Figures A, B, C, E, H) and the Mann-Whitney U test (Figures D, F, G, I) and are
903 shown on top of each graph.
904
905 **Supplemental Figure 5. STAT5 is upregulated, binds to TERT, and is required for**
906 **osteogenic reprogramming of VICs.** (A) Western blot analysis of cytoplasmic and nuclear
907 fractions of TERT from control VICs obtained after seven days of OST stimulation. TUB,
908 (tubuline); H3, (Histone H3); Cyt, cytoplasmic fraction; Nuc, nuclear fraction. (B) Representative
909 immunofluorescence image of STAT5 subcellular distribution after 14 days of NT and OST
910 stimulation. Scalebar 40 µm. (C) Representative images of human CASMCs treated with 10 µM
911 of the STAT5 inhibitors StafiA-1 or StafiB-1 during the 14 days of OST stimulation. Scalebar 400

912 µm. n = 4 for each group. (D) Representative images of human MSCs treated with 10 µM of the
913 STAT5 inhibitors StafiA-1 or StafiB-1 during the 21 days of OST stimulation. Scalebar 400 µm. n
914 = 4 for each group. (E) Representative images of TERT/STAT5 complex (red foci) detected by
915 proximity ligation assay (PLA) in the nucleus of control VICs. Scalebar 25 µm. n = 4 for each
916 group. (F) Relative luciferase activity in hVICS after transfection of *hRUNX2* Promoter GLuc-ON
917 pEZX-PG04.1. Samples were analyzed 72 hours after OST treatment. STAT5A inhibitor StafiA-
918 1 (10 µM) was dissolved in DMSO. NT and OST conditions were also supplemented with
919 DMSO, n = 10 per group. (G) Biotin-labeled 60 bp oligos containing the -194 STAT5 binding
920 sequence on the promoter of human RUNX2 were incubated cell extracts from HEK293s in
921 which STAT5 protein was overexpressed (lane 1). Extracts were also incubated with an
922 increasing amounts of unlabeled oligos (lanes 2-5). Cell extract was also incubated with a oligo
923 containing a mutated STAT5A site (mut RUNX2 DNA) (line 9) and incubated with an increased
924 amount of unlabeled mut RUNX2 oligo (lanes 10-13). Blots include the positive and negative
925 controls include in the LightShift Chemiluminescent EMSA Kit (lanes 6-8 and 14-16). (H)
926 Representative immunofluorescent images of Stat5 expression after 12 weeks of high adenine
927 high phosphate diet on Tert-/- and Tert-/- mice aorta. Scale bar 400 μm. Quantification of Stat5
928 expression is shown on the right panel. (I) Representative images of Stat5 immunofluorescence
929 staining of thoracic aortic rings isolated from Tert+/+ and Tert-/- mice after 14 days of OST
930 treatment relative to NT control treatment. Quantification of Stat5 is shown on the right graph.
931 Scale bar 400 μm. (J) Mol*3D Viewer rendering of the TERT-STAT5 dimer interaction predicted
932 by the HDock. Red boxes indicate the position of the interaction between TERT and STAT5. (K)
933 The diagram shows the regions involved in the predicted interaction as indicated in A, and the
934 docking and confidence scores predicted by HDock are indicated. TEN: DNA anchor domain for
935 processive telomeric repeat addition, RBD: Telomerase RNA binding domain, RT: Finger and
936 palm region of the reverse transcriptase domain, CTE: C-terminal extension or putative thumb

937 domain of the reverse transcriptase, CCD: Coiled-coil domain, required for nuclear localization,
938 DBD: DNA binding domain, HLK: Helical linker and DNA binding domain, SH2: Domain required
939 for activation and dimerization, TD: Transactivation domain. (L) H3K4me3 CUT&Run
940 sequencing tracks in genomic regions of Runx2 in no-treatment control and osteogenic
941 condition-treated human VICs. (M) Top 20 GO pathways enriched in genes with significant loss
942 of H3K4me3 in OST- vs NT-treated human VICs. Data are shown as means ± SD. P values
943 were calculated with the Mann-Whitney U test (Figures E and G) and the Kruskal-Wallis H test
944 with Dunn pairwise comparison post-test (Figures C, D, and H) and indicated in each graph.
945
946 **Supplemental Figure 6. Chromatin remodeling enzyme SMARCA4 is upregulated and**
947 **interacts with TERT during the osteogenic reprogramming of VICs.** (A) Representative
948 immunofluorescent images of Smarca4 expression after 12 weeks of high adenine high
949 phosphate diet on *Tert*$^{-/-}$ and *Tert*$^{-/-}$ mice aorta. Scale bar 400 μm. Quantification of Smarca4
950 expression is shown on the right panel. (B) Representative images of Smarca4
951 immunofluorescence staining of thoracic aortic rings isolated from *Tert*$^{+/+}$ and *Tert*$^{-/-}$ mice after
952 14 days of OST treatment relative to NT control treatment. Quantification of Smarca4 is shown
953 on the right graph. (C) SMARCA4 expression was evaluated on days 5 and 10 on VICs
954 stimulated with OST. n = 5 each group. (E) TERT/STAT and TERT/SMARCA4 interaction was
955 detected by co-immunoprecipitation upon osteogenic stimulation on VIC. (E) Representative
956 TERT and SMARCA4 immunofluorescent staining in control and CAVD tissues. The number of
957 positive cells is shown on the right graphs. n = 9 control, n = 9 CAVD. Scalebar 100 µm. Data
958 are shown as means ± SD, and P values were calculated with the Mann-Whitney U test and
959 indicated on each graph in Figures A and C. L = lumen.
960
961 **REFERENCES**

962 1. Kraler S, Blaser MC, Aikawa E, Camici GG, Luscher TF. Calcific aortic valve disease:
963 from molecular and cellular mechanisms to medical therapy. *Eur Heart J*. 2022;43:683-
964 697. doi: 10.1093/eurheartj/ehab757
965 2. Small AM, Yutzey KE, Binstadt BA, Voigts Key K, Bouatia-Naji N, Milan D, Aikawa E,
966 Otto CM, St Hilaire C, American Heart Association Council on G, et al. Unraveling the
967 Mechanisms of Valvular Heart Disease to Identify Medical Therapy Targets: A Scientific
968 Statement From the American Heart Association. *Circulation*. 2024;150:e109-e128. doi:
969 10.1161/CIR.0000000000001254
970 3. Buttner P, Feistner L, Lurz P, Thiele H, Hutcheson JD, Schlotter F. Dissecting Calcific
971 Aortic Valve Disease-The Role, Etiology, and Drivers of Valvular Fibrosis. *Front*
972 *Cardiovasc Med*. 2021;8:660797. doi: 10.3389/fcvm.2021.660797
973 4. Coffey S, Roberts-Thomson R, Brown A, Carapetis J, Chen M, Enriquez-Sarano M,
974 Zuhlke L, Prendergast BD. Global epidemiology of valvular heart disease. *Nat Rev*
975 *Cardiol*. 2021;18:853-864. doi: 10.1038/s41569-021-00570-z
976 5. Roth GA, Mensah GA, Johnson CO, Addolorato G, Ammirati E, Baddour LM, Barengo
977 NC, Beaton AZ, Benjamin EJ, Benziger CP, et al. Global Burden of Cardiovascular
978 Diseases and Risk Factors, 1990-2019: Update From the GBD 2019 Study. *J Am Coll*
979 *Cardiol*. 2020;76:2982-3021. doi: 10.1016/j.jacc.2020.11.010
980 6. Virani SS, Alonso A, Benjamin EJ, Bittencourt MS, Callaway CW, Carson AP,
981 Chamberlain AM, Chang AR, Cheng S, Delling FN, et al. Heart Disease and Stroke
982 Statistics-2020 Update: A Report From the American Heart Association. *Circulation*.
983 2020;141:e139-e596. doi: 10.1161/CIR.0000000000000757
984 7. Rajamannan NM, Evans FJ, Aikawa E, Grande-Allen KJ, Demer LL, Heistad DD,
985 Simmons CA, Masters KS, Mathieu P, O'Brien KD, et al. Calcific aortic valve disease:
986 not simply a degenerative process: A review and agenda for research from the National
987 Heart and Lung and Blood Institute Aortic Stenosis Working Group. Executive summary:
988 Calcific aortic valve disease-2011 update. *Circulation*. 2011;124:1783-1791. doi:
989 10.1161/CIRCULATIONAHA.110.006767
990 8. Chen JH, Simmons CA. Cell-matrix interactions in the pathobiology of calcific aortic
991 valve disease: critical roles for matricellular, matricrine, and matrix mechanics cues. *Circ*
992 *Res*. 2011;108:1510-1524. doi: 10.1161/CIRCRESAHA.110.234237

993 9. Liu AC, Joag VR, Gotlieb AI. The emerging role of valve interstitial cell phenotypes in
994 regulating heart valve pathobiology. *Am J Pathol*. 2007;171:1407-1418. doi:
995 10.2353/ajpath.2007.070251
996 10. Rajamannan NM, Subramaniam M, Rickard D, Stock SR, Donovan J, Springett M,
997 Orszulak T, Fullerton DA, Tajik AJ, Bonow RO, et al. Human aortic valve calcification is
998 associated with an osteoblast phenotype. *Circulation*. 2003;107:2181-2184. doi:
999 10.1161/01.CIR.0000070591.21548.69
1000 11. Rajamannan NM. Calcific aortic valve disease: cellular origins of valve calcification.
1001 *Arterioscler Thromb Vasc Biol*. 2011;31:2777-2778. doi: 10.1161/ATVBAHA.111.237610
1002 12. Aikawa E, Libby P. A Rock and a Hard Place: Chiseling Away at the Multiple
1003 Mechanisms of Aortic Stenosis. *Circulation*. 2017;135:1951-1955. doi:
1004 10.1161/CIRCULATIONAHA.117.027776
1005 13. Wirrig EE, Yutzey KE. Conserved transcriptional regulatory mechanisms in aortic valve
1006 development and disease. *Arterioscler Thromb Vasc Biol*. 2014;34:737-741. doi:
1007 10.1161/ATVBAHA.113.302071
1008 14. Calado RT, Young NS. Telomere diseases. *N Engl J Med*. 2009;361:2353-2365. doi:
1009 10.1056/NEJMra0903373
1010 15. Stewart SA, Hahn WC, O'Connor BF, Banner EN, Lundberg AS, Modha P, Mizuno H,
1011 Brooks MW, Fleming M, Zimonjic DB, et al. Telomerase contributes to tumorigenesis by
1012 a telomere length-independent mechanism. *Proc Natl Acad Sci U S A*. 2002;99:12606-
1013 12611. doi: 10.1073/pnas.182407599
1014 16. Choi J, Southworth LK, Sarin KY, Venteicher AS, Ma W, Chang W, Cheung P, Jun S,
1015 Artandi MK, Shah N, et al. TERT promotes epithelial proliferation through transcriptional
1016 control of a Myc- and Wnt-related developmental program. *PLoS Genet*. 2008;4:e10.
1017 doi: 10.1371/journal.pgen.0040010
1018 17. Masutomi K, Possemato R, Wong JM, Currier JL, Tothova Z, Manola JB, Ganesan S,
1019 Lansdorp PM, Collins K, Hahn WC. The telomerase reverse transcriptase regulates
1020 chromatin state and DNA damage responses. *Proc Natl Acad Sci U S A*.
1021 2005;102:8222-8227. doi: 10.1073/pnas.0503095102
1022 18. Park JI, Venteicher AS, Hong JY, Choi J, Jun S, Shkreli M, Chang W, Meng Z, Cheung
1023 P, Ji H, et al. Telomerase modulates Wnt signalling by association with target gene
1024 chromatin. *Nature*. 2009;460:66-72. doi: 10.1038/nature08137

1025 19. Aono J, Ruiz-Rodriguez E, Qing H, Findeisen HM, Jones KL, Heywood EB, Bruemmer
1026 D. Telomerase Inhibition by Everolimus Suppresses Smooth Muscle Cell Proliferation
1027 and Neointima Formation Through Epigenetic Gene Silencing. *JACC Basic Transl Sci*.
1028 2016;1:49-60. doi: 10.1016/j.jacbts.2016.01.002
1029 20. Endorf EB, Qing H, Aono J, Terami N, Doyon G, Hyzny E, Jones KL, Findeisen HM,
1030 Bruemmer D. Telomerase Reverse Transcriptase Deficiency Prevents Neointima
1031 Formation Through Chromatin Silencing of E2F1 Target Genes. *Arterioscler Thromb*
1032 *Vasc Biol*. 2017;37:301-311. doi: 10.1161/ATVBAHA.116.308717
1033 21. Shi S, Gronthos S, Chen S, Reddi A, Counter CM, Robey PG, Wang CY. Bone
1034 formation by human postnatal bone marrow stromal stem cells is enhanced by
1035 telomerase expression. *Nat Biotechnol*. 2002;20:587-591. doi: 10.1038/nbt0602-587
1036 22. Simonsen JL, Rosada C, Serakinci N, Justesen J, Stenderup K, Rattan SI, Jensen TG,
1037 Kassem M. Telomerase expression extends the proliferative life-span and maintains the
1038 osteogenic potential of human bone marrow stromal cells. *Nat Biotechnol*. 2002;20:592-
1039 596. doi: 10.1038/nbt0602-592
1040 23. Slagboom PE, Droog S, Boomsma DI. Genetic determination of telomere size in
1041 humans: a twin study of three age groups. *Am J Hum Genet*. 1994;55:876-882.
1042 24. Brouilette S, Singh RK, Thompson JR, Goodall AH, Samani NJ. White cell telomere
1043 length and risk of premature myocardial infarction. *Arterioscler Thromb Vasc Biol*.
1044 2003;23:842-846. doi: 10.1161/01.ATV.0000067426.96344.32
1045 25. Samani NJ, Boultby R, Butler R, Thompson JR, Goodall AH. Telomere shortening in
1046 atherosclerosis. *Lancet*. 2001;358:472-473. doi: 10.1016/S0140-6736(01)05633-1
1047 26. Kurz DJ, Kloeckener-Gruissem B, Akhmedov A, Eberli FR, Buhler I, Berger W, Bertel O,
1048 Luscher TF. Degenerative aortic valve stenosis, but not coronary disease, is associated
1049 with shorter telomere length in the elderly. *Arterioscler Thromb Vasc Biol*. 2006;26:e114-
1050 117. doi: 10.1161/01.ATV.0000222961.24912.69
1051 27. Huzen J, Peeters W, de Boer RA, Moll FL, Wong LS, Codd V, de Kleijn DP, de Smet BJ,
1052 van Veldhuisen DJ, Samani NJ, et al. Circulating leukocyte and carotid atherosclerotic
1053 plaque telomere length: interrelation, association with plaque characteristics, and
1054 restenosis after endarterectomy. *Arterioscler Thromb Vasc Biol*. 2011;31:1219-1225. doi:
1055 10.1161/ATVBAHA.110.217158
1056 28. Evans MA, Walsh K. Clonal hematopoiesis, somatic mosaicism, and age-associated
1057 disease. *Physiol Rev*. 2023;103:649-716. doi: 10.1152/physrev.00004.2022

1058 29. Steinmetz M, Schmitter C, Radecke T, Stundl A, Nickenig G, Schaefer C, Schahab N,
1059 Vasa-Nicotera M, Sinning JM. Brief report - Telomere length is a poor biomarker to
1060 predict 1-year mortality or cardiovascular comorbidity in patients with transcatheter aortic
1061 valve replacement. *PLoS One*. 2019;14:e0213250. doi: 10.1371/journal.pone.0213250
1062 30. Leonard WJ, O'Shea JJ. Jaks and STATs: biological implications. *Annu Rev Immunol*.
1063 1998;16:293-322. doi: 10.1146/annurev.immunol.16.1.293
1064 31. Hu X, Li J, Fu M, Zhao X, Wang W. The JAK/STAT signaling pathway: from bench to
1065 clinic. *Signal Transduct Target Ther*. 2021;6:402. doi: 10.1038/s41392-021-00791-1
1066 32. Okutani Y, Kitanaka A, Tanaka T, Kamano H, Ohnishi H, Kubota Y, Ishida T, Takahara
1067 J. Src directly tyrosine-phosphorylates STAT5 on its activation site and is involved in
1068 erythropoietin-induced signaling pathway. *Oncogene*. 2001;20:6643-6650. doi:
1069 10.1038/sj.onc.1204807
1070 33. Wingelhofer B, Neubauer HA, Valent P, Han X, Constantinescu SN, Gunning PT, Muller
1071 M, Moriggl R. Implications of STAT3 and STAT5 signaling on gene regulation and
1072 chromatin remodeling in hematopoietic cancer. *Leukemia*. 2018;32:1713-1726. doi:
1073 10.1038/s41375-018-0117-x
1074 34. Gu L, Liao Z, Hoang DT, Dagvadorj A, Gupta S, Blackmon S, Ellsworth E, Talati P, Leiby
1075 B, Zinda M, et al. Pharmacologic inhibition of Jak2-Stat5 signaling By Jak2 inhibitor
1076 AZD1480 potently suppresses growth of both primary and castrate-resistant prostate
1077 cancer. *Clin Cancer Res*. 2013;19:5658-5674. doi: 10.1158/1078-0432.CCR-13-0422
1078 35. Dieudonne FX, Severe N, Biosse-Duplan M, Weng JJ, Su Y, Marie PJ. Promotion of
1079 osteoblast differentiation in mesenchymal cells through Cbl-mediated control of STAT5
1080 activity. *Stem Cells*. 2013;31:1340-1349. doi: 10.1002/stem.1380
1081 36. Wu X, Chen C, Han T, Bian H, Chen J, Hei R, Meng Y, Wu C, Lu Y, Gu J, et al. Stat5a
1082 promotes Col10a1 gene expression during chondrocyte hypertrophic differentiation. *Am*
1083 *J Transl Res*. 2023;15:4006-4019.
1084 37. Cuevas RA, Chu CC, Moorhead WJ, 3rd, Wong R, Sultan I, St Hilaire C. Isolation of
1085 Human Primary Valve Cells for In vitro Disease Modeling. *J Vis Exp*. 2021:e62439. doi:
1086 10.3791/62439
1087 38. Ducy P, Zhang R, Geoffroy V, Ridall AL, Karsenty G. Osf2/Cbfa1: a transcriptional
1088 activator of osteoblast differentiation. *Cell*. 1997;89:747-754. doi: 10.1016/s0092-
1089 8674(00)80257-3

1090 39. Otto F, Thornell AP, Crompton T, Denzel A, Gilmour KC, Rosewell IR, Stamp GW,
1091 Beddington RS, Mundlos S, Olsen BR, et al. Cbfa1, a candidate gene for cleidocranial
1092 dysplasia syndrome, is essential for osteoblast differentiation and bone development.
1093 *Cell*. 1997;89:765-771. doi: 10.1016/s0092-8674(00)80259-7
1094 40. Sun Y, Byon CH, Yuan K, Chen J, Mao X, Heath JM, Javed A, Zhang K, Anderson PG,
1095 Chen Y. Smooth muscle cell-specific runx2 deficiency inhibits vascular calcification. *Circ*
1096 *Res*. 2012;111:543-552. doi: 10.1161/CIRCRESAHA.112.267237
1097 41. Lin ME, Chen T, Leaf EM, Speer MY, Giachelli CM. Runx2 Expression in Smooth
1098 Muscle Cells Is Required for Arterial Medial Calcification in Mice. *Am J Pathol*.
1099 2015;185:1958-1969. doi: 10.1016/j.ajpath.2015.03.020
1100 42. Parra-Izquierdo I, Castanos-Mollor I, Lopez J, Gomez C, San Roman JA, Sanchez
1101 Crespo M, Garcia-Rodriguez C. Calcification Induced by Type I Interferon in Human
1102 Aortic Valve Interstitial Cells Is Larger in Males and Blunted by a Janus Kinase Inhibitor.
1103 *Arterioscler Thromb Vasc Biol*. 2018;38:2148-2159. doi: 10.1161/ATVBAHA.118.311504
1104 43. Parra-Izquierdo I, Castanos-Mollor I, Lopez J, Gomez C, San Roman JA, Sanchez
1105 Crespo M, Garcia-Rodriguez C. Lipopolysaccharide and interferon-gamma team up to
1106 activate HIF-1alpha via STAT1 in normoxia and exhibit sex differences in human aortic
1107 valve interstitial cells. *Biochim Biophys Acta Mol Basis Dis*. 2019;1865:2168-2179. doi:
1108 10.1016/j.bbadis.2019.04.014
1109 44. Jin H, St Hilaire C, Huang Y, Yang D, Dmitrieva NI, Negro A, Schwartzbeck R, Liu Y, Yu
1110 Z, Walts A, et al. Increased activity of TNAP compensates for reduced adenosine
1111 production and promotes ectopic calcification in the genetic disease ACDC. *Sci Signal*.
1112 2016;9:ra121. doi: 10.1126/scisignal.aaf9109
1113 45. Moorhead WJ, 3rd, Chu CC, Cuevas RA, Callahan Jt, Wong R, Regan C, Boufford CK,
1114 Sur S, Liu M, Gomez D, et al. Dysregulation of FOXO1 (Forkhead Box O1 Protein)
1115 Drives Calcification in Arterial Calcification due to Deficiency of CD73 and Is Present in
1116 Peripheral Artery Disease. *Arterioscler Thromb Vasc Biol*. 2020;40:1680-1694. doi:
1117 10.1161/ATVBAHA.119.313765
1118 46. Jung JJ, Razavian M, Kim HY, Ye Y, Golestani R, Toczek J, Zhang J, Sadeghi MM.
1119 Matrix metalloproteinase inhibitor, doxycycline and progression of calcific aortic valve
1120 disease in hyperlipidemic mice. *Sci Rep*. 2016;6:32659. doi: 10.1038/srep32659
1121 47. Millan A, Lanzer P, Sorribas V. The Thermodynamics of Medial Vascular Calcification.
1122 *Front Cell Dev Biol*. 2021;9:633465. doi: 10.3389/fcell.2021.633465

1123 48. Kim NW, Piatyszek MA, Prowse KR, Harley CB, West MD, Ho PL, Coviello GM, Wright
1124 WE, Weinrich SL, Shay JW. Specific association of human telomerase activity with
1125 immortal cells and cancer. *Science*. 1994;266:2011-2015. doi: 10.1126/science.7605428
1126 49. Hao LY, Armanios M, Strong MA, Karim B, Feldser DM, Huso D, Greider CW. Short
1127 telomeres, even in the presence of telomerase, limit tissue renewal capacity. *Cell*.
1128 2005;123:1121-1131. doi: 10.1016/j.cell.2005.11.020
1129 50. Bu DX, Johansson ME, Ren J, Xu DW, Johnson FB, Edfeldt K, Yan ZQ. Nuclear factor
1130 kappaB-mediated transactivation of telomerase prevents intimal smooth muscle cell from
1131 replicative senescence during vascular repair. *Arterioscler Thromb Vasc Biol*.
1132 2010;30:2604-2610. doi: 10.1161/ATVBAHA.110.213074
1133 51. Yuan X, Larsson C, Xu D. Mechanisms underlying the activation of TERT transcription
1134 and telomerase activity in human cancer: old actors and new players. *Oncogene*.
1135 2019;38:6172-6183. doi: 10.1038/s41388-019-0872-9
1136 52. Wu KJ, Grandori C, Amacker M, Simon-Vermot N, Polack A, Lingner J, Dalla-Favera R.
1137 Direct activation of TERT transcription by c-MYC. *Nat Genet*. 1999;21:220-224. doi:
1138 10.1038/6010
1139 53. Lee J, Rhee MH, Kim E, Cho JY. BAY 11-7082 is a broad-spectrum inhibitor with anti-
1140 inflammatory activity against multiple targets. *Mediators Inflamm*. 2012;2012:416036.
1141 doi: 10.1155/2012/416036
1142 54. Pierce JW, Schoenleber R, Jesmok G, Best J, Moore SA, Collins T, Gerritsen ME. Novel
1143 inhibitors of cytokine-induced IkappaBalpha phosphorylation and endothelial cell
1144 adhesion molecule expression show anti-inflammatory effects in vivo. *J Biol Chem*.
1145 1997;272:21096-21103. doi: 10.1074/jbc.272.34.21096
1146 55. Jin HY, Weir-McCall JR, Leipsic JA, Son JW, Sellers SL, Shao M, Blanke P, Ahmadi A,
1147 Hadamitzky M, Kim YJ, et al. The Relationship Between Coronary Calcification and the
1148 Natural History of Coronary Artery Disease. *JACC Cardiovasc Imaging*. 2021;14:233-
1149 242. doi: 10.1016/j.jcmg.2020.08.036
1150 56. Ogawa D, Nomiyama T, Nakamachi T, Heywood EB, Stone JF, Berger JP, Law RE,
1151 Bruemmer D. Activation of peroxisome proliferator-activated receptor gamma
1152 suppresses telomerase activity in vascular smooth muscle cells. *Circ Res*. 2006;98:e50-
1153 59. doi: 10.1161/01.RES.0000218271.93076.c3
1154 57. Chiang YJ, Hemann MT, Hathcock KS, Tessarollo L, Feigenbaum L, Hahn WC, Hodes
1155 RJ. Expression of telomerase RNA template, but not telomerase reverse transcriptase,

1156 is limiting for telomere length maintenance in vivo. *Mol Cell Biol*. 2004;24:7024-7031.
1157 doi: 10.1128/MCB.24.16.7024-7031.2004
1158 58. Tani T, Orimo H, Shimizu A, Tsuruoka S. Development of a novel chronic kidney
1159 disease mouse model to evaluate the progression of hyperphosphatemia and associated
1160 mineral bone disease. *Sci Rep*. 2017;7:2233. doi: 10.1038/s41598-017-02351-6
1161 59. Feng J, Funk WD, Wang SS, Weinrich SL, Avilion AA, Chiu CP, Adams RR, Chang E,
1162 Allsopp RC, Yu J, et al. The RNA component of human telomerase. *Science*.
1163 1995;269:1236-1241. doi: 10.1126/science.7544491
1164 60. Roake CM, Artandi SE. Regulation of human telomerase in homeostasis and disease.
1165 *Nat Rev Mol Cell Biol*. 2020;21:384-397. doi: 10.1038/s41580-020-0234-z
1166 61. Pascolo E, Wenz C, Lingner J, Hauel N, Priepke H, Kauffmann I, Garin-Chesa P, Rettig
1167 WJ, Damm K, Schnapp A. Mechanism of human telomerase inhibition by BIBR1532, a
1168 synthetic, non-nucleosidic drug candidate. *J Biol Chem*. 2002;277:15566-15572. doi:
1169 10.1074/jbc.M201266200
1170 62. Ghosh A, Saginc G, Leow SC, Khattar E, Shin EM, Yan TD, Wong M, Zhang Z, Li G,
1171 Sung WK, et al. Telomerase directly regulates NF-kappaB-dependent transcription. *Nat*
1172 *Cell Biol*. 2012;14:1270-1281. doi: 10.1038/ncb2621
1173 63. Liu N, Ding D, Hao W, Yang F, Wu X, Wang M, Xu X, Ju Z, Liu JP, Song Z, et al. hTERT
1174 promotes tumor angiogenesis by activating VEGF via interactions with the Sp1
1175 transcription factor. *Nucleic Acids Res*. 2016;44:8693-8703. doi: 10.1093/nar/gkw549
1176 64. Lee C, Huang CH. LASAGNA: a novel algorithm for transcription factor binding site
1177 alignment. *BMC Bioinformatics*. 2013;14:108. doi: 10.1186/1471-2105-14-108
1178 65. Wingender E, Dietze P, Karas H, Knuppel R. TRANSFAC: a database on transcription
1179 factors and their DNA binding sites. *Nucleic Acids Res*. 1996;24:238-241. doi:
1180 10.1093/nar/24.1.238
1181 66. Babu AN, Meng X, Zou N, Yang X, Wang M, Song Y, Cleveland JC, Weyant M,
1182 Banerjee A, Fullerton DA. Lipopolysaccharide stimulation of human aortic valve
1183 interstitial cells activates inflammation and osteogenesis. *Ann Thorac Surg*. 2008;86:71-
1184 76. doi: 10.1016/j.athoracsur.2008.03.008
1185 67. Natarajan K, Muller-Klieser D, Rubner S, Berg T. Stafia-1: a STAT5a-Selective Inhibitor
1186 Developed via Docking-Based Screening of in Silico O-Phosphorylated Fragments.
1187 *Chemistry*. 2020;26:148-154. doi: 10.1002/chem.201904147

1188 68. Elumalai N, Berg A, Natarajan K, Scharow A, Berg T. Nanomolar inhibitors of the
1189 transcription factor STAT5b with high selectivity over STAT5a. *Angew Chem Int Ed Engl*.
1190 2015;54:4758-4763. doi: 10.1002/anie.201410672
1191 69. Fredriksson S, Gullberg M, Jarvius J, Olsson C, Pietras K, Gustafsdottir SM, Ostman A,
1192 Landegren U. Protein detection using proximity-dependent DNA ligation assays. *Nat*
1193 *Biotechnol*. 2002;20:473-477. doi: 10.1038/nbt0502-473
1194 70. Gillis AJ, Schuller AP, Skordalakes E. Structure of the Tribolium castaneum telomerase
1195 catalytic subunit TERT. *Nature*. 2008;455:633-637. doi: 10.1038/nature07283
1196 71. Neculai D, Neculai AM, Verrier S, Straub K, Klumpp K, Pfitzner E, Becker S. Structure of
1197 the unphosphorylated STAT5a dimer. *J Biol Chem*. 2005;280:40782-40787. doi:
1198 10.1074/jbc.M507682200
1199 72. Jumper J, Evans R, Pritzel A, Green T, Figurnov M, Ronneberger O, Tunyasuvunakool
1200 K, Bates R, Zidek A, Potapenko A, et al. Highly accurate protein structure prediction with
1201 AlphaFold. *Nature*. 2021;596:583-589. doi: 10.1038/s41586-021-03819-2
1202 73. Yan Y, Tao H, He J, Huang SY. The HDOCK server for integrated protein-protein
1203 docking. *Nat Protoc*. 2020;15:1829-1852. doi: 10.1038/s41596-020-0312-x
1204 74. Tebo AG, Gautier A. A split fluorescent reporter with rapid and reversible
1205 complementation. *Nat Commun*. 2019;10:2822. doi: 10.1038/s41467-019-10855-0
1206 75. Liu JC, Lengner CJ, Gaur T, Lou Y, Hussain S, Jones MD, Borodic B, Colby JL,
1207 Steinman HA, van Wijnen AJ, et al. Runx2 protein expression utilizes the Runx2 P1
1208 promoter to establish osteoprogenitor cell number for normal bone formation. *J Biol*
1209 *Chem*. 2011;286:30057-30070. doi: 10.1074/jbc.M111.241505
1210 76. Stock M, Otto F. Control of RUNX2 isoform expression: the role of promoters and
1211 enhancers. *J Cell Biochem*. 2005;95:506-517. doi: 10.1002/jcb.20471
1212 77. Zhang S, Xiao Z, Luo J, He N, Mahlios J, Quarles LD. Dose-dependent effects of Runx2
1213 on bone development. *J Bone Miner Res*. 2009;24:1889-1904. doi: 10.1359/jbmr.090502
1214 78. Okura H, Sato S, Kishikawa S, Kaneto S, Nakashima T, Yoshida N, Takayanagi H,
1215 Kiyono H. Runx2-I isoform contributes to fetal bone formation even in the absence of
1216 specific N-terminal amino acids. *PLoS One*. 2014;9:e108294. doi:
1217 10.1371/journal.pone.0108294
1218 79. Banerjee C, Javed A, Choi JY, Green J, Rosen V, van Wijnen AJ, Stein JL, Lian JB,
1219 Stein GS. Differential regulation of the two principal Runx2/Cbfa1 n-terminal isoforms in

1220 response to bone morphogenetic protein-2 during development of the osteoblast
1221 phenotype. *Endocrinology*. 2001;142:4026-4039. doi: 10.1210/endo.142.9.8367
1222 80. Maida Y, Yasukawa M, Okamoto N, Ohka S, Kinoshita K, Totoki Y, Ito TK, Minamino T,
1223 Nakamura H, Yamaguchi S, et al. Involvement of telomerase reverse transcriptase in
1224 heterochromatin maintenance. *Mol Cell Biol*. 2014;34:1576-1593. doi:
1225 10.1128/MCB.00093-14
1226 81. Okamoto N, Yasukawa M, Nguyen C, Kasim V, Maida Y, Possemato R, Shibata T, Ligon
1227 KL, Fukami K, Hahn WC, et al. Maintenance of tumor initiating cells of defined genetic
1228 composition by nucleostemin. *Proc Natl Acad Sci U S A*. 2011;108:20388-20393. doi:
1229 10.1073/pnas.1015171108
1230 82. Gizard F, Nomiyama T, Zhao Y, Findeisen HM, Heywood EB, Jones KL, Staels B,
1231 Bruemmer D. The PPARalpha/p16INK4a pathway inhibits vascular smooth muscle cell
1232 proliferation by repressing cell cycle-dependent telomerase activation. *Circ Res*.
1233 2008;103:1155-1163. doi: 10.1161/CIRCRESAHA.108.186205
1234 83. Yutzey KE, Demer LL, Body SC, Huggins GS, Towler DA, Giachelli CM, Hofmann-
1235 Bowman MA, Mortlock DP, Rogers MB, Sadeghi MM, et al. Calcific aortic valve disease:
1236 a consensus summary from the Alliance of Investigators on Calcific Aortic Valve
1237 Disease. *Arterioscler Thromb Vasc Biol*. 2014;34:2387-2393. doi:
1238 10.1161/ATVBAHA.114.302523
1239 84. Hoerstrup SP, Kadner A, Melnitchouk S, Trojan A, Eid K, Tracy J, Sodian R, Visjager JF,
1240 Kolb SA, Grunenfelder J, et al. Tissue engineering of functional trileaflet heart valves
1241 from human marrow stromal cells. *Circulation*. 2002;106:I143-150.
1242 85. Hortells L, Sur S, St Hilaire C. Cell Phenotype Transitions in Cardiovascular
1243 Calcification. *Front Cardiovasc Med*. 2018;5:27. doi: 10.3389/fcvm.2018.00027
1244 86. Bogdanova M, Zabirnyk A, Malashicheva A, Enayati KZ, Karlsen TA, Kaljusto ML,
1245 Kvitting JP, Dissen E, Sullivan GJ, Kostareva A, et al. Interstitial cells in calcified aortic
1246 valves have reduced differentiation potential and stem cell-like properties. *Sci Rep*.
1247 2019;9:12934. doi: 10.1038/s41598-019-49016-0
1248 87. Xu K, Xie S, Huang Y, Zhou T, Liu M, Zhu P, Wang C, Shi J, Li F, Sellke FW, et al. Cell-
1249 Type Transcriptome Atlas of Human Aortic Valves Reveal Cell Heterogeneity and
1250 Endothelial to Mesenchymal Transition Involved in Calcific Aortic Valve Disease.
1251 *Arterioscler Thromb Vasc Biol*. 2020;40:2910-2921. doi: 10.1161/ATVBAHA.120.314789

1252 88. Lindroos M, Kupari M, Heikkila J, Tilvis R. Prevalence of aortic valve abnormalities in the
1253 elderly: an echocardiographic study of a random population sample. *J Am Coll Cardiol*.
1254 1993;21:1220-1225. doi: 10.1016/0735-1097(93)90249-z
1255 89. Joung YH, Lim EJ, Darvin P, Chung SC, Jang JW, Do Park K, Lee HK, Kim HS, Park T,
1256 Yang YM. MSM enhances GH signaling via the Jak2/STAT5b pathway in osteoblast-like
1257 cells and osteoblast differentiation through the activation of STAT5b in MSCs. *PLoS*
1258 *One*. 2012;7:e47477. doi: 10.1371/journal.pone.0047477
1259 90. Lee KM, Park KH, Hwang JS, Lee M, Yoon DS, Ryu HA, Jung HS, Park KW, Kim J,
1260 Park SW, et al. Inhibition of STAT5A promotes osteogenesis by DLX5 regulation. *Cell*
1261 *Death Dis*. 2018;9:1136. doi: 10.1038/s41419-018-1184-7
1262 91. Paulson M, Pisharody S, Pan L, Guadagno S, Mui AL, Levy DE. Stat protein
1263 transactivation domains recruit p300/CBP through widely divergent sequences. *J Biol*
1264 *Chem*. 1999;274:25343-25349. doi: 10.1074/jbc.274.36.25343
1265 92. Martino A, Holmes JHt, Lord JD, Moon JJ, Nelson BH. Stat5 and Sp1 regulate
1266 transcription of the cyclin D2 gene in response to IL-2. *J Immunol*. 2001;166:1723-1729.
1267 doi: 10.4049/jimmunol.166.3.1723
1268 93. Bergad PL, Towle HC, Berry SA. Yin-yang 1 and glucocorticoid receptor participate in
1269 the Stat5-mediated growth hormone response of the serine protease inhibitor 2.1 gene.
1270 *J Biol Chem*. 2000;275:8114-8120. doi: 10.1074/jbc.275.11.8114
1271 94. Yamada O, Ozaki K, Furukawa T, Machida M, Wang YH, Motoji T, Mitsuishi T, Akiyama
1272 M, Yamada H, Kawauchi K, et al. Activation of STAT5 confers imatinib resistance on
1273 leukemic cells through the transcription of TERT and MDR1. *Cell Signal*. 2011;23:1119-
1274 1127. doi: 10.1016/j.cellsig.2011.02.005
1275 95. Yamada O, Ozaki K, Akiyama M, Kawauchi K. JAK-STAT and JAK-PI3K-mTORC1
1276 pathways regulate telomerase transcriptionally and posttranslationally in ATL cells. *Mol*
1277 *Cancer Ther*. 2012;11:1112-1121. doi: 10.1158/1535-7163.MCT-11-0850
1278 96. Tormo AJ, Letellier MC, Sharma M, Elson G, Crabe S, Gauchat JF. IL-6 activates
1279 STAT5 in T cells. *Cytokine*. 2012;60:575-582. doi: 10.1016/j.cyto.2012.07.002
1280 97. Tanabe Y, Nishibori T, Su L, Arduini RM, Baker DP, David M. Cutting edge: role of
1281 STAT1, STAT3, and STAT5 in IFN-alpha beta responses in T lymphocytes. *J Immunol*.
1282 2005;174:609-613. doi: 10.4049/jimmunol.174.2.609
1283 98. Honda S, Miyamoto T, Watanabe T, Narumi T, Kadowaki S, Honda Y, Otaki Y,
1284 Hasegawa H, Netsu S, Funayama A, et al. A novel mouse model of aortic valve stenosis

1285 induced by direct wire injury. *Arterioscler Thromb Vasc Biol*. 2014;34:270-278. doi:
1286 10.1161/ATVBAHA.113.302610
1287 99. Sider KL, Blaser MC, Simmons CA. Animal models of calcific aortic valve disease. *Int J*
1288 *Inflam*. 2011;2011:364310. doi: 10.4061/2011/364310
1289 100. Balani K, Brito FC, Kos L, Agarwal A. Melanocyte pigmentation stiffens murine cardiac
1290 tricuspid valve leaflet. *J R Soc Interface*. 2009;6:1097-1102. doi: 10.1098/rsif.2009.0174
1291 101. Carneiro F, Kruithof BP, Balani K, Agarwal A, Gaussin V, Kos L. Relationships between
1292 melanocytes, mechanical properties and extracellular matrix composition in mouse heart
1293 valves. *J Long Term Eff Med Implants*. 2015;25:17-26. doi:
1294 10.1615/jlongtermeffmedimplants.2015011748
1295 102. Mjaatvedt CH, Kern CB, Norris RA, Fairey S, Cave CL. Normal distribution of
1296 melanocytes in the mouse heart. *Anat Rec A Discov Mol Cell Evol Biol*. 2005;285:748-
1297 757. doi: 10.1002/ar.a.20210
1298 103. Dharmarajan S, Speer MY, Pierce K, Lally J, Leaf EM, Lin ME, Scatena M, Giachelli CM.
1299 Role of Runx2 in Calcific Aortic Valve Disease in Mouse Models. *Front Cardiovasc Med*.
1300 2021;8:687210. doi: 10.3389/fcvm.2021.687210
1301 104. Lanzer P, Hannan FM, Lanzer JD, Janzen J, Raggi P, Furniss D, Schuchardt M,
1302 Thakker R, Fok PW, Saez-Rodriguez J, et al. Medial Arterial Calcification: JACC State-
1303 of-the-Art Review. *J Am Coll Cardiol*. 2021;78:1145-1165. doi:
1304 10.1016/j.jacc.2021.06.049
1305

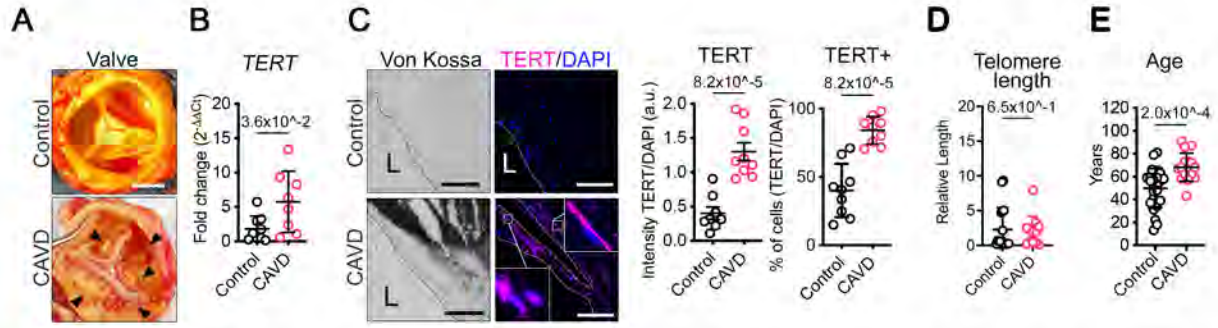

Figure 1. TERT is elevated in CAVD tissues. (**A**) Examples of non-calcified control (top) and calcified CAVD (bottom) human valves used in this study. Arrowheads indicate calcified nodules Scalebar. 1 cm. (**B**), *TERT* mRNA transcript quantification in control and CAVD valve tissues. n = 8 control, n= 9 CAVD. (**C**), Representative serial sections of Von Kossa (dark precipitation) and TERT immunofluorescent staining in control and CAVD valve tissues. Scalebar 100 µm. Graphs show the quantification of TERT intensity and the number of TERT-positive cells. n = 9 control, n = 9 CAVD. (**D**), Telomere length measurements in valve tissues. n = 19 control, n = 12 CAVD. (**E**), Age of the patients utilized in this study. n = 25 control, n = 16 CAVD. Data are shown as means ± SD. P values were calculated using the Mann-Whitney U test and shown on each graph. L = lumen.

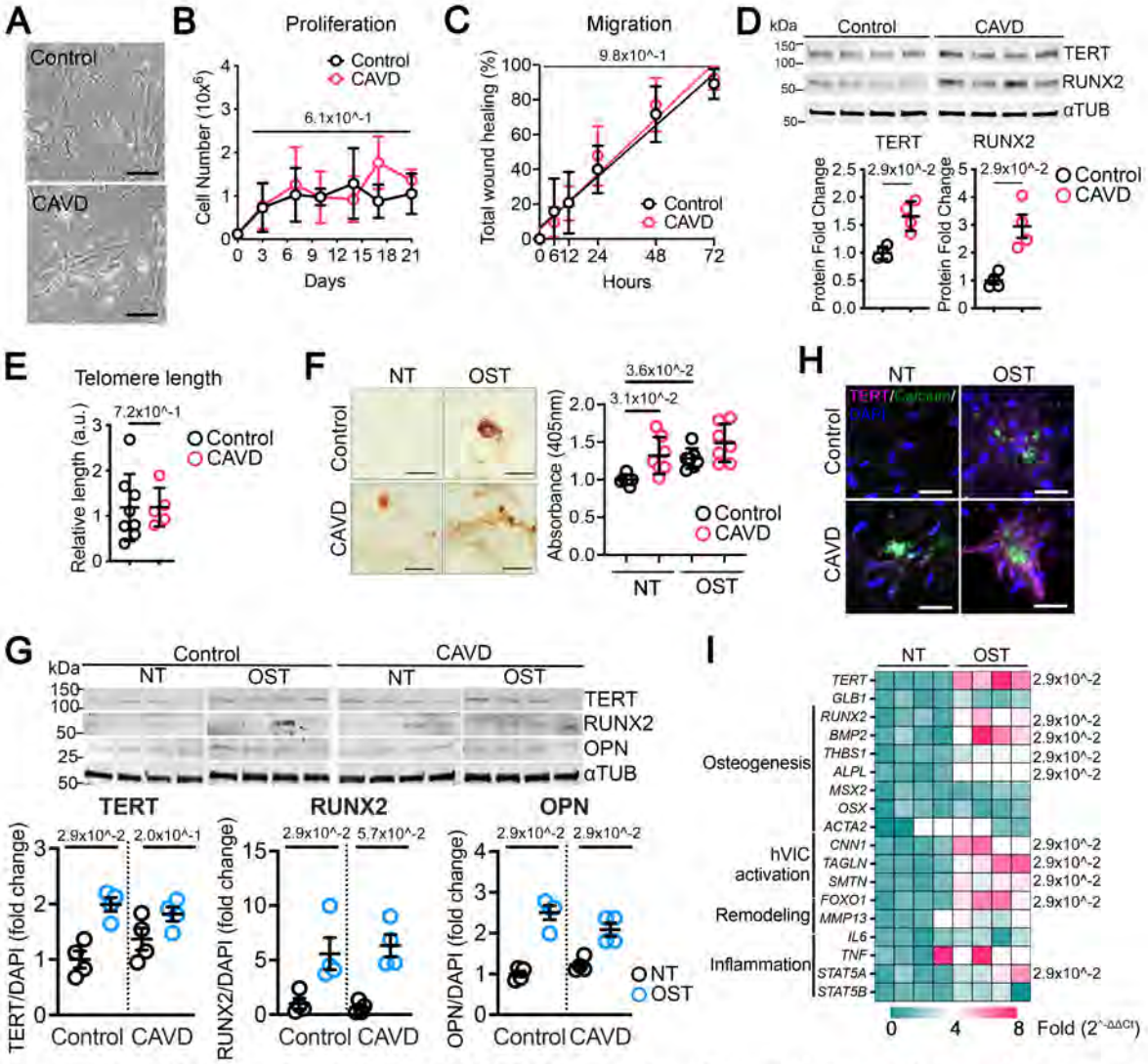

Figure 2. TERT is elevated in CAVD hVICs at baseline and upregulation during osteogenic reprogramming. (**A**), Representative images showing cell morphology of control and CAVD hVICs. Scalebar 50 µm. (**B**), Proliferation of control and CAVD hVICs at baseline. n = 3 both groups. (**C**) Relative migration distances of control and CAVD VICs. n = 10 both groups. (**D**) Western blot staining of control and CAVD hVICs at baseline. Quantification of protein levels is shown on the right panels. n = 4 both groups. (**E**) Telomere length measurements in VICs. n = 8, control, n = 5 CAVD. (**F**) Representative images of early calcification in hVICs growing in normal conditions (no treatment NT) or stimulated with osteogenic media (OST) for 14 days. Calcium deposition was visualized by Alizarin Red staining. Scalebar 50 µm. Quantification of calcification on the right graphs. n = 7 both groups. (**G**), Western blot staining of samples from control and CAVD hVICs after 14 days of NT or OST. Quantification of protein levels is shown on the bottom graphs. n = 4 both groups. (**H**), Representative immunofluorescent staining images of TERT in control and CAVD hVICs after 14 days of NT or OST. Calcium deposition was visualized with OsteoImage. Scalebar 100 µm. (**I**) Expression profile control VICs after 14 days of NT and OST treatment. n = 4 both groups. Data are shown as means ± SD. P values were calculated with the Mann-Whitney U test (Figures B, C, D, E, G, and I), and the Kruskal-Wallis H test with Dunn post hoc test (Figure F) and shown on each graph.

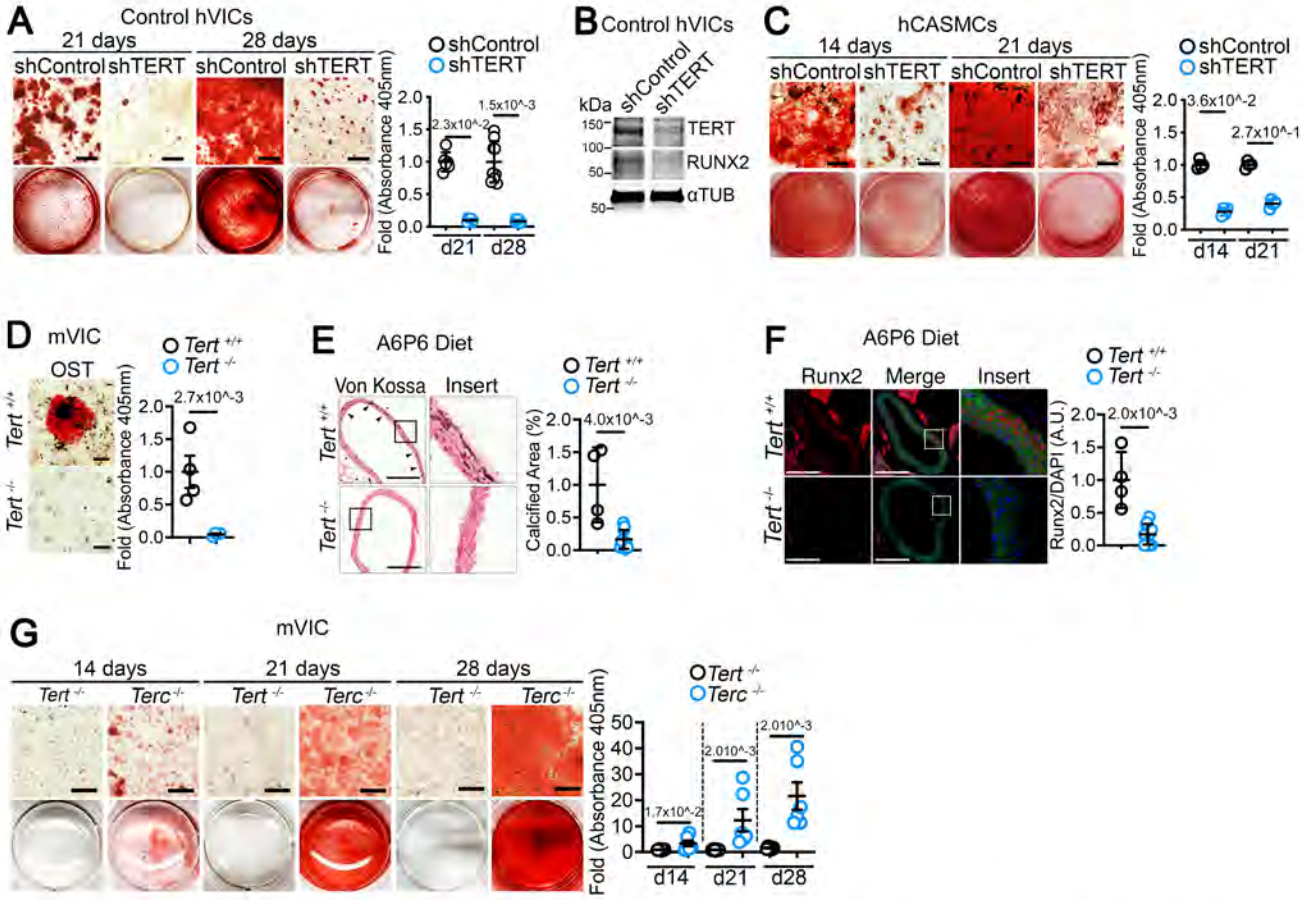

Figure 3. TERT is required to initiate the osteogenic transition and calcify human VICs. (**A**) Control hVICs were transduced lentivirus containing shControl or shTERT and followed by OST stimulation for up to 28 days. Calcium deposition was visualized by Alizarin Red staining. n = 6 shControl, n = 6 shTERT at 21 days and n = 9 each group at day 28. Scalebar 400 μm. (**B**) Representative western blot staining of control hVICs transduced with lentivirus containing either shControl or shTERT followed by 7 days of OST. (**C**) hCASMCs were transduced with shControl or shTERT and stimulated with OST for 14 and 21 days. n = 4 for each group at both time points. Scalebar 400 μm. (**D**) Representative images of mVIC isolated from *Tert*$^{+/+}$ and *Tert*$^{-/-}$ mice were stimulated with OST for 28 days. Scalebar 400 μm. (**E**) Representative Von Kossa staining images of *Tert*$^{+/+}$ and *Tert*$^{-/-}$ mice aortas (dark precipitation). Scale bar 400 μm. Quantification of calcification is shown on the right panel. (**F**) Representative immunofluorescent images of Runx2 expression indicative of calcification (red, insert) on *Tert*$^{+/+}$ and *Tert*$^{-/-}$ mice aorta. Scale bar 400 μm. Runx2 quantification of calcification is shown on the right panel. (**G**) Representative images of mVICs isolated from F1 *Tert*$^{-/-}$ or *Terc*$^{-/-}$ mice were stimulated with OST for up to 21 days. Scalebar 100 μm. Data are shown as means ± SD. P values were calculated using the Kruskal-Wallis H test, Dunn post hoc test (Figures A, C, and G), and Mann-Whitney U test (Figures D, E, and F).

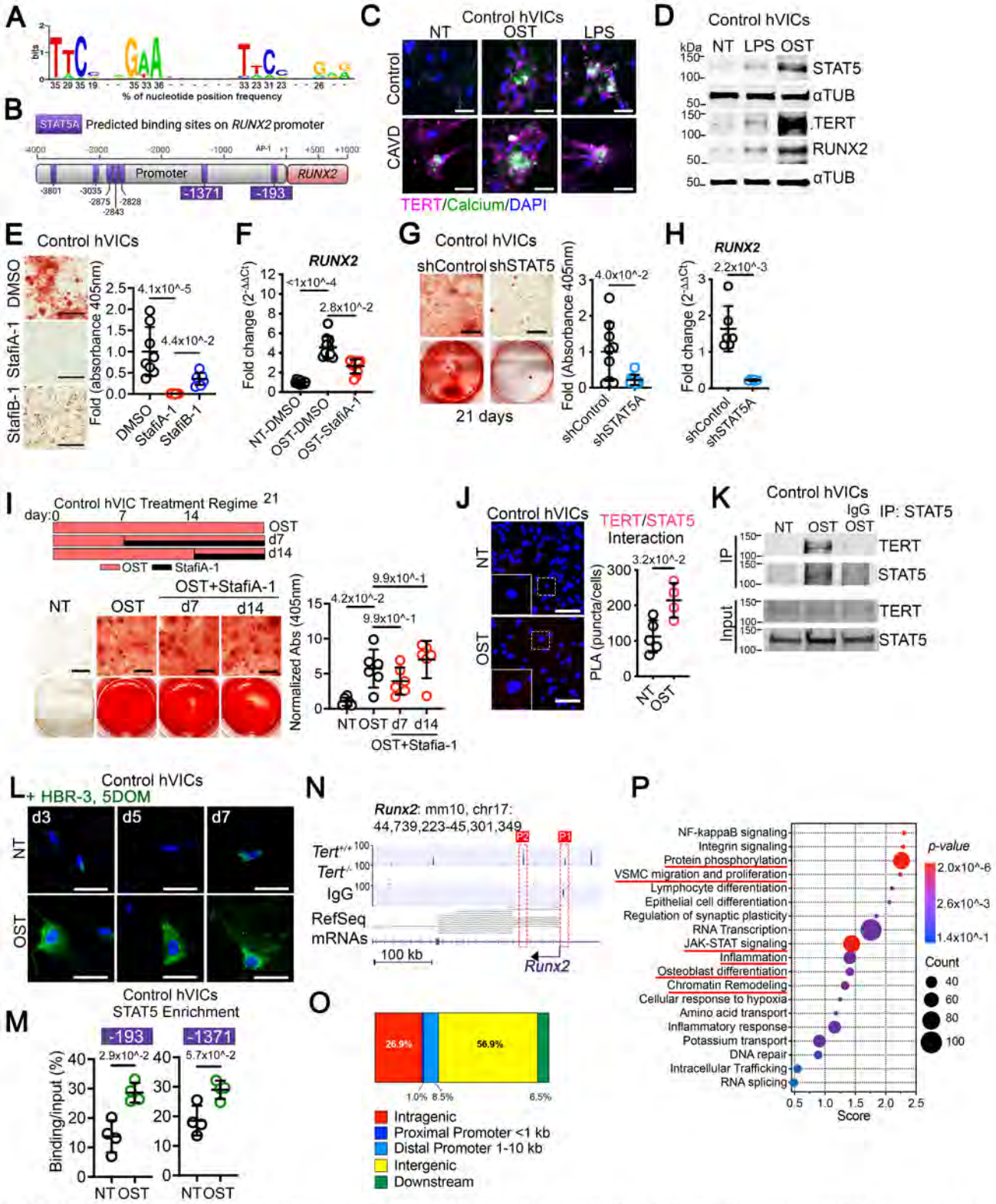

Figure 4. STAT5 binds to TERT and is required for the calcification of human VICs. (**A**) Graphic of in silico analysis identifying the consensus binding site for STAT5. (**B**), Diagram depicting STAT5 binding to RUNX2 promoter and the positions of the predicted STAT5 binding sites (purple boxes). (**C**) Representative immunofluorescence images of control hVICs after 14 days of LPS treatment or OST stimulation. Scalebar 50 μm. (**D**) Representative western blot staining of hVICs after 14 days of OST stimulation. (**E**) Representative images of control hVICs treated with 10 μM of the STAT5 inhibitors StafiA-1 or StafiB-1 throughout 28 days of osteogenic stimulation. Scalebar 400 μm. n = 8 each group. The quantification of calcification is shown on the right graph. (**F**) *RUNX2* mRNA transcript quantification at d7 OST, n = 10. (**G**) Control hVICs were transduced with lentivirus containing shControl or shSTAT5 constructs and treated with OST for 21 days. Calcium deposition was visualized by Alizarin Red staining. n = 9 for each group. Scalebar 400 μ m. (**H**) *RUNX2* mRNA transcript quantification at d7 OST, n = 6. (**I**) Schematic of OST treatment with delayed shTERT transduction (top panel).Representative images of hVIC (left panels) treated with 10 μM of the STAT5 inhibitors StafiA-1 at d7 or d14 of OST treatment. Samples were collected at d21 (bottom panel). Scalebar 400 μm. n = 6 for each group. (**J**) Representative images of TERT/STAT5 complex (red foci) in control hVICs cultured for 21 days in osteogenic medium and detected by PLA. Scalebar 100 μm. n = 4 for each group. (**K**) STAT5 co-immunoprecipitation in control hVICs under OST for 10 days to detect TERT/STAT5 interaction. (**L**) Control hVIC co-expressing TERT-NFAST and STAT5A-CFAST were labeled with 5 μM HBR-3,5DOM (4-hydroxy-3,5- dimethoxybenzylidene rhodamine, coral) and imaged at d3, d5, and d7 of osteogenic treatment (OST) or control no-treatment (NT). Scale bars 50 μm. (**M**) Chromatin immunoprecipitation shows enrichment of STAT5 on RUNX2 promoter OST conditions compared to NT. The base position is indicated in the blue boxes. n=4 for each group as in B. (**N**) STAT5 CUT&Tag sequencing tracks in genomic regions of Runx2 in no-treatment control and osteogenic condition-treated mice VICs. (**O**) Stacked chart representing genome-wide STAT5 occupancy in promoters, genes, and intergenic regions frequency in mice VICs. (**P**) Top 20 GO pathways enriched in genes with significant loss of STAT5 in *Tert*$^{+/+}$ vs *Tert*$^{-/-}$ mice VICs. Data are shown as means ± SD. P values were calculated by the Mann-Whitney U test (Figures F, H, and J) and the Kruskal-Wallis H test (Figures E and G) and indicated on top of each graph.

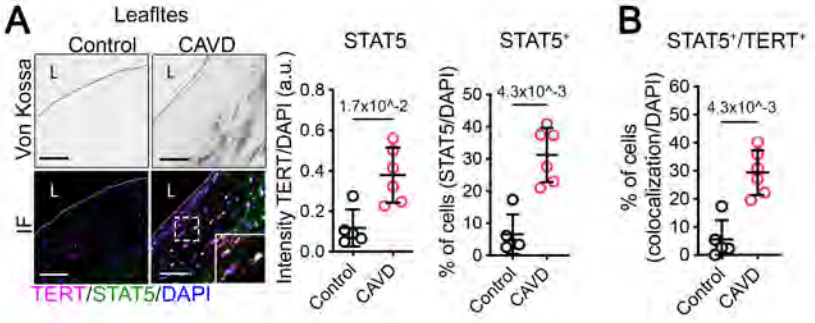

Figure 5. TERT and STAT5 are upregulated and colocalized in CAVD tissue. (**A**) Representative serial sections of Von Kossa (dark precipitation) and TERT and STAT5 immunofluorescent staining in control and CAVD tissues. Scalebar 100 µm. STAT5 intensity and STAT5-positive cells (STAT5+) are quantified on the right panels. (**B**) Quantification of STAT5-TERT-positive cells. Data are shown as means ± SD, n = 5 control, n = 6 CAVD. P values were calculated with the Mann-Whitney U test and indicated on each graph. L = lumen.

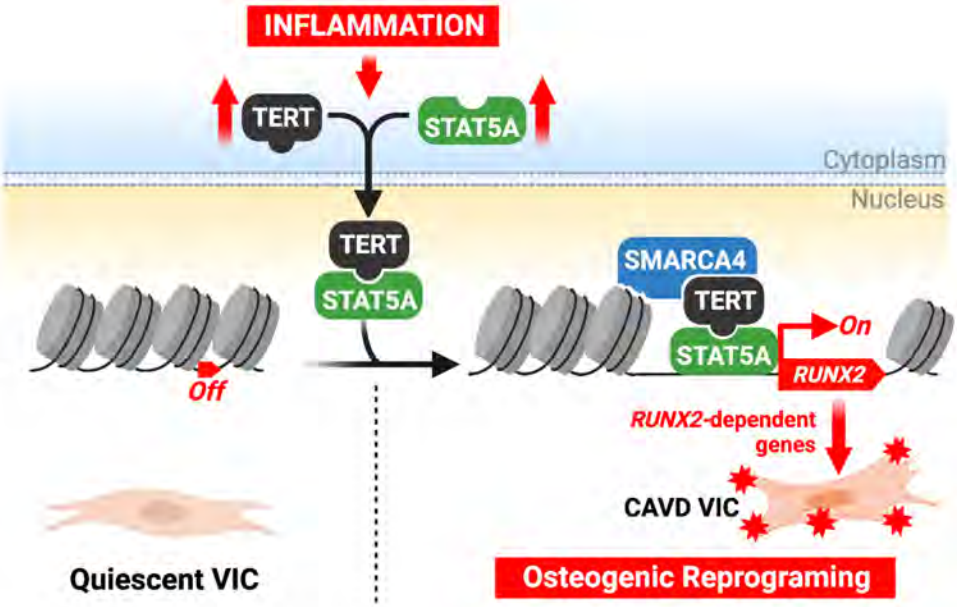

Figure 6. TERT/STAT5 promotes osteogenic reprogramming. Inflammatory signals promote the upregulation and interaction of TERT and STAT5A. The TERT/STAT5 complex translocates into the nucleus, where TERT interacts with SMARCA4 (also known as BRG1), which facilitates a permissive chromatin configuration, and STAT5A binds specific sites on the RUNX2 promoter, leading to the osteogenic reprogramming of valve interstitial cells during the early stages of CAVD pathogenesis.

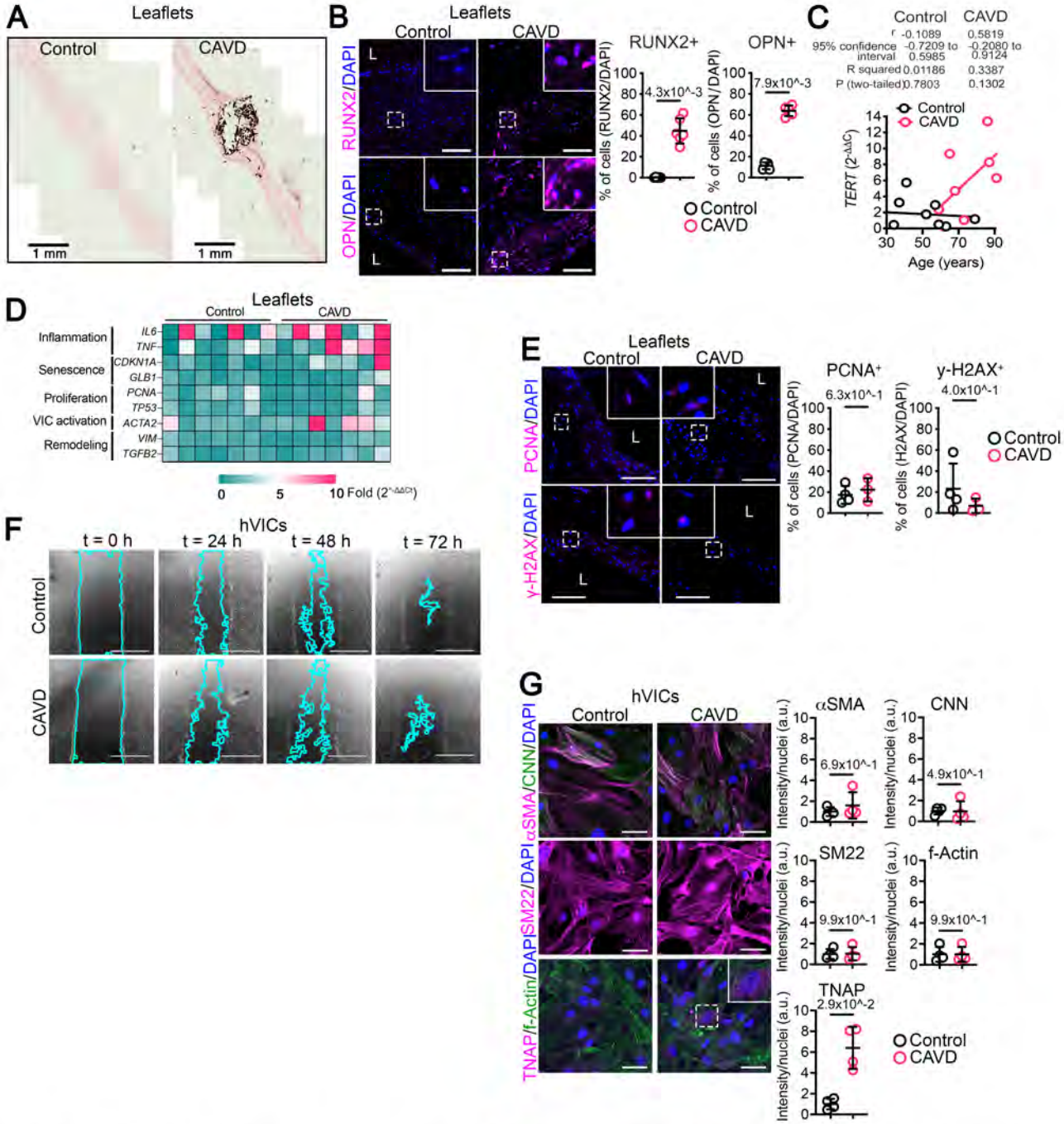

Supplemental Figure 1. Characterization of human CAVD valves and patient-isolated VICs. (**A**) Representative section of Von Kossa staining in control and valve CAVD leaflets tissue. Scalebar 1 mm. (**B**) Representative serial sections of RUNX2 immunofluorescent staining and OPN in control and CAVD valve tissues. Scalebar 100 µm. Quantification of RUNX2-positive cells and OPN-positive cells on the leaflet specimen is shown on the right graphs. n = 5 control, n = 6 CAVD. (**C**) Correlation between age of the donor and TERT expression in valve tissues. n = 8 control, n = 9 CAVD. (**D**) Gene expression profile in the valve leaflets. n = 7 each group. (**E**) Representative images of immunofluorescent staining of PCNA (top panels) and γ-H2AX (bottom panels) in control and CAVD valve tissues. Scalebar 100 µm. Quantification of PCNA-positive cells and γ-H2AX-positive cells are shown on the right graphs. n = 4 control, n = 3 CAVD. (**F**) Representative images of a scratch assay in control and CAVD hVICs. Time points are indicated on top of each panel. Blue lines denote the cell migration front. Scalebar 1 mm. n = 10 of each group. (**G**) Representative images of αSMA, CNN, SM22, TNAP, and f-Actin in control and CAVD hVICs. Scalebar 50 µm. Signal quantification is shown on the right. n = 4 each group. Data are shown as means ± SD. P values were calculated using the Mann-Whitney U test (Figures B, D, E, and G) and the Pearson correlation test (Figure C). L = lumen.

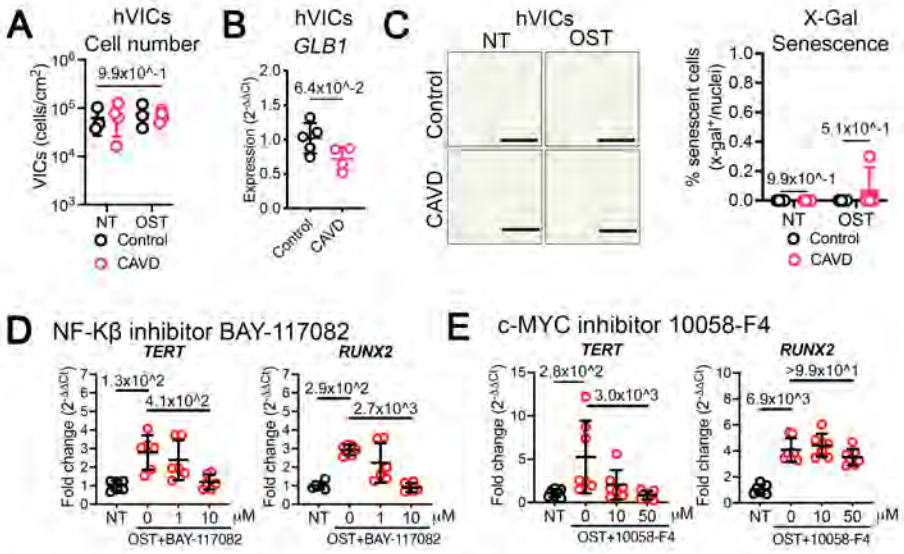

Supplemental Figure 2. Inhibition of reverse transcriptase activity of TERT does not prevent osteogenic reprogramming of hVICs. (**A**) Cell counts of control and CAVD hVICs after 14 days of NT or OST stimulation. n = 4 each group. (**B**) β-galactosidase (BLG1) mRNA transcript quantification in control and CAVD hVICs at baseline. n = 5 control, n= 4 CAVD. (**C**) Representative images of senescence-associated β-galactosidase activity staining of hVICs after 28 days of NT or OST stimulation. Blue cells were considered positive for senescence. Quantification of senescence is shown on the right graph. n = 4 each group. Scalebar 400 μm. (**D**) hVICs growing in no treatment (NT), OST media, or OST media supplemented with the NF-Kβ inhibitor BAY-117082 for 7 days, n = 6. (**E**) hVICs growing in no treatment (NT), OST media, or OST media supplemented with the c-MYC inhibitor 10058-F4 for 7 days, n = 7. qRT-PCR quantified TERT and RUNX2 gene expression. In D and E, inhibitors were dissolved in DMSO thus NT and OST were supplemented with the highest volume of vehicle (DMSO) used in treatment groups. Data are shown as means ± SD. P values were calculated with the Mann-Whitney U test (Figure B) and the Kruskal-Wallis H test with Dunn pairwise comparison post hoc test (Figures A, C-E) and shown on top of each graph.

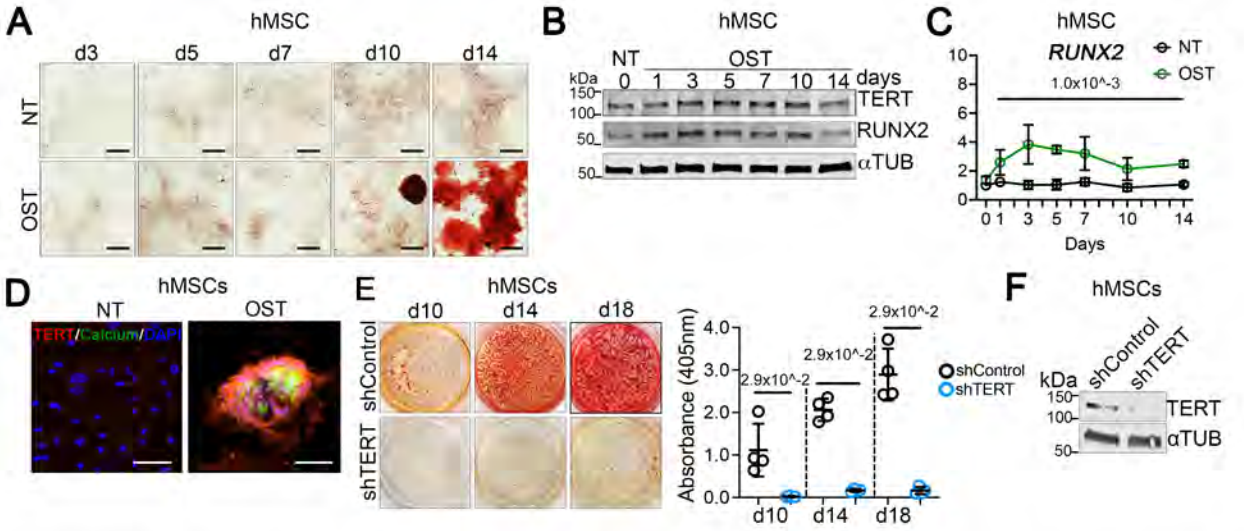

Supplemental Figure 3. TERT is upregulated and required for the osteogenic differentiation of human mesenchymal stem cells. (**A**) Representative images of hMSCs stimulated with OST for 14 days. Calcium deposition was visualized by Alizarin Red staining. Scalebar 50 µm. (**B**) Western blot staining of samples from hMSCs collected during the 14 days of OST treatment. (**C**) *RUNX2* expression profile of differentiating hMSCs stimulated for 14 days with OST media. n = 3. (**D**) Representative TERT immunofluorescent staining images of hMSCs stimulated with OST for 14 days. Scalebar 100 µm. (**E**) Representative images of hMSCs infected with shTERT or shControl virus and stimulated with OST for 14 days. Calcium deposition was visualized by Alizarin Red staining. The quantification of calcification is shown on the right graph. n = 3. (**F**) Western blot staining of samples from hMSCs collected during the 14 days of OST treatment. Data are shown as means ± SD. P values were calculated with the Kruskal-Wallis H test with Dunn pairwise comparison post hoc test (Figure C) and the Mann-Whitney U test (Figure E) and shown on each graph.

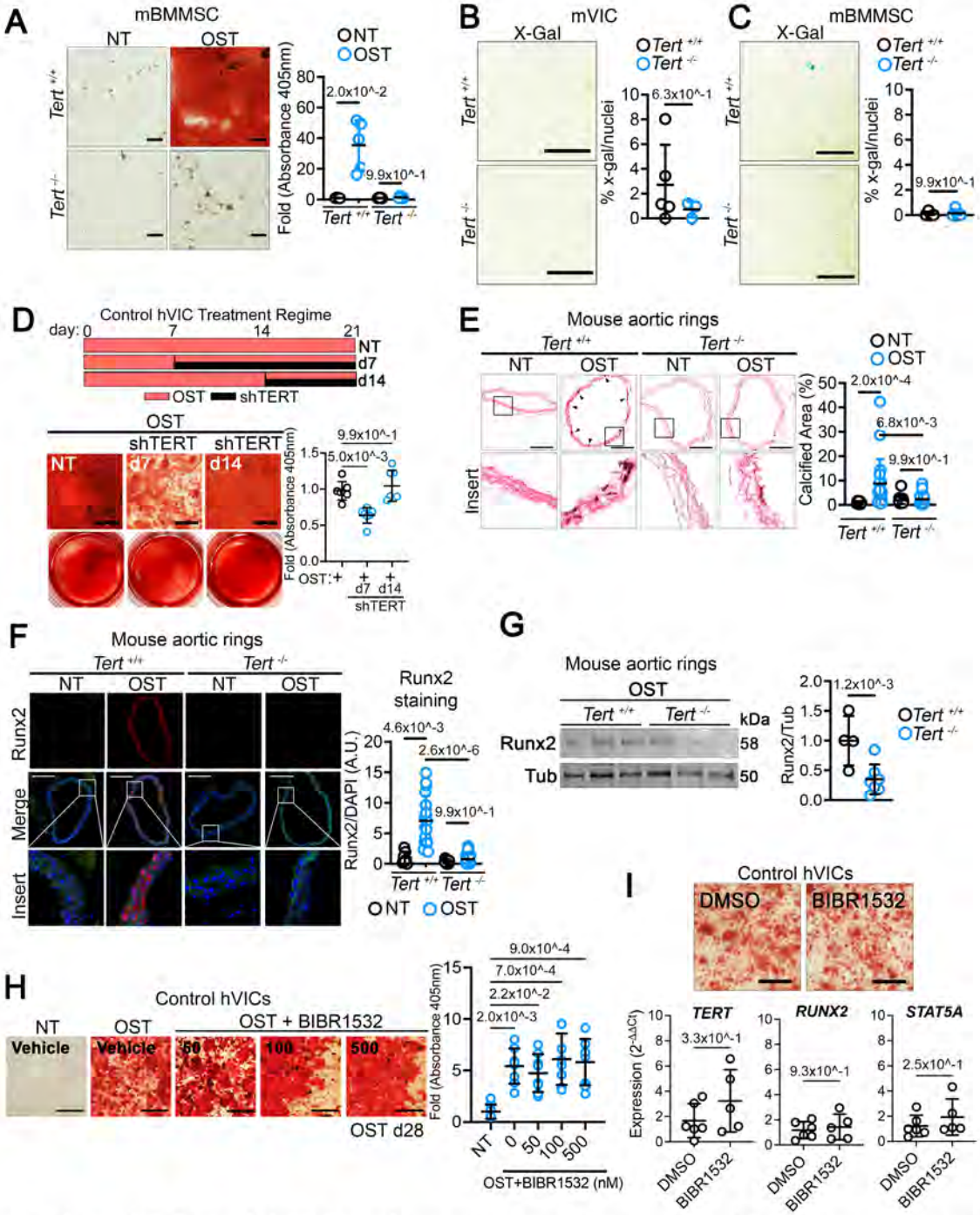

Supplemental Figure 4. Inhibition of reverse transcriptase activity of TERT does not prevent osteogenic reprogramming of VICs. (**A**) Representative images of mBMMSCs isolated from *Tert*$^{+/+}$ or *Tert*$^{-/-}$ mice and stimulated with OST for 21 days. Scalebar 100 µm. Quantification of calcification is presented as average absorbance on the right graphs, n = 5 for each group. (**B, C**) Representative images of a senescence-associated β-galactosidase (SA-β-gal) staining of mVICs and mBMMSCs isolated from *Tert*$^{+/+}$ or F1 *Tert*$^{-/-}$ mice after 21 days of OST stimulation. In each group, blue cells were considered positive for senescence, n = 5. (**D**) Schematic of OST treatment with delayed shTERT transduction (top panel). VICs were transduced with shTERT, and calcification was assessed with Alizarin Red S stain at day 21. Scalebar 400 µm. n = 6 for each group. (**E**) Representative sections of Von Kossa staining in thoracic aortic rings isolated from *Tert*$^{+/+}$ and *Tert*$^{-/-}$ mice after 14 days of OST treatment relative to NT control treatment. Quantification is shown on the right. Scale bar 400 µm (**F**) Immunofluorescence staining of thoracic aortic rings after OST treatment as in B. Quantification of Runx2 is shown on the right graph. Scale bar 400 µm (**G**) Western blot staining of aortic ring specimens collected and treated in B. Quantification of Runx2 is shown on the right graph. (**H**) Human VICs were treated with the TERT inhibitor BiBR1532 and stimulated with OST, and calcification was assessed on day 28, with n = 5 in each group. (**I**) *TERT*, *RUNX2*, and *STAT5A* expression were evaluated on day 14, n = 6 DMSO, n = 5 BIBR1532. Data are shown as means ± SD. P values were calculated with the Kruskal-Wallis H test with Dunn pairwise comparison post hoc test (Figures A, B, C, E, H) and the Mann-Whitney U test (Figures D, F, G, I) and are shown on top of each graph.

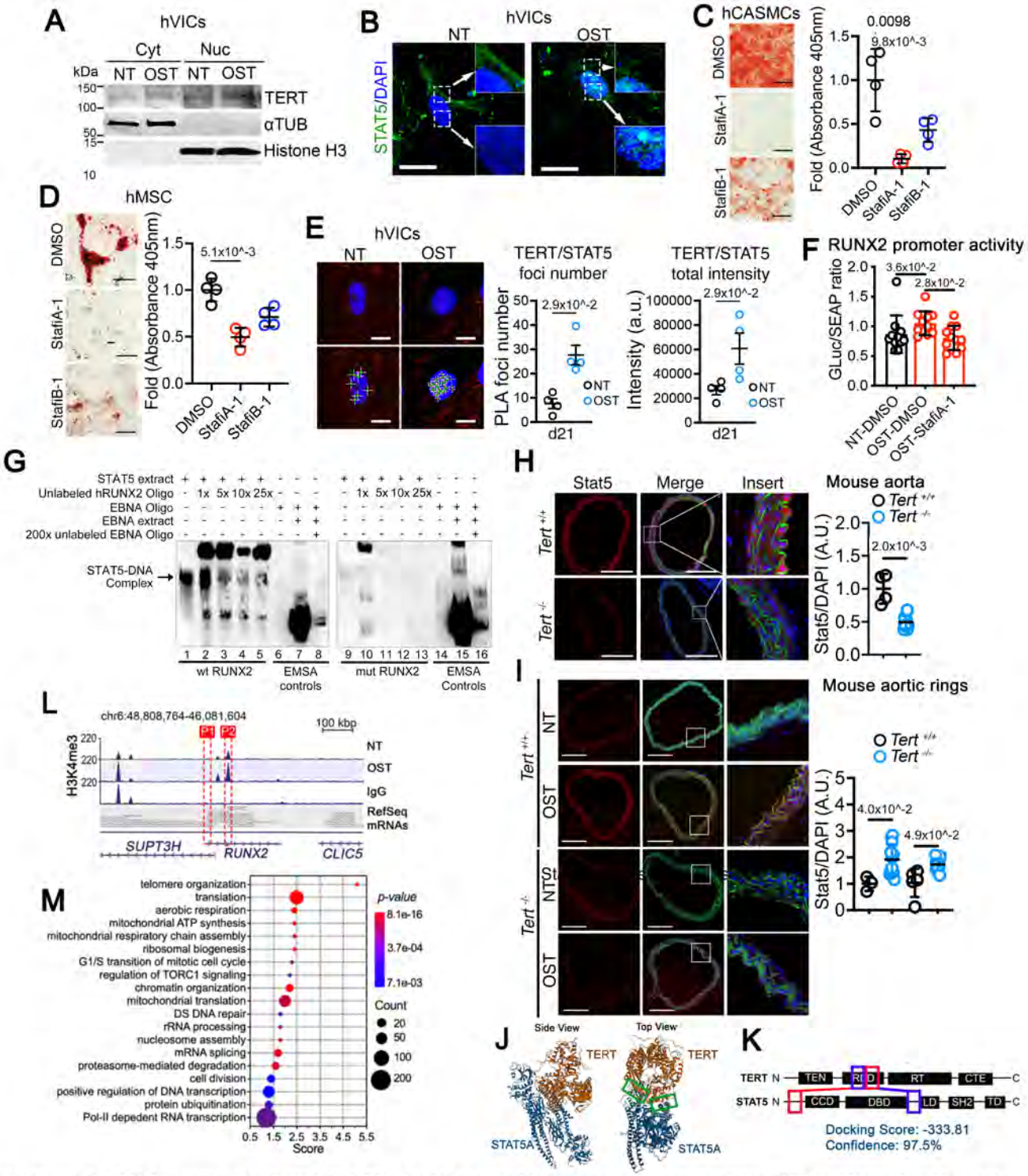

Supplemental Figure 5. STAT5 is upregulated, binds to TERT, and is required for osteogenic reprogramming of VICs. (A) Western blot analysis of cytoplasmic and nuclear fractions of TERT from control VICs obtained after seven days of OST stimulation. TUB, (tubuline); H3, (Histone H3); Cyt, cytoplasmic fraction; Nuc, nuclear fraction. (B) Representative immunofluorescence image of STAT5 subcellular distribution after 14 days of NT and OST stimulation. Scalebar 40 μm. (C) Representative images of human CASMCs treated with 10 μM of the STAT5 inhibitors StafiA-1 or StafiB-1 during the 14 days of OST stimulation. Scalebar 400 μm. n = 4 for each group. (D) Representative images of human MSCs treated with 10 μM of the STAT5 inhibitors StafiA-1 or StafiB-1 during the 21 days of OST stimulation. Scalebar 400 μm. n = 4 for each group. (E) Representative images of TERT/STAT5 complex (red foci) detected by proximity ligation assay (PLA) in the nucleus of control VICs. Scalebar 25 μm. n = 4 for each group. (F) Relative luciferase activity in hVICS after transfection of hRUNX2 Promoter GLuc-ON pEZX-PG04.1. Samples were analyzed 72 hours after OST treatment. STAT5A inhibitor StafiA-1 (10 μM) was dissolved in DMSO. NT and OST conditions were also supplemented with DMSO, n = 10 per group. (G) (G) Biotin-labeled 60 bp oligos containing the -194 STAT5 binding sequence on the promoter of human RUNX2 were incubated cell extracts from HEK293s in which STAT5 protein was overexpressed (lane 1). Extracts were also incubated with an increasing amounts of unlabeled oligos (lanes 2-5). Cell extract was also incubated with a oligo containing a mutated STAT5A site (mut RUNX2 DNA) (line 9) and incubated with an increased amount of unlabeled mut RUNX2 oligo (lanes 10-13). Blots include the positive and negative controls include in the LightShift Chemiluminescent EMSA Kit (lanes 6-8 and 14-16). (H) Representative immunofluorescent images of Stat5 expression after 12 weeks of high adenine high phosphate diet on Tert-/- and Tert-/- mice aorta. Scale bar 400 μm. Quantification of Stat5 expression is shown on the right panel. (I) Representative images of Stat5 immunofluorescence staining of thoracic aortic rings isolated from Tert+/+ and Tert-/- mice after 14 days of OST treatment relative to NT control treatment. Quantification of Stat5 is shown on the right graph. Scale bar 400 μm. (J) Mol*3D Viewer rendering of the TERT-STAT5 dimer interaction predicted by the HDock. Red boxes indicate the position of the interaction between TERT and STAT5. (K) The diagram shows the regions involved in the predicted interaction as indicated in A, and the docking and confidence scores predicted by HDock are indicated. TEN: DNA anchor domain for processive telomeric repeat addition, RBD: Telomerase RNA binding domain, RT: Finger and palm region of the reverse transcriptase domain, CTE: C-terminal extension or putative thumb domain of the reverse transcriptase, CCD: Coiled-coil domain, required for nuclear localization, DBD: DNA binding domain, HLK: Helical linker and DNA binding domain, SH2: Domain required for activation and dimerization, TD: Transactivation domain. (L) H3K4me3 CUT&Run sequencing tracks in genomic regions of Runx2 in no-treatment control and osteogenic condition-treated human VICs. (M) Top 20 GO pathways enriched in genes with significant loss of H3K4me3 in OST- vs NT-treated human VICs. Data are shown as means ± SD. P values were calculated with the Mann-Whitney U test (Figures E and G) and the Kruskal-Wallis H test with Dunn pairwise comparison post-test (Figures C, D, and H) and indicated in each graph.

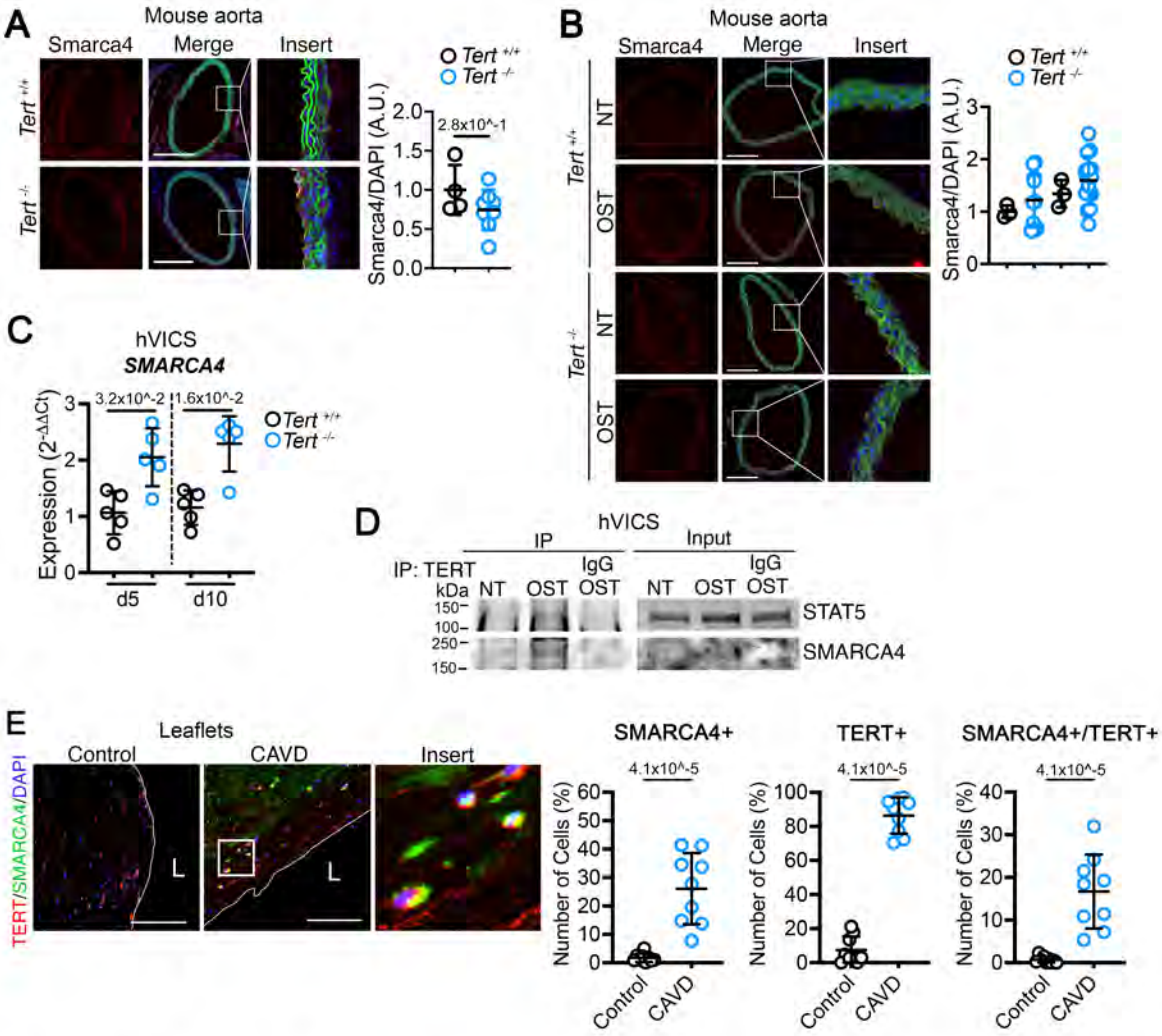

Supplemental Figure 6. Chromatin remodeling enzyme SMARCA4 is upregulated and interacts with TERT during the osteogenic reprogramming of VICs. (**A**) Representative immunofluorescent images of Smarca4 expression after 12 weeks of high adenine high phosphate diet on *Tert*$^{-/-}$ *and Tert*$^{-/-}$ mice aorta. Scale bar 400 µm. Quantification of Smarca4 expression is shown on the right panel. (**B**) Representative images of Smarca4 immunofluorescence staining of thoracic aortic rings isolated from *Tert*$^{+/+}$ and *Tert*$^{-/-}$ mice after 14 days of OST treatment relative to NT control treatment. Quantification of Smarca4 is shown on the right graph. (**C**) *SMARCA4* expression was evaluated on days 5 and 10 on VICs stimulated with OST. n = 5 each group. (**E**) TERT/STAT and TERT/SMARCA4 interaction was detected by co-immunoprecipitation upon osteogenic stimulation on VIC. (**E**) Representative TERT and SMARCA4 immunofluorescent staining in control and CAVD tissues. The number of positive cells is shown on the right graphs. n = 9 control, n = 9 CAVD. Scalebar 100 µm. Data are shown as means ± SD, and P values were calculated with the Mann-Whitney U test and indicated on each graph in Figures A and C. L = lumen.

SUPPLEMENTAL MATERIAL

Non-canonical Telomerase Reverse Transcriptase Controls Osteogenic Reprogramming of Aortic Valve Cells Through STAT5

Rolando A. Cuevas[1], Luis Hortells[2], Claire C. Chu[1], Ryan Wong[1], Alex Crane[1], Camille Boufford[1], Cailyn Regan[1], William J. Moorhead III[1], Michael J. Bashline[1], Aneesha Parwal[1], Angelina M. Parise[1], Parya Behzadi[1], Mark J. Brown[1], Aditi Gurkar[3], Dennis Bruemmer[4], John Sembrat[5], Ibrahim Sultan[6], Thomas G. Gleason[6], Marie Billaud[6], and Cynthia St. Hilaire[1,8,9*]

[1] Division of Cardiology, Department of Medicine, Pittsburgh Heart, Lung, Blood and Vascular Medicine Institute, University of Pittsburgh, Pittsburgh, Pennsylvania, USA.

[2] Cardiovascular Research Group, Department of Medical Biology, Faculty of Health Science, UiT-The Arctic University of Norway, 9019 Tromsø, Norway.

[3] Aging Institute, Division of Geriatrics, Department of Medicine, University of Pittsburgh, Pittsburgh, Pennsylvania, USA.

[4] Department of Cardiovascular Medicine, Cleveland Clinic, Cleveland, OH, USA.

[5] Division of Pulmonary, Allergy, and Critical Care Medicine, University of Pittsburgh School of Medicine, Pittsburgh, PA, USA.

[6] Division of Cardiac Surgery, Department of Cardiothoracic Surgery, Heart and Vascular Institute, University of Pittsburgh Medical Center, Pittsburgh, Pennsylvania, USA.

[7] Department of Surgery, Division of Cardiac Surgery, Brigham and Women's Hospital & Harvard Medical School, Boston, Maryland, USA.

[8] Department of Bioengineering, University of Pittsburgh, Pittsburgh, Pennsylvania, USA.

[9] Department of Cardiothoracic Surgery, University of Pittsburgh, Pittsburgh, Pennsylvania, USA

26

27 Running Title: TERT/STAT5 is required for valvular calcification

28

29 *Corresponding Author Contact Info:

30 Cynthia St. Hilaire, PhD, FAHA

31 University of Pittsburgh

32 BSTWR 1744.1

33 200 Lothrop Street, Pittsburgh, PA 15261

34 +1 412-648-9441 sthilair@pitt.edu

35 **METHODS**

36 **Availability of Materials**

37 We abide by the NIH Grants Policy on Sharing of Unique Research Resources, including the
38 NIH Policy on Sharing of Model Organisms for Biomedical Research (2004), NIH Grants Policy
39 Statement (2003), and Sharing of Biomedical Research Resources: Principles and Guidelines
40 for Recipients of NIH Grants and Contracts (1999), and the Bayh-Dole Act and the Technology
41 Transfer Commercialization Act of 2000. De-identified human cell lines and tissues generated in
42 our laboratory will be made available for non-commercial research per established University of
43 Pittsburgh Office of Research IRB and MTA protocols.

44

45 **Ethics**

46 Human aortic valves were collected from subjects enrolled in studies approved by the
47 institutional review board (IRB) of the University of Pittsburgh per the Declaration of Helsinki. No
48 bicuspid valves were used in this study. Mice used for the generation of cell lines were given
49 veterinary care by the University of Pittsburgh Division of Laboratory Animal Resources, which
50 adheres to the NIH policy on the Animal Welfare Act and all other applicable laws. Facilities are
51 under the full-time supervision of veterinarians and are AAALAC-accredited. Our protocols
52 follow the AVMA Guidelines on Euthanasia. All animal use was approved by the Institutional
53 Animal Care and Use Committee at the University of Pittsburgh.

54

55 **Human Tissue Collection and Isolation**

56 Surgical specimens from humans were collected from subjects who consented and enrolled in
57 studies approved by the institutional review board (IRB) of the University of Pittsburgh per the
58 Declaration of Helsinki. Personnel involved with specimen handling underwent extensive
59 institutional training. Cadaveric donor tissues were obtained via the Center for Organ Recovery

60 and Education (CORE) and were approved by the University of Pittsburgh Committee for
61 Oversight of Research and Clinical Training Involving Decedents (CORID). A detailed protocol
62 describing tissue collection hand handling was published previously.[1] Briefly, valves were
63 collected from valve replacement surgeries or recovered from cadaveric organs and stored in
64 cold Belzer UW Cold Storage Transplant Solution (Bridge to Life) at 4°C for transporting. Aortic
65 roots were excised and washed with a sterile rinsing solution (sterile PBS supplemented with
66 2.5 µg/mL of fungicide, 0.05 mg/mL of gentamicin, and 5 µg/mL of bactericide). Leaflets were
67 unbiasedly selected for VIC isolation, Von Kossa staining for calcification, and snap freezing for
68 RNA collection. Tissues were processed as close as possible to the extraction time to
69 guarantee the best yield of cell recovery.
70
71 **Human Cell Isolation**
72 We established patient-specific lines by using the same valves for histopathology, RNA, and cell
73 isolation. Human primary aortic valve interstitial cells (VICs) lines were generated from male and
74 female subjects as previously described.[1] Briefly, leaflets were washed with PBS containing 10
75 mg/ml gentamicin (GIBCO) and 250 µg/ml fungizone (GIBCO) and dissociated with 0.1%
76 collagenase II at 37 C and 5% of CO2 for 18 hours. Then, the tissue was further dissociated by
77 gently mixing it by pipetting with a serological pipette to ensure the release of VICs and then
78 passed through a 0.70 µm filter to remove debris. Cells were pelleted and then resuspended in
79 Dulbecco's Modified Eagle's Medium (DMEM) supplemented with 10% fetal bovine serum (FBS)
80 and 1X penicillin-streptomycin (P/S). Human coronary artery smooth muscle cells (CASMC)
81 were obtained from the patient coronary as previously described.[2] Briefly, vessels were washed
82 with PBS containing 10 mg/ml gentamicin (GIBCO) and 250 µg/ml fungizone (GIBCO). Vessels
83 were cut open to expose the lumen, and intima and adventitia were gently scrapped. Vessels

84 were then sectioned and dissociated with 0.1% collagenase II for 3 hrs. Cells were pelleted and
85 then seeded and expanded.
86
87 **Murine tissue and cell isolation**
88 All murine cell lines are generated from a single animal. Males and females, 6 to 8 weeks old,
89 *Mus musculus Terc*$^{-/-}$ (Jackson Labs, strain # 004132) mice were utilized for cell isolation. Males
90 and female *Tert*$^{-/-}$ (Jackson Labs, strain # 005423, 10-12 weeks old) mice were bred with wild-
91 type mice (Jackson Labs, 000664) to produce *Tert*$^{+/-}$ heterozygous mice. Heterozygous *Tert*$^{+/-}$
92 breeding regimes were used to prevent telomere attrition. PCR confirmed genotype. Mouse BM-
93 MSCs were isolated from femurs, and tibias were dissected from three-month-old *Tert*$^{+/+}$ or *Tert*$^{-}$
94 $^{/-}$ mice. The marrow was rinsed out of the bones with MSC media, and cells were plated and
95 expanded as described previously.[3] Mouse VICs were isolated from the hearts of three-month-
96 old *Tert*$^{+/+}$ *or Tert*$^{-/-}$ or mice and were removed, dissected, and valve leaflets removed. Cells
97 were isolated and expanded as described previously.[4] Animals were handled by designed
98 members in our lab. Tissue and cell isolation were carried out by a different team to ensure
99 randomization. Mice were given veterinary care by the University of Pittsburgh Division of
100 Laboratory Animal Resources, which adheres to the NIH policy on the Animal Welfare Act and
101 all other applicable laws. Facilities are under the full-time supervision of veterinarians and are
102 AAALAC-accredited. Our protocols follow the AVMA Guidelines on Euthanasia. All animal
103 breeding and isolations were approved by the Institutional Animal Care and Use Committee at
104 the University of Pittsburgh. We made attempts to minimize the number of mice required to
105 complete experiments.
106
107 **Cell Culture**

108 VICs lines were expanded in Dulbecco's Modified Eagle's Medium supplemented with 10% fetal
109 bovine serum and 1X penicillin-streptomycin. Cells were used between passages 4 and 15.
110 Growth media was changed every three days, and cells were split 1:2 when confluent. Human
111 coronary artery smooth muscle cells (CASMCs) lines were expanded in smooth muscle media
112 SMGM (CC-3181) supplemented with BULLETKIT (CC-4149). Human mesenchymal stem cells
113 (MSCs, PT-2501, Lonza) were expanded on Minimum Essential Medium alpha without
114 nucleosides and supplemented with 10% fetal bovine serum and 1X penicillin-streptomycin and
115 used between passages 4 and 10. Cells are routinely tested for mycoplasma contamination.
116
117 **Osteogenic Assay**
118 For osteogenic experiments, 250,000 cells per 9.5 cm^2 were seeded and treated with
119 osteogenic media (OST, Gibco Minimum Essential Medium alpha with nucleosides, 10% FBS,
120 1X P/S, 10 mM glycerol phosphate, 50 µM ascorbic acid 2-phosphate, and 100 nM
121 dexamethasone).[5] No treatment media consisted of Gibco Minimum Essential Medium alpha
122 with nucleosides, 10% FBS, 1X P/S. Media was replaced every four days and prepared fresh
123 every time. BiBR1532 (2981, Tocris) was added to the media at 1, 10, or 100 nM every two
124 days during the OST treatment.[6] Inhibitors StafiA-1 and StafiB-1 (HY-136546, HY-112647 MedC
125 hemExpress) were used at 10 µM. Inhibitors BAY-117082 (catalog number S2913,
126 SelleckChem) and 10058-F4 (catalog number S7153, SelleckChem) were used at a maximum
127 of 10 and 50 10 µM, respectively. Inhibitors were added every two days for the duration of the
128 OST treatment. For inflammatory assays, we used 2.5 µg/mL of LPS from Escherichia coli
129 O111:B4 (Sigma-Aldrich) every two days for the duration of the OST treatment.
130
131 **SDS-Page and Immunoblotting**

132 Cells were lysed in lysis buffer (1% CHAPS hydrate, 150 mM sodium chloride, 25 mM HEPES
133 buffer), supplemented with 1x protease and phosphatase inhibitor cocktail (Sigma-Aldrich).
134 Cells were scraped and transferred into microcentrifuge tubes, vortexed for 10 minutes,
135 freeze/thawed for 5 cycles, then centrifuged at 12,000 x g for 10 minutes at 4°C, and
136 supernatants were collected. Proteins were separated with TGX 4-20% stain-free
137 polyacrylamide gel (Bio-Rad) in 1x Tris/Glycine/SDS buffer (Bio-Rad) and transferred to 0.2 um
138 nitrocellulose (1620112, Bio-Rad) membrane in 1x Trans-Blot Turbo Transfer Buffer (Bio-Rad)
139 using the Trans-Blot Turbo Transfer System (Bio-Rad) according to the manufacturer
140 recommendations. The membranes were blocked in Odyssey blocking buffer (PBS, Li-COR)
141 and immunoblotted overnight with primary antibodies against TERT (600-401-252, Rockland),
142 STAT5 (9420S, Cell Signaling), RUNX2 (ab192256, Abcam), OPN (AF808, R&D systems),
143 αSMA (ab5494, Abcam), TNAP (MAB2909, R&D systems), a-tubulin (926-42213, LI-COR),
144 followed by secondary anti-rabbit or anti-mouse IgG antibody (926-68070, 926-68021, 926-
145 32211, LI-COR). Primary and secondary antibodies were diluted in Odyssey blocking buffer with
146 0.1% Tween 20. Membranes were washed in PBS with 0.1% Tween 20. Immunofluorescence
147 signals were detected with the Odyssey CLx system (LI-COR), and images were analyzed with
148 Image Studio (Version 5.2, LI-COR).
149
150 **Immunofluorescent Staining on Fixed Cells**
151 Cells were washed with PBS and then fixed with 4% paraformaldehyde (5025999, Electron
152 Microscopy Sciences) for 15 minutes at room temperature, followed by 10 minutes of
153 permeabilization with TRITON X-100 0.5% (Fisher Scientific). Cells were incubated at room
154 temperature for 1 hour in a blocking buffer (PBS, 0.5% Triton-X 100, 5% FBS). Primary
155 antibodies were diluted in the blocking solution and then incubated overnight at 4°C. Next, cells
156 were washed three times for five minutes each with PBS containing 0.1% TWEEN. Fluorescent

157 secondary antibodies were diluted in blocking solution and incubated for one hour protected
158 from the light, then washed three times for five minutes each with PBS, 0.1% TWEEN 20 with a
159 final wash in PBS. Specimens were finally mounted with Fluoroshield Mounting Medium with
160 DAPI (Abcam) and imaged within 24 hours. F-Actin was stained with AlexaFluor488 Phalloidin
161 (Molecular Probes) for 30 minutes, then washed with PBS before mounting. Calcium
162 accumulation was determined with OsteoImage (Lonza) following the manufacturer's
163 recommendations. Images were obtained in an EVOS FL microscope (AMA3300, Life
164 Technologies) at 20x with an EVOS Plan Fluor 20x/0.5 objective (AMEP 4698, Life
165 Technologies) at 360/447 nm excitation/emission (DAPI), 470/525 nm excitation/emission
166 (GFP), and 530/593 nm excitation/emission (RFP) filters. Representative images are selected
167 based on quality, and if the assay includes quantification, the image that shows the average of
168 the quantification across multiple images.
169
170 **Immunofluorescent Staining on Paraffin Sections**
171 Human specimens were embedded in paraffin and cut to 10 μm thickness. Slides were warmed
172 to 65°C, deparaffinized using xylene and graded alcohol baths, rehydrated in distilled H_2O, and
173 boiled for 20 minutes in antigen unmasking solution (H-3300, Vector Labs). Cooled samples
174 were then washed with PBS for five minutes. Specimens were then blocked with PBS
175 containing 3% fish skin gelatin and 10% horse serum for one hour. Primary antibodies were
176 diluted in the blocking solution and incubated overnight at 4°C. Next, specimens were washed
177 three times for five minutes each with PBS containing 3% fish skin gelatin and 0.1% TWEEN 20.
178 Fluorescent secondary antibodies were diluted in a blocking solution, incubated for one hour,
179 protected from the light, and washed thrice for five minutes each. Normal rabbit polyclonal IgG
180 (Invitrogen, 31235) and Normal mouse IgG (Vector, I-200U) were used as a negative isotype
181 antibody control at the same concentration of the specific antibodies. Specimens were finally

182 mounted with Fluoroshield Mounting Medium with DAPI (Abcam) and imaged within 24 hours.
183 Images were obtained in a EVOS FL microscope (AMA3300, Life Technologies) at 20x with a
184 EVOS Plan Fluor 20x/0.5 objective (AMEP 4698, Life Technologies) at 360/447 nm
185 excitation/emission (DAPI), 470/525 nm excitation/emission (GFP), and 530/593 nm
186 excitation/emission (RFP) filters. Representative images are selected based on quality, and if
187 the assay includes quantification, the image that shows the average of the quantification across
188 multiple images.
189
190 **Alizarin Red Staining and Quantification**
191 Cells were washed with PBS and then fixed with 4% paraformaldehyde (Electron Microscopy
192 Sciences) for 15 minutes at room temperature, followed by two washes with deionized water.
193 Fixed cells were then covered with 40 mM Alizarin Red S (Sigma-Aldrich) at pH 4.1 – 4.3 and
194 gently rocked for 20 minutes at room temperature. Cells were then washed twice with deionized
195 water to remove any unincorporated dye. After imaging, Alizarin Red S was extracted with 10%
196 (v/v) acetic acid (Fisher Scientific) for 30 minutes, scraped into a microcentrifuge tube, vortexed,
197 and then incubated at 85°C for 10 minutes. After chilling on ice for 5 minutes, the mixture was
198 centrifuged at 20,000 x g for 15 minutes at 4°C. 500 µl of supernatant was transferred to a new
199 tube, and 10% (v/v) ammonium hydroxide (Fisher Scientific) was then added to the supernatant.
200 Absorbance was at 405 nm using a 96-well plate spectrophotometer.
201
202 **Von Kossa Staining**
203 Human specimens embedded in paraffin were warmed to 65°C for one hour and then
204 deparaffinized through xylene and graded alcohol incubations. Specimens were then
205 rehydrated in distilled water. Specimens were stained using the Von Kossa Method of Calcium
206 Kit (Polysciences, 24633-1) following the manufacturer's instructions.

207

208 **Lentiviral Production and Cell Infection**

209 Lentiviruses were produced by transfecting Dharmacon SMARTvector Lentiviral plasmids
210 encoding shTERT TurboGFP (shTERT, V3SH11240-225610522). Turbo SMARTvector Non-
211 targeting Control (shControl,VSC11707) into HEK293T cells following manufacturer
212 recommendations. shSTAT5A (sc-29495-V) was obtained from Santa Cruz. The viral-containing
213 supernatant was collected at 48h after transfection, filtered through a 0.45-µm filter, and stored
214 at -80C. Human VICs, CASMCs, and MSCs lines were transduced with MOI of 5 in the
215 presence of 0.8 µg ml^{-1} polybrene (Millipore) to enhance transduction efficiency.

216

217 **Transcriptional Analysis**

218 Tissue RNA was isolated using Trizol (Life Technologies). Cell RNA was isolated using Quick-
219 RNA MiniPrep (Zymo Research). RNA was treated with DNAse I (Zymo Research) in
220 accordance with the manufacturer's instructions. Reverse transcription was performed using
221 MultiScribe Reverse Transcriptase system (43-112-35, Fisher). Sixteen ng of cDNA was used
222 per reaction. qPCR was performed on a CFX Connect Real-Time System (Bio-Rad) using
223 PowerUP SYBR Green Master Mix (A25741, Applied Biosystems) as follows: one cycle at 95 °C
224 (10 minutes) and 40 cycles of 95 °C (20 seconds) and 58 °C (20 seconds) and 72°C (1 minutes).
225 *GAPDH* or *18s* gene expression was used to normalize expression. Relative expression was
226 calculated using the average threshold cycle number and the $2^{(Ct(housekeeping\ gene)-Ct(target\ gene))}$
227 formula. Primers are listed in Supplementary Table 3.

228

229 **Luciferase Assay**

230 Human VICs ($0.5x10^5$ cells/well) were seeded in 24-well plates and transfected with the RUNX2
231 Promoter GLuc-ON plasmid (HPRM32232-PG04, Genecopoeia) using Lipofectamine 3000

232 (L3000001, ThermoFisher). This plasmid encodes 1627 bp upstream of the human *RUNX2*
233 gene NM_001015051. 48 hrs after transfection, the cells were treated with OST media for 72
234 hrs. Luciferase activities were measured using the Secrete-Pair Dual Luminescence Assay Kit
235 (LF032, Genecopoeia), following to the manufacturer's instructions. The results were expressed
236 as relative light units (RLU) of luciferase to secreted alkaline phosphatase (SEAP)
237
238 **CUT&Run**
239 The CUT&Run assay was performed using the CUTANA Kit V3 (14-1048, EpiCypher) according
240 to the manufacturer's instructions. Briefly, human VICs were cultured in osteogenic media for
241 seven days. On the extraction day, 500,000 cells were harvested and tagged with concanavalin
242 A-coated magnetic beads. The coated cells were incubated overnight with 0.5 µg of H3K4me3
243 antibody (Part number 13-0041k, EpiCypher) at 4°C. The following day, samples were
244 incubated with pAG-MNase (Part number 15-1016, EpiCypher) for 2 hours at 4°C. DNA was
245 purified and indexed with 14 PCR cycles to generate the libraries. Sequencing was performed
246 on an Illumina NextSeq 2000, resulting in the generation of 60-bp paired-end reads. Raw data
247 was processed and analyzed using CLC Genomic Workbench (version 24.0.1, Qiagen). Reads
248 resulting from H3K4me3 binding were aligned to the human genome assembly GRCh38. Peaks
249 were annotated to the nearest gene, and the binding between no treatment and osteogenic
250 conditions was compared to identify osteogenic differentially regulated genes with a P-value of
251 less than 0.05 (GEO accession number GSE274226). Visualization was conducted using the
252 CLC Genomic Workbench. GO pathway analyses were performed with DAVID version
253 2023q4.[7,8]
254
255 **CUT&Tag**

256 CUT&Tag assay was performed using the CUT&Tag-IT Assay Kit (Catalog No. 53160, Active
257 Motif) following the manufacturer's instructions. Briefly, wild-type *Tert*$^{+/+}$ and *Tert*$^{-/-}$ mouse VICs
258 were cultured in osteogenic media for seven days. On the extraction day, 500,000 cells were
259 harvested and tagged with concavalin-A-coated magnetic beads. Coated cells were incubated
260 overnight with 1 µg of antibody against STAT5 (9420S, Cell Signaling) in 50 µl of total volume at
261 4°C with slow rotation. After washing, cells were incubated with guinea pig anti-rabbit antibody
262 (Part No. 105465, Active Motif) at room temperature for 1 hour, followed by incubation with pre-
263 assembled pA-Tn5 Transposomes at room temp for 1 hour (Part No. 105458, Active Motif).
264 Tagmentated DNA was purified and indexed with 14 PCR cycles with Q5 Polymerase (part no.
265 104483, Active Motif) to generate the libraries. Sequencing was performed on an Illumina
266 NextSeq 2000. 60-bp paired-end reads were generated. Raw data was processed and analyzed
267 with CLC Genomic Workbench (version 24.0.1, Qiagen) supplied by the University of Pittsburgh.
268 Reads resulting from STAT5 binding were aligned to the mouse reference genome mm10
269 assembly version GRCm39. The peaks were annotated to the nearest gene, and binding
270 between no treatment and osteogenic conditions was compared to define osteogenic
271 differentially regulated genes of those with a P-value less than 0.1 (GEO accession number
272 GSE274226). Visualization was performed with IGV and CLC Genomic Workbench. GO
273 pathway analyses were performed with DAVID version 2023q4.[7,8]
274
275 **Telomere Length Analysis**
276 Tissue and VICs genomic DNA was isolated from passage 1 using DirectAmp Tissue Genomic
277 DNA Amplification Kit (Denville Scientific). Telomere length was analyzed using real-time PCR
278 as previously described.[9] Briefly, genomic DNA was isolated following standard protocol, and 10
279 ng of gDNA per reaction was utilized. Samples were run in triplicate with 35 ng of DNA per
280 reaction, and telomere repeats were amplified using PowerUP SYBR Green Master Mix

281 (Thermofisher Scientific) on a CFX Connect Real-Time PCR System (Bio-Rad). Repeated
282 amplification data were normalized to *RPLP0*/*36b4* as a single copy-gene. Primers are listed in
283 Supplementary Table 3.
284
285 **Electrophoretic Mobility Shift Assay (EMSA)**
286 HEK293 overexpressing STAT5 were lysed in ice-cold hypertonic non-denaturing buffer (20 mM
287 Tris-HCl, pH 8.0, 137 mM NaCl, 1% Nonident P-40, and 2 mM EDTA) and microfuged at 14,000
288 rpm for 5 minutes at 4°C. The supernatant containing STAT5 was collected, and 6.8 µg of the
289 extract was incubated for 30 minutes at 37°C with 20 fmol of biotinylated–end-labeled 60-mer
290 double-stranded RUNX2 promoter containing the STAT5 centered at -194 5'-
291 AAGCTATATCCTTCTGGATGCCAGGAAAGGCCTTACCACAAGCCTTTTGTGAGAGAAAGA-
292 3' (underlined) binding site. The specificity of STAT5 binding to the wild-type probe was
293 determined with mutated STAT5 binding site, 5′-
294 AAGCTATATCCTTCTGGAAACAACTGCTCGGCGAGACACAGTCCTTTTGTGAGAGAAAGA-
295 3' oligonucleotide. Binding reactions were carried out with LightShift® Chemiluminescent
296 EMSA Kit (ThermoFisher) according to the manufacturer's instructions. Briefly, a final volume
297 of 20 µL containing the STAT5 extract and the probe plus 1 µg poly(dI-dC), 100 mM MgCl2,
298 50% glycerol, and 1x propietary binding buffer. Bound complexes were separated on 6%
299 acrylamide gel with TBE running buffer, crosslinked to a nylon membrane at 120mJ/cm^2, and
300 then visualized on BioChem Docs (Bio-RAD). No STAT5 binding was displaced by adding
301 unlabeled (cold) wild-type oligonucleotide to the reaction. No STAT5 binding to the mutated
302 probe was detected in our experiments, confirming the specificity of interaction between STAT5
303 and wild-type oligonucleotide.
304
305 **Proliferation Assays**

306 Cell proliferation was evaluated using Trypan Blue incorporation in an automatized cell counter
307 Countess II FL (Invitrogen). Briefly, cells were grown on alpha-MEM supplemented with 10% of
308 FBS and penicillin and streptomycin cocktail (GIBCO) for the duration of the assay. Growth was
309 quantified twice a week. Cell number during OST treatment was determined at the beginning
310 and end of the assay.
311
312 **Senescence-Associated β-Galactosidase Assays**
313 Cellular senescence was evaluated by senescence-associated β-Galactosidase (SA-β-Gal)
314 activity assay. Briefly, cells were washed with PBS and then fixed with 4% paraformaldehyde
315 (Electron Microscopy Sciences) for 5 minutes at room temperature and then washed twice with
316 PBS. Next, cells were incubated in X-Gal Solution Mix containing 1 mg/mL of 5-Bromo-4-
317 Chloro-3-Indolyl-Alpha-D-Galactopyranoside (American Bioanalytical), 40 mM Sodium
318 Phosphate monobasic solution (Sigma-Aldrich), 40 mM Sodium Phosphate Dibasic solution
319 (Sigma-Aldrich), 40 mM Citric Acid (Sigma-Aldrich), 5 mM Potassium Ferrocyanaide (Sigma-
320 Aldrich), 5 mM Potassium Ferricyanaide (Sigma-Aldrich), 150 mM $NaCl_2$, and 2 mM $MgCl_2$, pH
321 6.0, for 16 hours at 37°C without CO_2 to develop blue color. Then, cells were washed twice with
322 PBS, and SA-*β*-gal positive cells were imaged and calculated based on randomly selected
323 bright fields areas containing at least 200 cells per field as revelated by subsequent DAPI
324 staining.
325
326 **Cell Migration Assays**
327 VICs were seeded in a 12-well plate at a concentration of $1x10^5$ cells per well and were left until
328 they reached 90% of confluence. The well surface was scratched with a 200 µl sterile pipette tip
329 and washed with PBS to remove detached cells. Horizontal lines were drawn on the bottom
330 outside of the well and used as a reference for alignment to obtain the same field for each

331 image acquisition run. VICs media was added, and images were collected at different time
332 points with a phase-contrast microscope using the horizontal lines as reference marks. Scratch
333 area and scratch width were determined with the Wound Healing Size Macro Tool using
334 ImageJ.[10] Linear regression was used to compare the changes in the area and the average
335 length of the scratch
336
337 **Chromatin Immunoprecipitation**
338 Chromatin Immunoprecipitation (ChIP) was performed on cultured cells as previously
339 described.[11] Briefly, VICs were stimulated with OST for 14 days and then collected in 20 mM
340 Na-butyrate dissolved in PBS, and cross-linking of DNA and proteins was performed with
341 formaldehyde (1% vol/vol final concentration) at room temperature. Cross-linking was stopped
342 with 125 mM glycine for 10 min. Cross-linked chromatin was sonicated to obtain fragments
343 between 250 and 750 base pairs in a Bioruptor Pico sonication device (Diagenode). The
344 sheared chromatin was immunoprecipitated with 1 ug of antibody raised against TERT
345 (Rockland, 600-401-252S) and 0.3 ug STAT5 (Cell Signaling, 94205S). Normal rabbit polyclonal
346 IgG (Cell Signaling, 2729S) was used as a negative control. Negative control was incubated
347 with rabbit IgG and input DNA primary antibody. Chromatin complexes were recovered with
348 ChIP-grade Protein G magnetic beads (9006S, Cell Signaling). DNA was recovered with
349 standard phenol-chloroform extraction. Immunoprecipitated DNA was amplified by quantitative
350 RT-PCR using SYBR green. ChIP primers are listed in Supplementary Table 3.
351
352 **Proximity Ligation Assays (PLA)**
353 PLA was performed directly after cell fixation and according to manufacturer instructions. Briefly,
354 cells were blocked with Duolink blocking solution for 60 minutes at 37°C. Samples were then
355 incubated with rabbit TERT and mouse STAT5 antibodies diluted in Duolink Blocking Solution

356 and incubated overnight at 4°C. Samples were then incubated with secondary antibodies
357 conjugated with PLA probes (DUO92002, DUO92004, Sigma) for 2 h at 37°C in a humidity
358 chamber, followed by probe ligation for 30 minutes at 37°C as recommended by the
359 manufacturer. Amplification was performed with Duolink detection kit Red 595 nm for 100
360 minutes at 37°C (DUO92101, Sigma). Samples were mounted in DAPI-containing mounting
361 media and prepared for image acquisition. PLA foci were quantified using ImageJ relative to the
362 number of cells per field. Fields with over 50 cells and 5 fields per cell line were acquired.
363 Nuclear PLA foci were all puncta circumscribed to the nuclear (DAPI) signal.
364

365 **Promoter Analysis**

366 The upstream region of the *RUNX2* (NM_001015051.3) promoter was scanned with LASAGNA
367 and TRANSFAC/ suites.[12,13] Searches were conducted with data version 2021.3, high-quality
368 matrices, and cut-offs to minimize false positive hits. STAT5 logo analysis was performed with
369 WebLogo (weblogo.berkeley.edu).
370

371 **SplitFAST plasmid construction and SplitFAST assay**

372 Plasmids containing full-length human CDS TERT pEZ-M02-CMV-hTERT and STAT5A pEZ-
373 M02_CMV_hSTAT5A were purchased from Genecopeia (catalog numbers EX-Q0450-M02-10
374 and EX-F0979-M02-10, respectively). Plasmids containing NFAST (pCMV-FRB-NFAST) and
375 CFAST (pCMV-FKBP-CFAST) tags were purchased from The Twinkle Factory (catalog
376 numbers PL058 and PL040, respectively). Fusion plasmids were constructed by PCR assembly.
377 TERT and STAT5A were amplified using primers hTERT-RP-SplitFAST and hTERT-FP-
378 SplitFAST and hSTAT5A-RP-SplitFAST and hSTAT5A-FP-SplitFAST, respectively
379 (Supplementary Table 3). The plasmid pCMV-TERT-NFAST was generated by inserting TERT
380 gene into pAG148-FRB-NFAS using restriction enzymes *Bgl*II and *Kpn*2I. The plasmid pCMV-

381 STAT5A-CFAST was generated by inserting the STAT5A gene into pAG152-FRB-FRB-
382 CFAST11 using restriction enzymes *Bgl*II and *Kpn*2I. Insertions were validated by full plasmid
383 sequencing. pCMV-TERT-NFAST and pCMV-STAT5A-CFAST fusion plasmids were
384 transfected in a 1:1 ratio in control hVICs with XtremeGene 9 DNA transfection reagent (catalog
385 number 39320900, Roche) following manufacturer recommendations. To image the interaction
386 between TERT and STAT5A, cells were imaged in alpha-MEM supplemented with 5 µM µM 4-
387 hydroxy-3,5- dimethoxy benzylidene rhodamine (HBR-3,5DOM, dissolved in DMSO) at d3, d5,
388 and d7 of OST treatment in an EVOS FL microscope (AMA3300, Life Technologies) at 20x with
389 an EVOS Plan Fluor 20x/0.5 objective (AMEP 4698, Life Technologies) at 360/447 nm
390 excitation/emission (DAPI), 470/525 nm excitation/emission (GFP).
391
392 **In-Silico Modeling**
393 PDB files for TERT (UniProt 014746) and STAT5A (UniProt K7EIF9) were downloaded from the
394 EMBL-EBI-maintained AlphaFold protein structure database.[14] The STAT5A file was then
395 uploaded to the HDOCK server as both the receptor and ligand.[15] The top predicted model for
396 the STAT5A dimer was downloaded and reuploaded as the receptor file, while the TERT file
397 was uploaded as the ligand. The top predicted model was downloaded and visualized with the
398 Mol viewer.[16] Separately, the residue data were examined to assess which regions of TERT and
399 STAT5 were predicted to localize.
400
401 **Animal Model of Aortic Artery Calcification (in vivo calcification)**
402 Vascular calcification was induced in 8-weeks old *Tert*$^{+/+}$ and *Tert*$^{-/-}$ mice with a 12-week diet
403 regime consisting of chow (LabDiet 5P00, Prolab RMH 3000), supplemented with 0.2% adenine
404 (adenine 0.2%, FD&C Blue No. 2 0.3%, LabDiet 5ZAF) for 6 weeks followed by chow
405 supplemented with 0.2% adenine and 1.8% phosphate (adenine 0.2%, FD&C Blue No. 40 0.3%,

406 sodium phosphate 0.65%, potassium phosphate 1,0%, dicalcium phosphate 3.55%, LabDiet
407 5ZRX) or 6 weeks.[17] Both groups included an equal number of male and female mice. At the
408 end of the 12-week diet, aortas were dissected for histological analysis, Von Kossa, and
409 immunohistochemistry.
410

411 **Cultured Aortic Segments Calcification (ex vivo calcification)**

412 Aorta were dissected from *Tert*$^{-/-}$ and *Tert*$^{+/+}$ mice after euthanized with CO2 and cervical
413 dislocation, followed by in situ perfusion with 10 ml of PBS. Collected arteries were cut into 3-4
414 mm segments and cultured in osteogenic or control media for 14 days in a humidified incubator
415 with 5% CO2 at 37 °C. The medium was changed every 2-3 days. Aortic arteries osteogenic
416 media was prepared as follows: DMEM (11965092, Thermo Fisher Scientific, MA, USA)
417 supplemented with 1% fetal bovine serum (FBS), 1% Antibiotic-Antimycotic (15240062, Thermo
418 Fisher Scientific), 10 mM β-glycerophosphate disodium (G9422, Sigma), 0.25 mM L-ascorbic
419 acid (49752, Sigma), and 10 nM dexamethasone (D4902, Sigma). The control medium was
420 prepared with DMEM supplemented with 1% FBS and 1% Antibiotic-Antimycotic. At the end of
421 the treatments, aortic segments were washed with PBS, fixed in 4% PFA for 4 hours, embedded
422 in paraffin wax, and cut in 10 um slices for histology and immunofluorescence staining.
423

424 **Blinding Procedures**

425 Professionally trained technicians handled animal welfare, including weaning and mouse line
426 expansion, diets, sacrifice, and surgery. For experiments involving human samples and in vivo
427 and ex vivo murine experiments, blinding procedures were used. Individuals conducting and
428 analyzing experiments did not know the clinical diagnosis nor treatment groups until after the
429 analysis was performed.
430

431 **Sample Size and Power Analysis.**

432 The two-sample Cohen's D algorithm for large-size effects was used.[18] Power was defined at >
433 80%, with confidence levels of 95%, alpha at 0.05, and P significance value. The animal size
434 was based on a power analysis that assumes confidence levels of 95%, the probability of
435 finding a statistical difference between groups of 80%, an expected difference of 37% between
436 groups, and a standard deviation of 25%; experiments required at least five mice per group. A
437 25% redundancy is built-in to allow for mortality associated with treatments and other
438 complications.

439

440 **Statistics**

441 Statistical analyses were performed with GraphPad Prism 9.2 (GraphPad Software, San Diego,
442 CA) software. All experiments used at least n = 3 biological replicates and were run in technical
443 duplicates. Statistical comparisons between the two groups were performed by a nonparametric
444 Mann-Whitney *U* test. Statistical comparisons among more than two groups were performed by
445 nonparametric Kruskal-Wallis *H* tests with post hoc Dunn's multiple pairwise comparisons
446 between groups. Shapiro-Wilk normality test was used to test data distribution. Data are
447 presented as mean ± SD.

448

449 **REFERENCES**

450 1. Cuevas RA, Chu CC, Moorhead WJ, 3rd, Wong R, Sultan I, St Hilaire C. Isolation of
451 Human Primary Valve Cells for In vitro Disease Modeling. *J Vis Exp*. 2021:e62439. doi:
452 10.3791/62439
453 2. Gupta GK, Dhar K, Del Core MG, Hunter WJ, 3rd, Hatzoudis GI, Agrawal DK.
454 Suppressor of cytokine signaling-3 and intimal hyperplasia in porcine coronary arteries
455 following coronary intervention. *Exp Mol Pathol*. 2011;91:346-352. doi:
456 10.1016/j.yexmp.2011.04.004

457 3. Huang S, Xu L, Sun Y, Wu T, Wang K, Li G. An improved protocol for isolation and
458 culture of mesenchymal stem cells from mouse bone marrow. *J Orthop Translat*.
459 2015;3:26-33. doi: 10.1016/j.jot.2014.07.005
460 4. Bouchareb R, Lebeche D. Isolation of Mouse Interstitial Valve Cells to Study the
461 Calcification of the Aortic Valve In Vitro. *J Vis Exp*. 2021. doi: 10.3791/62419
462 5. Hoemann CD, El-Gabalawy H, McKee MD. In vitro osteogenesis assays: influence of the
463 primary cell source on alkaline phosphatase activity and mineralization. *Pathol Biol*
464 *(Paris)*. 2009;57:318-323. doi: 10.1016/j.patbio.2008.06.004
465 6. Pascolo E, Wenz C, Lingner J, Hauel N, Priepke H, Kauffmann I, Garin-Chesa P, Rettig
466 WJ, Damm K, Schnapp A. Mechanism of human telomerase inhibition by BIBR1532, a
467 synthetic, non-nucleosidic drug candidate. *J Biol Chem*. 2002;277:15566-15572. doi:
468 10.1074/jbc.M201266200
469 7. Huang da W, Sherman BT, Lempicki RA. Systematic and integrative analysis of large
470 gene lists using DAVID bioinformatics resources. *Nat Protoc*. 2009;4:44-57. doi:
471 10.1038/nprot.2008.211
472 8. Sherman BT, Hao M, Qiu J, Jiao X, Baseler MW, Lane HC, Imamichi T, Chang W.
473 DAVID: a web server for functional enrichment analysis and functional annotation of
474 gene lists (2021 update). *Nucleic Acids Res*. 2022;50:W216-w221. doi:
475 10.1093/nar/gkac194
476 9. Cawthon RM. Telomere measurement by quantitative PCR. *Nucleic Acids Res*.
477 2002;30:e47. doi: 10.1093/nar/30.10.e47
478 10. Suarez-Arnedo A, Torres Figueroa F, Clavijo C, Arbelaez P, Cruz JC, Munoz-Camargo
479 C. An image J plugin for the high throughput image analysis of in vitro scratch wound
480 healing assays. *PLoS One*. 2020;15:e0232565. doi: 10.1371/journal.pone.0232565
481 11. Dahl JA, Collas P. A rapid micro chromatin immunoprecipitation assay (microChIP). *Nat*
482 *Protoc*. 2008;3:1032-1045. doi: 10.1038/nprot.2008.68
483 12. Lee C, Huang CH. LASAGNA: a novel algorithm for transcription factor binding site
484 alignment. *BMC Bioinformatics*. 2013;14:108. doi: 10.1186/1471-2105-14-108
485 13. Wingender E, Dietze P, Karas H, Knuppel R. TRANSFAC: a database on transcription
486 factors and their DNA binding sites. *Nucleic Acids Res*. 1996;24:238-241. doi:
487 10.1093/nar/24.1.238

14. Jumper J, Evans R, Pritzel A, Green T, Figurnov M, Ronneberger O, Tunyasuvunakool K, Bates R, Zidek A, Potapenko A, et al. Highly accurate protein structure prediction with AlphaFold. *Nature*. 2021;596:583-589. doi: 10.1038/s41586-021-03819-2
15. Yan Y, Zhang D, Zhou P, Li B, Huang SY. HDOCK: a web server for protein-protein and protein-DNA/RNA docking based on a hybrid strategy. *Nucleic Acids Res*. 2017;45:W365-W373. doi: 10.1093/nar/gkx407
16. Sehnal D, Bittrich S, Deshpande M, Svobodova R, Berka K, Bazgier V, Velankar S, Burley SK, Koca J, Rose AS. Mol* Viewer: modern web app for 3D visualization and analysis of large biomolecular structures. *Nucleic Acids Res*. 2021;49:W431-W437. doi: 10.1093/nar/gkab314
17. Tani T, Orimo H, Shimizu A, Tsuruoka S. Development of a novel chronic kidney disease mouse model to evaluate the progression of hyperphosphatemia and associated mineral bone disease. *Sci Rep*. 2017;7:2233. doi: 10.1038/s41598-017-02351-6
18. Baguley T. Standardized or simple effect size: what should be reported? *Br J Psychol*. 2009;100:603-617. doi: 10.1348/000712608X377117

Supplemental Table 1: Patient information

Patient ID	Age	Sex	Valve	Cause of Death	Calcification (Von Kossa Staining)	Hypertension	Diabetes	Smoking	Alcohol
2016-034	91	Male	Tricuspid	Natural causes	Yes	No	No	No	Unknown
2016-037	31	Male	Tricuspid	Brain anoxia due to cardiovascular complications	No	No	No	Unknown	Yes
2016-038	81	Male	Tricuspid	Myocardial Infarction	No	No	No	Unknown	Unknown
2016-042	22	Female	Tricuspid	Brain anoxia due to head trauma	No	No	No	No	Unknown
2016-045	59	Female	Tricuspid	Stroke	No	PH	Yes	Yes	Unknown
2016-046	65	Male	Tricuspid	Head trauma from accident	No	No	No	Unknown	Unknown
2016-048	56	Female	Tricuspid	Stroke	No	HTN	No	Unknown	Unknown
2016-050	65	Male	Tricuspid	Stroke	No	HTN	No	Unknown	Yes
2016-051	65	Male	Tricuspid	Natural causes	Yes	HTN	No	Yes	Yes
2016-053	73	Male	Tricuspid	Congestive heart failure	Yes	No	No	No	Unknown
2016-054	63	Female	Tricuspid	Hemorriage and Ruptire AAA	No	No	Yes	No	Unknown
2016-060	73	Male	Tricuspid	Cardiac arrest	Yes	No	No	Unknown	Unknown
2016-061	67	Male	Tricuspid	Natural causes	Yes	No	Yes	Unknown	Unknown
2016-062	59	Male	Tricuspid	Cardiac arrest	Yes	No	No	Yes	Unknown
2016-065	58	Male	Tricuspid	Stroke	No	HTN	Yes	Yes	Unknown
2016-068	68	Female	Tricuspid	Intracranial hemorrhage	Yes	No	No	Yes	Unknown
2016-072	62	Female	Tricuspid	Cardiac arrest	Yes	No	No	No	Unknown
2016-073	41	Female	Tricuspid	Traumatic arrest and motor vehicle accident	No	HTN	No	Yes	Unknown
2016-078	34	Female	Tricuspid	Heart Failure	No	No	No	Unknown	Unknown
2016-079	59	Male	Tricuspid	Respiratory failure	No	HTN	No	No	Unknown
2016-083	52	Male	Tricuspid	Stroke	No	PAH	No	Yes	Unknown
2016-085	52	Male	Tricuspid	Myocardial Infarction	No	PH	No	Unknown	Unknown
2016-091	59	Female	Tricuspid	Stroke	No	HTN	No	Unknown	Unknown
2016-092	47	Female	Tricuspid	Stroke	No	No	No	No	Unknown
2016-093	43	Male	Tricuspid	Cardiac arrest	Yes	HTN	Yes	No	Unknown
2016-095	87	Male	Tricuspid	Myocardial Infarction	Yes	HTN	No	Yes	Unknown
2016-098	57	Male	Tricuspid	Cardiac arrest	No	HTN	No	Yes	Unknown
2016-101	37	Female	Tricuspid	Cardiac Death	No	No	No	Unknown	Unknown

2016-102	58	Female	Tricuspid	Cardiac arrest and asystole	Yes	No	No	Yes	Unknown
2016-103	72	Male	Tricuspid	Cardiac arrest	Yes	HTN	No	Unknown	Unknown
2016-105	86	Male	Tricuspid	Cardiac arrest	Yes	No	No	No	Unknown
2016-118	62	Male	Tricuspid	Cardiac arrest	Yes	No	No	No	Unknown
2016-146	79	Male	Tricuspid	Cardiac arrest	No	No	No	Yes	Unknown
2017-005	66	Female	Tricuspid	Stroke	No	No	No	Unknown	Unknown
2017-025	57	Female	Tricuspid	Brain anoxia due to choking	Yes	No	Yes Type II	Unknown	Unknown
2017-035	48	Female	Tricuspid	Brain anoxia due to CO poisoning	No	No	No	Unknown	Unknown
2017-051	56	Male	Tricuspid	Brain anoxia due to cardiac arrest	No	No	No	Unknown	Unknown
2017-069	37	Male	Tricuspid	Motor vehicle accident	No	No	No	Unknown	Unknown
2017-076	68	Female	Tricuspid	Myocardial Infarction	Yes	No	No	No	Unknown
03-0127	61	Male	Tricuspid	Surgical replacement	No	HTN	No	Unknown	Unknown
03-0129	68	Male	Tricuspid	Surgical replacement	No	HTN	Yes Type II	Unknown	Unknown

HTN = Hypertension

PH = Pulmonary Hypertension

PAH = Pulmonary Arterial Hypertension

Supplemental Table 2: LASAGNA and TRANSFAC STAT5 Search on RUNX promoter

Name	Position	DB	Strand	Sequence	p-value
STAT5B (homodimer)	-4572	TRANSFAC	(-)	cttttccaagaaagc	0
STAT5A (homotetramer)	-2844	TRANSFAC	(-)	taccaacaactttttttctttgaaattgatttcaagatc	0.000325
STAT5A (homotetramer)	-1429	LASAGNA	(-)	tcctagttactgtcacactaggaa	0.00015
STAT5A (homotetramer)	-1372	TRANSFAC	(-)	taaatggcaaaaaaATGCCtagaa	0.0005
STAT5A	-1218	LASAGNA	(+)	gagttcta	0
STAT5A	-430	LASAGNA	(-)	cagaattt	0.0004
STAT5A (homotetramer)	-279	LASAGNA	(+)	ttacaggagtttgggctccttcag	0.000525
STAT5A (homotetramer)	-194	TRANSFAC	(+)	tgccaggaaaggccttaccacaag	0

Supplemental Table 3: qPCR, Cloning Primers, and Oligos

Species	Gene	Forward Primer Sequence 5' -> 3'	Reverse Primer Sequence 5' -> 3'	Amplicon	Technique	Source
Human	TERT	GCATTGGAATCAGACAGCAC	CCACGACGTAGTCCATGTTC	165	qPCR	Sigma-
Human	RUNX2	ATTCCTGTAGATCCGAGCACC	GCTCACGTCGCTCATTTTGC	81	qPCR	IDT
Human	MSX2	GAGCTGGGATGTGGTAAAGG	AAATTCAGAAGATGGAGCGG	142	qPCR	IDT
Human	CDKN1A	TGTCCGTCAGAACCCATG	AAAGTCGAAGTTCCATCGCTC	139	qPCR	IDT
Human	PCNA	ACACTAAGGGCCGAAGATAAC	ACAGCATCTCCAATATGGCTGA	209	qPCR	IDT
Human	TP53	GAGGTTGGCTCTGACTGTACC	TCCGTCCCAGTAGATTACCAC	133	qPCR	IDT
Human	ALPL	ATGGGATGGGTGTCTCCACA	CCACGAAGGGGAACTTGTC	108	qPCR	IDT
Human	GLB1	TATACTGGCTGGCTAGATCACTG	GGCAAAATTGGTCCCACCTATAA	138	qPCR	IDT
Human	STAT3	CAGCAGCTTGACACACGGTA	GCCCAATCTTGACTCTCAATCC	110	qPCR	IDT
Human	STAT5A	ATGTGAAACCACAGATCAAG	TCTGTGGGTACATGTTATAGG	141	qPCR	Sigma-
Human	STAT5B	ATGGGACTCAGTAGATCTTG	CTTCAGTAAAAACCCATCTTCC	127	qPCR	Sigma-
Human	TGFb2	CTGCATCTGGTCACGGTCG	CCTCGGGCTCAGGATAGTCT	151	qPCR	IDT
Human	OSX	CCCCCTTTACAAGCACTAATGG	GGCAGACAGTCAGAAGAGCTG	172	qPCR	IDT
Human	ACTA2	AAAAGACAGCTACGTGGGTGA	GCCATGTTCTATCGGGTACTTC	76	qPCR	IDT
Human	FOXO1	TCGTCATAATCTGTCCCTACACA	CGGCTTCGGCTCTTAGCAAA	168	qPCR	Sigma-
Human	18s	GTAACCCGTTGAACCCCATT	CCATCCAATCGGTAGTAGCG	151	qPCR	IDT
Human	MYH11	CGCCAAGAGACTCGTCTGG	TCTTTCCCAACCGTGACCTTC	129	qPCR	IDT
Human	IL6	AAATTCGGTACATCCTCGACGG	GGAAGGTTCAGGTTGTTTTCTGC	112	qPCR	IDT
Human	VIM	GGAAACTAATCTGGATTCACTC	CATCTCTAGTTTCAACCGTC	83	qPCR	Sigma-
Human	SOX9	GCCAGGTGCTCAAAGGCTA	TCTCGTTCAGAAGTCTCCAGAG	213	qPCR	IDT
Human	KLF4	CCCACATGAAGCGACTTCCC	CAGGTCCAGGAGATCGTTGAA	170	qPCR	IDT
Human	SM22	AGTGCAGTCCAAAATCGAGAAG	CTTGCTCAGAATCACGCCAT	154	qPCR	IDT
Human	TNF	CCTCTCTCTAATCAGCCCTCTG	GAGGACCTGGGAGTAGATGAG	220	qPCR	IDT
Human	BGLAP	GGACTGTGACGAGTTGGCTG	CCGTAGAAGCGCCGATAGG	60	qPCR	IDT
Human	SMTN	CAAAAAGTCCTAACCCCTGCT	TCATGTCGTCCACCTCCAC	77	qPCR	IDT
Human	THBS1	TGCTCCAATGCCACAGTTCC	CTGCTGAATTCCATTGCCACA	132	qPCR	IDT
Human	CNN1	GTCAACCCAAAATTGGCACCA	ACCTTGTTTCCTTTCGTCTTCG	183	qPCR	IDT
Human	MMP13	CACCAATTCCTGGGAAGTCT	GCAGCTGTTCACTTTGAGGA	136	qPCR	IDT
Human	SMARCA4	GATGTCGATGATGAATATGGC	ATCTGGTACTGTTTGAGGAC	140	qPCR	Sigma-
Human	GAPDH	CTGGGCTACACTGAGCACC	AAGTGGTCGTTGAGGGCAATG	101	qPCR	IDT
Human	pRUNX2-1	ACCTTACAGGAGTTTGGGCT	CTTTCCTGGCATCCAGAAGGATA	99	ChIP	IDT
Human	pRUNX2-2	CCGCCCACCCCATTTACTT	GGCGAACAGACCAATTTTCTAGG	124	ChIP	IDT
Human	hTelomere	GGTTTTTGAGGGTGAGGGTGAGGGT	TCCCGACTATCCCTATCCCTATCCCT		PCR	Sigma-
Human	hTERT-RP-SpliFAST	TATATATCCGGAGTCCAGGATGGTCTTGAAGTCTGAGGGC			Cloning	IDT
Human	hTERT-FP-SpliFAST	TATATAAGATCTATGCCGCGCGCTCCCCGCTGC			Cloning	IDT
Human	hSTAT5A-RP-SpliFAST	TATATATCCGGATGAGAGGGAGCCTCTGGCAGA			Cloninig	IDT
Human	hSTAT5A-FP-SpliFAST	TATATAAGATCTATGGCGGGCTGGATCCAGGCC			Cloninig	IDT
Human	hRUNX2-194-WT	AAGCTATATCCTTCTGGATGCCAGGAAAGGCCTTACCACAAGCCTTTTGTGAGAGAAAGA			EMSA	IDT
Human	hRUNX2-194-mut	AAGCTATATCCTTCTGGAAACAACTGCTCGGCGAGACACAGTCCTTTTGTGAGAGAAAGA			EMSA	IDT
Mouse	mRunx2-194-WT	AAAAGCTATAACCTTCTGAATGCCAGGAAGGCCTTACCACAAGCCTTTTGTCAGAGGGAG			EMSA	IDT
Mouse	mRunx2-194-mut	AAAAGCTATAACCTTCTGAACAACTGCTCGGCGAGACACAGTACCTTTTGTCAGAGGGAG			EMSA	IDT